The Local Bonding Environment of Amorphous In-Zn-O Films Studied by X-ray Absorption Fine Structure and Total X-ray Scattering Using Synchrotron Radiation

by

Brandon J. Reese

B.S., Engineering Physics, Colorado School of Mines, 2005

A thesis submitted to the

Faculty of the Graduate School of the

University of Colorado in partial fulfillment

of the requirements for the degree of

Master of Science

Department of Electrical, Computer, and Energy Engineering

2011

This thesis entitled:
The Local Bonding Environment of Amorphous In-Zn-O Films Studied by X-ray Absorption Fine
Structure and Total X-ray Scattering Using Synchrotron Radiation
written by Brandon J. Reese
has been approved for the Department of Electrical, Computer, and Energy Engineering

_____
Garret Moddel

_____
Assc. Prof. Wounjhang Park

_____
Prof. Bart Van Zeghbroeck

Date _____

The final copy of this thesis has been examined by the signatories, and we find that both the
content and the form meet acceptable presentation standards of scholarly work in the above
mentioned discipline.

Reese, Brandon J. (M.S., Electrical, Computer, and Energy Engineering)

The Local Bonding Environment of Amorphous In-Zn-O Films Studied by X-ray Absorption Fine

      Structure and Total X-ray Scattering Using Synchrotron Radiation

Thesis directed by Prof. Garret Moddel

Thesis co-directed by Dr. John D. Perkins, National Renewable Energy Laboratory

Amorphous transparent conducting oxides (a-TCOs) are a class of materials becoming increasingly important for their use in transparent electronic devices. Depending on the application, these materials can be tuned to behave as conductors, semiconductors, or even insulators. These materials have been gaining interest because they exhibit several desirable properties that are limiting factors in more common crystalline TCOs. The amorphous nature of these films means that they have no grain boundaries. This is beneficial because grain boundaries act as defects, decreasing the mobility of charge carriers in the material. Grain boundaries also provide a path for contaminants from the surrounding environment, such as water vapor, to transport through the films. This can be particularly detrimental to the performance of photovoltaics. Typically, these materials are very smooth and are mechanically robust, making them well suited for use in the emerging field of flexible electronics.

An archetypical a-TCO is amorphous indium zinc oxide (a-IZO). This material can be produced with a wide range of compositions and conductivities while not displaying any evidence of crystallization. The electrical and optical properties of a-IZO have been well characterized under a variety of different growth methods and conditions. Despite being well characterized from the standpoint of device performance, the structure of a-IZO has not, until recently, been thoroughly investigated. The native oxide of indium (In) is bixbyite, a cubic structure, while zinc (Zn) naturally crystallizes as wurtzite, a hexagonal structure. These two crystal structures are incompatible. It is believed that the inclusion of Zn atoms in IZO "frustrates" the crystal structure, hindering the creation of any long-range periodicity. This is because, when deposited at low temperatures,

both Zn and In try to form their respective native oxides. The structural description of sputtered a-IZO thin films is of interest for this work.

The amorphous nature of these materials means that any structural description will be statistical in nature, and traditional methods to measure structure, such as X-ray diffraction, will not be particularly illuminating. Despite the lack of long-range periodicity, a-TCOs still exhibit short-range ordering that closely resembles what would be expected in a crystalline material. Two methods well suited for structural determinations of amorphous materials are the Pair-Distribution Function (PDF), which is derived from the total scattering spectrum, and X-ray Absorption Fine Structure spectroscopy (XAFS). XAFS is capable of probing the structure of materials on very short ($\lesssim 5$ Å) length scales surrounding a specific element of interest. The PDF method is capable of probing the structure over longer distances than XAFS. Both techniques have strengths and weaknesses that will be discussed.

Both XAFS and PDF methods require highly monochromatic X-rays with widely tunable energy ranges and high fluxes. These requirements necessitate the use of synchrotron-based X-ray sources. Although synchrotron based measurements are becoming more routine in the scientific community, these methods still present significant difficulties in the determination and interpretation of results. The Stanford Synchrotron Radiation Lightsource and the Advanced Photon Source were both used in the collection of experimental data for this work.

Previous XAFS results from similar systems has shown that the oxygen coordination around each metal site is close to that of the native oxide, however current literature for XAFS analysis of a-IZO is lacking. The PDF results confirm that the arrangement of nearest and next-nearest neighbors in a-IZO is similar to what would be expected of crystalline In_2O_3. From the XAFS results, it has been concluded that InO_6 octahedra and ZnO_4 tetrahedra form edge-sharing linkages in a-IZO. Supporting this conclusion, EXAFS analysis provided a measure of the local cation (Zn/In) ratio which was consistent with the measurement of the bulk cation ratio.

Dedication

Dedicated to my loving family.

Acknowledgements

First, I would like the National Renewable Energy Laboratory and the staff of the National Center for Photovoltaics (NCPV). Thanks to Dave Ginley, John Perkins, Phil Parilla, Joe Berry, and everyone else at the NCPV for assisting and guiding me in this research. I thank Dan Miracle of the Air Force Research Laboratory for supporting this research and for engaging in innumerable conversations in the course of this project. Thanks to all of the members of the ifeffit and diffpy mailing list communities for providing with me with much appreciated advice and guidance in everything from software installation issues to practical advice on how to approach the scientific problems posed by this research. Thanks to Scott, for spending many hours sitting down with me, answering my random questions, and telling me which of my ideas were nonsense and how to follow the ones that were not.

Thanks to the staff at the Advanced Photon Source and the Stanford Synchrotron Radiation Laboratory, without whom none of these experiments could ever have happened.

I would also like to extend immense gratitude to my outside editors of this dissertation. Carrie, you are the best sister in the world. Ryan, thanks for making sure this paper made sense to someone other than me. Bob, thanks for running the dog.

Lastly, thanks to Kelly, Dylan, and Kleone. You have all supported me throughout graduate school and the writing of this dissertation more than words can express. Without your love and support none of this would have been possible. Thanks for being understanding of my obnoxious work habits and reminding me to take a break and sleep sometimes.

Contents

Chapter

Tables

Table

Figures

Figure

Chapter 1

Introduction

Transparent conducting oxides (TCOs) are an important and widespread class of materials. They are commonly used in flat panel displays, photovoltaic (PV)modules, light emitting diodes and transparent thin-film transistors [1, 2]. They serve a unique roll as a electrical contact that must also be transparent. Traditional TCOs can be characterized as substitutionally-doped wide band gap ($\sim$ 3 eV) semiconductors. The most commonly used TCO system is In_2O_3:Sn (indium tin oxide, or ITO), other common examples include ZnO:Al and SnO_2:F. Presently, materials such as ITO are commercially available with high conductivities ($\sim 10^4$ S/cm) and high transmittance ($>$ 85%) in the visible spectrum [3]. It has generally been considered that good crystallinity is a pre-requisite to obtain high-quality TCOs with these opto-electronic properties because grain boundaries and other impurities result in increased carrier scattering and decreased conductivity [4]. However, amorphous TCOs (a-TCOs) with no crystalline structure have been gaining popularity as a potential replacement for ITO. Common examples of a-TCOs include In-Zn-O (a-IZO), In-Ga-Zn-O (a-IGZO) and In-Zn-Sn-O (a-IZTO). However, many other compositions are being investigated as well [5–8]. Although numerous methods exist for producing a-TCOs, this work will focus on the structural characterization of a-IZO deposited with magnetron sputtering.

A driving force in a-TCOs gaining significant attention is in part because they exhibit many properties that are highly desirable from a device fabrication standpoint. Typically, a-TCOs are grown at ambient or low temperatures ($T < 100$ °C) and have remarkably smooth surfaces ($R_{RMS} < 0.5$ nm) while maintaining conductivities ($\sim$ 3000 S/cm) and visible transmittances

($>80\%$) approaching that of crystalline ITO [5]. The low growth temperature and smooth surface makes a-IZO a good candidate for applications using materials that can not be exposed to high temperatures, such as those found in organic light emitting diodes [9] or transparent thin film transistors [10]. Another aspect contributing to the interest in a-TCOs is the ability to easily tune the bulk properties of the film. The conductivity of the films varies with both In/Zn ratio and the O_2 present during film growth [11]. In the composition range of $\sim 55-85$ indium cation percent, sputtered IZO films typically remain amorphous. If no additional O_2 is added to the chamber during the deposition, conductivity peaks near the upper end of this range [5]. Outside of the amorphous composition range, the material begins to take on a crystalline structure. The grain boundaries in crystalline TCOs create pathways allowing the transport of contaminates, such as water vapor, to permeate the films. These environmental contaminants degrade the functionality of electronic devices. Amorphous TCOs, by definition, have no grain boundaries that can act as transport routes for contaminants, increasing the reliability of electronic devices in real world conditions [12].

Due to scarcity as a naturally occurring element, the price of ITO has risen due to the cost of the indium feedstock. The majority of the worlds' In supply is used to make ITO for various applications. At the beginning of the millennium, the price of In was a bit less than 200 \$/kg, after a short dip following the tech-crash in 2001, the price of In was over 900 \$/kg before recently dropping to near 600 \$/kg. The significant overall price increase is due to the rapid rise in demand of LCD televisions and touch screen electronics, many of which are manufactured using ITO [13–15]. The price volatility, with no indication of secession in demand, is another driving force behind researching new materials to bring down the manufacturing costs associated with ITO.

For PV applications a-IZO exhibits desirable properties compared to other typical TCO materials. The traditional TCO used for $Cu(In,Ga)Se_2$ solar cells is a combination of intrinsic ZnO and ZnO:Al. The biggest drawback of this system is when exposed to damp-heat[1] for 20 days the resistivity of ZnO:Al increases by a factor of more than 10^6. This is in comparison to a-IZO which shows no change over the same time period [16]. The most deposited TCO (by area)

---

[1] A typical PV testing condition defined as 85°C at 85% relative humidity.

is SnO_2:F (FTO), primarily used for energy-efficient ("low-e") windows. Although the low cost of FTO makes it desirable for large area applications, it requires high-temperature depositions (> 450 °C) to achieve the highest conductivity (~ 1500 S/cm), making it unsuitable for many PV systems [2]. At low-temperatures the most conductive FTO is only ~ 150 S/cm, making it too resistive for PV systems [17]. The IZTO system, when deposited at high-temperatures (> 450 °C) can reach conductivities of ~ 3000 S/cm, comparable to a-IZO. However, at low-temperatures the conductivity is typically about half of that value [18]. During device fabrication, a-IZO exhibits good etch characteristics, allowing smaller line widths compared a crystalline TCO, such as ITO [2].

1.1   The Structure of Amorphous-IZO

While worldwide research in a-TCOs has progressively grown, the majority of this research has focused on the characterization and control of bulk properties. It wasn't until recently that experimental methods sufficiently progressed to make measuring the atomic structure of these materials a reality. Upon first blush, talking about the structure of an amorphous material seems to be a misnomer. This is because structure is most often encountered when discussing crystalline materials where a few atoms are repeated indefinitely in all directions while maintaining an exact geometrical relationship with each other. By definition, amorphous materials do not possess this long-range periodicity, meaning that any structural descriptions must be statistical in nature. In addition, the exact meaning of "amorphous" is ambiguous, which poses the question: Does "amorphous" mean that the arrangement for every atom is completely random, or do the atoms posses local ordering on the scale of a few Å, or more?

In this work, two methods will be used to describe the structure of a-IZO thin films. Both rely on the use of high-energy X-rays only available at synchrotron radiation facilities. The first of these methods uses total scattering techniques to measure the Pair-Distribution Function, or PDF. These experiments are similar in nature to typical X-ray diffraction experiments, but the data is taken with some very specific considerations in mind and manipulated in such a way that a distribution of atomic distances can be obtained. The theoretical description of this technique and

the experimental results are presented in Chapter 3 and Chapter 4, respectively. PDF analysis of a-TCOs, in conjunction with molecular dynamics simulations, has recently been used in describing the atomic structure of these materials [19, 20].

The second technique used is X-ray Absorption Fine Structure spectroscopy, or XAFS. With this technique, the X-ray absorption as a function of energy is measured. The energy range used is such that an atom's core electron is excited during the course of the measurement, dramatically changing the absorption behavior of that particular element. As the X-ray energy is varied, the change in behavior is measured and can be related to the local atomic structure around that atom. The main results of this thesis deal with XAFS measurements. XAFS is a general term that describes a group of similar experiments, the theoretical description of which can be found in Chapter 6 and the results are presented and Chapters 7 and 8. Presently, XAFS analysis of TCOs has been limited to either crystalline TCOs [21, 22], or the description of nearest neighbors only for amorphous TCOs [7, 23, 24]. At this time, no work has been published showing evidence of next-nearest neighbor bonding arrangements using XAFS.

Chapter 2

Sample Preparation

2.1   Substrates

The substrates used for XAFS were 2×2 in. square Eagle 2000 (E2k) glass, produced by Corning[TM]. All E2k substrates were cleaned in Liquinox[TM] soap, a critical cleaning detergent, rinsed in deionized water and dried with a N_2 gun. A 10 minute ultrasonic bath in acetone followed by an isopropyl alcohol ultrasonic bath was them used to remove any oils still present. As a final step, the substrates were O_2 plasma cleaned for 5 minutes at 150 watts, removing any remaining residues.

Because the PDF portion of the experiment is much more sensitive to background effects, greater care had to be taken in creating suitable samples. Commercially available silicon nitride windows (pellicles) produced by Norcada were used as substrates.[1] The pellicle frame was a 7.5 x 7.5 mm^2 square piece of a 200 micron thick $\langle 100 \rangle$ oriented Si crystal. The top of the Si was coated with 100 nm of low-stress SiN. The Si was removed from a 2 x 2 mm^2 section in the center of the frame, leaving only the SiN. This resulted in a relatively robust sample that could be mounted on a variety of apparatuses and handled with tweezers, yet with a region of interest only 100 nm thick. The 2 mm square center region provided enough space for the X-ray beam to pass through it without any concern of a stray X-ray scattering off of the Si frame. These substrates are thoroughly cleaned and inspected by the manufacturer, so no additional preparation was necessary.

---

[1] Part #:NX7200C

2.2   Film Growth

All samples were deposited in the "Cube1" magnetron sputtering system at the National Renewable Energy Laboratory. It uses a sputter down configuration, with a sample stage rotating at 1 revolution/second. The gun was centered over the sample stage with a target to substrate distance of 2 inches. The sputter targets were produced by Cerac, and were specified according to weight ratio of In_2O_3/ZnO at purities >99.99%. The three concentrations used were 87/13, 80/20, and 70/30 (wt.%), approximately corresponding to 80/20, 70/30, 57/43 In/Zn atomic ratios. Atomic ratios will be used for the remainder of this thesis. The composition of the films was confirmed using X-ray fluorescence (XRF). The 70/30 and 57/43 samples were deposited using 4 inch gun at a power ratio of 25W RF/25W DC. Unfortunately, a suitable target of the 80/20 composition was only available in a 2 inch target. The 80/20 samples were deposited at 13WRF/13WDC. This power was chosen because it was the closest power density to that of the other two compositions that the power supplies would reliably operate. Although this is about a factor of 2 difference in power density, this is not anticipated to have a strong influence on the results of this work. E2k and pellicle samples were deposited simultaneously.

The sputtering system was turbo pumped until pressures of $< 3 \times 10^{-6}$ Torr were reached. The sputtering pressure was controlled by partially closing the gate valve until a steady pressure of 4.5 mTorr was achieved. For all samples Ar was flowed at 20 sccm. A MKS HPQ2 residual gas analyzer was used to measure the relative amount of gases present in the chamber before and during the entire deposition. The primary contaminant was water. The base level of water was dependent on the pump down time. The system pumped long enough that the oxygen present during depositions was typically a factor of five greater than the contaminants, with a ratio no smaller than a factor of two.

The oxygen content of the deposition was varied to provide a range of conductivities. Two samples of each composition were deposited, one "conductive" and one "intrinsic." Here, conductive refers to films grown with no additional O_2 added, and intrinsic refers to samples deposited with

added O_2. The "intrinsic" samples are not truly intrinsic, but simply a less conducting version of a-IZO. The terminology was chosen to provide a concise differentiation between the two types of samples. The conductive samples have a typical conductivity of ∼2000 S/cm, and the intrinsic samples had a range of conductivity from ∼ 60% of the conductive samples, to more than two orders of magnitude less than the conductive samples. A full matrix of compositions and conductivities was not made because the experimental time available at synchrotrons is limited.

2.3   Preliminary Characterization

Because this material is of interest as a TCO, the conductivity is an important metric. The thickness of the films was measured on a spectroscopic ellipsometer. The model used to determine the thickness was confirmed to be accurate by comparing the results with a profilometer measurement. The sheet resistance was measured using a standard 4-point probe method. The actual composition of the films was measured using X-ray fluorescence. The results of these measurements are summarized in Table 2.1. While it is recognized that in the context of TCO's some of the conductivity values of the intrinsic samples are actually quite conductive, a concise terminology to differentiate the sample sets was needed. For the remainder of this work, the samples will be referred to with their nominal atomic cation ratio and conductivity state, such as 80/20-C or 57/43-I.

To ensure that the films remained amorphous, X-ray diffraction was performed on a Bruker D8 Discover. The Bruker uses an area detector, thus any texturing present in the films should be apparent. The main broad scattering peak for all the samples was centered near $2\theta = 32°$, with a FWHM of ∼ 4°. The width of this peak puts the material into a gray area, it is not totally amorphous like a typical silica glass, but it is not crystalline either. The width of these peaks is sufficiently large that traditional structural analysis techniques are of little use.

Table 2.1: A summary of the physical properties of each sample. The sample is listed as nominal atomic ratio of In/Zn, as specified by the sputtering source used, in addition the state of the conductivity is listed as conductive (C) or intrinsic (I). The cation (In/Zn) ratio was calculated from the measured XRF concentrations, assuming stoichiometric In_2O_3 and ZnO. The O_2 content is the ratio of the O_2 content to the total gas content (O_2, Ar, N_2, and H_2O) during the deposition.

sample	wt.% (nom.)	XRF (wt.%)	In/Zn (cat.%)	O_2 (%)	t (nm)	σ (S/cm)
57/43-C	70/30	71/29	59/41	0.23	518	1862
57/43-I	70/30	70/30	58/42	0.98	497	514
70/30-C	80/20	80/20	70/30	0.25	563	2298
70/30-I	80/20	79/21	69/31	1.23	540	14
80/20-C	87/13	88/12	81/19	0.25	521	2315
80/20-I	87/13	90/10	84/16	1.37	508	1483

Chapter 3

Theory of Total Scattering and the Pair Distribution Function (PDF)

In typical X-ray diffraction (XRD) methods, it is assumed that all of the atoms are periodically arranged in a sample. The scattering intensity comes only from planes of atoms oriented parallel to the surface and is only observed at very specific locations (known as Bragg peaks), as defined by Bragg's law:

$$n\lambda = 2d \, \sin\theta. \tag{3.1}$$

The spacing between planes is d, θ is half of the angle between the incident and scattered beams, and n is an integer.

Even if an absolutely perfect crystal could be created, this assumption would not be strictly valid because thermal fluctuations and zero-point phenomena cause the atoms to vibrate. To account for some of these non-idealities, the Debye-Waller Factor (DWF)[1] was developed to approximate disorder effects [25]. In general, the DWF is dependent on the temperature of the sample and scattering angle, θ. It affects the **amplitude** of an observed diffraction peak. As the temperature or the scattering angle increase, the DWF grows, decreasing the observed intensity of the peak. But this intensity does not just disappear; it spreads out, asserting itself underneath and between the Bragg peaks. This type of scattering is referred to as **diffuse** scattering. Typically, diffuse scattering is considered part of the "background" and removed from the data. One of the factors affecting the **width** of a scattering peak is often attributed to the crystallite size. This effect is described using the Scherrer equation [26], which states that as the size of a crystallite is increased,

---

[1] Sometimes the DWF is simply referred to as the Temperature Factor

the width of a diffraction peak will decrease. For a thorough explanation of these terms, and the many other effects on the line shape in X-ray diffraction, see [27] and [25]. These corrections were developed to handle situations where the **fundamental** assumption of the Bragg equation, the periodicity of the atoms, was not perfect, but close. However, because the Bragg equation is so strongly dependent on this assumption, these corrections only work when **some** disorder is present. In systems where significant disorder is present the equations break down entirely.

3.1   Total Scattering

In general, the total signal measured in a scattering experiment (I_T) will be a combination of many different effects,

$$I_T = I_C + I_{IC} + I_{MS} + I_{bkg}, \tag{3.2}$$

where I_C is the coherently scattered intensity, I_{IC} is the incoherently scattered intensity, I_{MS} is the intensity due to multiple scattering events, and I_{bkg} is the scattering signal due to air, the optical path, etc. For further clarification of each of these terms, see Appendix A.1.

The coherent signal is of interest and can be expressed as $I_C = I_{Br} + I_D$, where I_{Br} is the intensity of a Bragg peak (Eq. 3.1), and I_D is the diffuse scattering intensity. In typical X-ray diffraction experiments, only the I_{Br} term is of interest, everything else is neglected as part of the "background." However, in **total scattering** techniques the diffuse scattering is also used in the determination of the structure. The following sections give a brief overview of total scattering methods and important derivations. For more complete explanations see [27], or *Underneath the Bragg Peaks* by Egami and Billinge [28], regarded as the seminal textbook on the subject.

3.1.1   Diffuse Scattering

By its very nature, diffuse scattering is very weak and difficult to measure. It is particularly apparent in the high-Q regions, where Q (defined in Eq. 3.8) has units of Å^{-1} and is proportional to the sine of the scattering angle, θ, and the X-ray energy. In this region the intensity of the scattering has spread out in between and underneath the Bragg peaks. In typical X-ray diffraction,

an approximation is made that this spread out intensity is simply part of the background. Figure 3.1 is an example of this spreading of the intensity, showing the diffraction data from In_2O_3 powder. The data is plotted as a function of Q, typical of total scattering experiments. This data is taken to $Q_{max} = 32$ Å^{-1}, whereas a typical laboratory XRD experiment using a Cu-$K\alpha$ source (8 keV, 1.55 Å X-rays) could only measure data to $Q_{max} \sim 8$ Å^{-1}. For a more rigorous explanation of the diffuse scattering see [28].
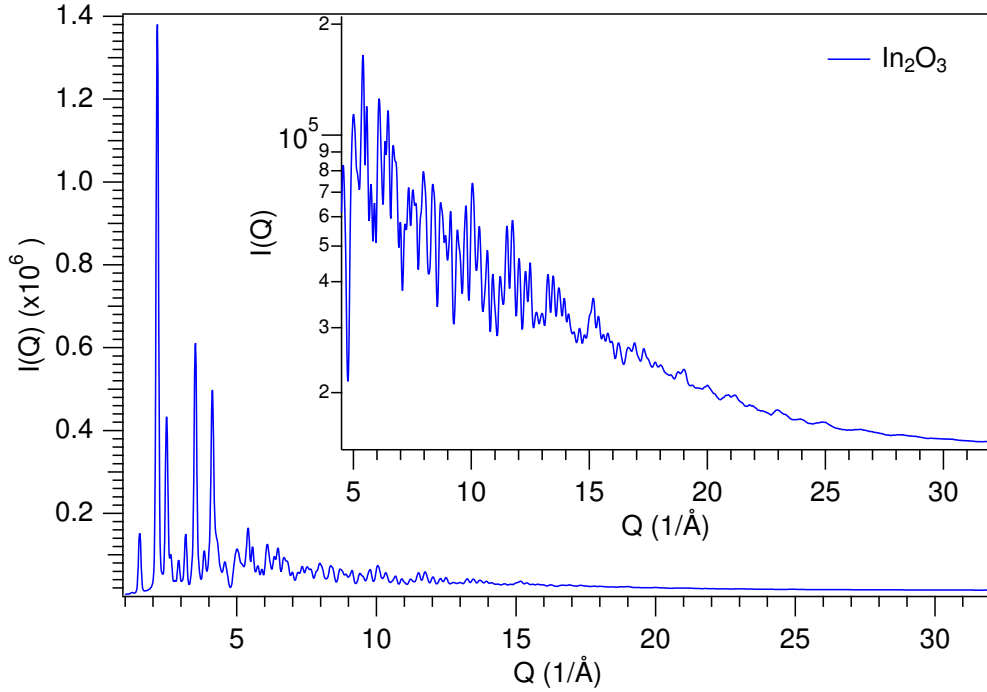
Figure 3.1: A powder In_2O_3 sample measured in transmission mode using 90 keV (0.137 Å) X-rays. Beyond the limit of laboratory X-rays, typically $Q \approx 8$ Å^{-1}, there is still a significant amount of information present (inset, log scale). However, the intensity of the peaks is severely reduced due to DWF effects. Typical X-ray diffraction ignores the high-Q region, whereas total scattering techniques require data going to very high Q.

3.1.1.1   The Total Scattering Amplitude - $\Psi(\mathbf{Q})$

The basic starting point for understanding total scattering methods is the expression for the total scattering amplitude (derived in Appendix A.2),

$$\Psi(\mathbf{Q}) = \frac{1}{\langle b \rangle} \sum_{\nu} b_{\nu} e^{i\mathbf{Q}\mathbf{r}_{\nu}}, \tag{3.3}$$

where b_{ν} is the scattering amplitude of the νth atom, $\mathbf{r}_{\nu}$ is the vector to that atom, and $\langle b \rangle$ is the compositional average of the scattering power,

$$\langle b \rangle = \frac{1}{N} \sum_{\nu} b_{\nu} = \sum_{\alpha} c_{\alpha} b_{\alpha}, \tag{3.4}$$

where ν represents the sum over all atoms. For X-rays this term is dependent on $|\mathbf{Q}|$, but this explicit dependence is left out for simplicity. In practice, the last expression is most usable where the sum is over each atomic species, α, and c_{α} is the atomic concentration of each atomic species. The diffraction vector, $\mathbf{Q}$, is defined as:

$$\mathbf{Q} \equiv \mathbf{k}_i - \mathbf{k}_f, \tag{3.5}$$

where $\mathbf{k}_i$ and $\mathbf{k}_f$ are the initial and final wavevectors, respectively. The magnitude of the wavevectors is

$$k = |\mathbf{k}_{i,f}| = \frac{\tau}{\lambda_{i,f}}, \tag{3.6}$$

where λ is the wavelength of the X-ray and[2]

$$\tau \equiv 2\pi. \tag{3.7}$$

From this expression, with the assumption of elastic scattering $(\lambda_i = \lambda_f)$, comes the important relation,

$$Q \equiv |\mathbf{Q}| = 2k \sin\theta = \frac{2\tau \sin\theta}{\lambda}, \tag{3.8}$$

where θ is half of the angle between the incident and scattered X-rays. The relevant quantity in many scattering experiments is the magnitude of the diffraction vector, Q, not the vector itself.

---

[2] For a philosophical justification of $\tau \equiv 2\pi$, see http://tauday.com/ [accessed: July 26, 2011] or [29].

This is because many systems such as amorphous solids, liquids, and powdered crystals scatter isotropically; meaning that the scattering is equally probable in all directions. For the remainder of this thesis, this assumption is made. This definition also allows a connection to the Bragg equation (Eq. 3.1, with $n = 1$), rewriting this equation yields

$$d \;=\; \frac{\lambda}{2\sin\theta} \tag{3.9}$$

$$\;=\; \frac{\tau}{Q}. \tag{3.10}$$

This provides a connection of total scattering methods with typical crystallography. While crystallography is typically interested in the spacing between atomic planes, d, for amorphous systems defining the spacing between planes does not make sense. However, Q plays an additional role in total scattering methods, as will be discussed in section 3.2.2.

3.1.1.2 The Structure Function - $S(Q)$

Equation 3.3 accounts for the coherently scattered amplitude from every atom in the sample. By writing this equation as

$$\Psi(\mathbf{Q}) = \sum_{\nu} F(\mathbf{r}_\nu) e^{i\mathbf{Q}\mathbf{r}_\nu}, \tag{3.11}$$

it can be seen that the scattering amplitude is the Fourier transform of $\mathbf{r}_\nu$, the atomic positions in the atom. Therefore if we measure the scattering amplitude and take the Fourier transform, an exact representation of atomic positions is obtained. However, in any real scattering experiment the scattered amplitude can never be measured, only the intensity, which is proportional to the square of the amplitude.

Scattered X-rays are emitted in every direction from the sample, but practical considerations mean that only a portion of this space can be measured. In addition, not all of these X-rays contain structural information. An actual scattering experiment measures the scattering cross-section,

$$\frac{d\sigma_c(Q)}{d\Omega} = \frac{\langle b \rangle^2}{N} |\Psi(Q)|^2, \tag{3.12}$$

where N is the number of atoms and the subscripted c indicates being only interested in the coherent scattering from the sample. A derivation of this expression can be found in Appendix

A.3. Because of the isotropic scattering assumption, this term is dependent only on the magnitude of the scattering vector, Q, not the vector itself, $\mathbf{Q}$. The measured intensity can be expressed as

$$I(Q) = \frac{d\sigma_c(Q)}{d\Omega} + \langle b \rangle^2 - \langle b^2 \rangle, \tag{3.13}$$

where the additional term, $\langle b \rangle^2 - \langle b^2 \rangle$, is referred to as the Laue monotonic scattering. This is an elastic, incoherent scattering that we are not interested in. This unwanted term is explicity included because at large Q, $d\sigma_c(Q)/d\Omega$ approaches $\langle b^2 \rangle$. Finally, defining the **total scattering structure function**,[3]

$$S(Q) = \frac{I(Q)}{\langle b \rangle^2} \tag{3.14}$$

From this definition it can be seen that as $Q \to \infty$, $S(Q) \to 1$.

3.2 The Pair Distribution Function - $g(r)$

The pair distribution function (PDF) is the Fourier transform of $S(Q)$. It utilizes a wide range in Q-space that, when Fourier transformed, produces a spectrum in r-space. This section will first give a qualitative description of the PDF, then derive a simple expression for the PDF.

3.2.1 Qualitative Description of the PDF

With total scattering methods, the goal is to measure the number of atoms in a spherical shell of radius r and thickness dr from a particular origin. This very intuitive idea is often what is used in describing the principle of the PDF. However, strictly speaking this is the **radial distribution function** which is defined as

$$T(r) = 2\tau r^2 \rho_0 g(r) = \frac{1}{N} \sum_n \sum_m \delta(r - r_{nm}), \tag{3.15}$$

where ρ_0 is the number density of the system of N atoms, δ is the Dirac delta function, r_{nm} is the distance between atoms n and m, and $g(r)$ is the **pair distribution function**. If we integrate $T(r)$

---

[3] It is important to note that sometimes the literature refers to this term as the structure **factor**. Here, this a term that scales with the **intensity**, where as in typical crystallography, the structure factor refers to a term that scales the **amplitude**, as in Eq. A.8.

between r_1 and r_2, the result will give the number of atoms between those distances. Essentially, $T(r)$ is a histogram of interatomic distances. Both $T(r)$ and $g(r)$ are one of many functions that get lumped into the general idea of the PDF [30]. Generally these functions generally all contain the same information, but display it differently.

Using $T(r)$ has the drawback in that it diverges as r^2, making it useful to display data only over short r ranges. The pair-distribution function, $g(r)$, has the property that as $r \to 0$, $g(r) \to 0$, and as $r \to \infty$, $g(r) \to 1$. However, $g(r)$ has the drawback that it naturally decays as $1/r$, this makes it less clear if peak amplitudes are diminishing because the structure is losing coherence, or if it is merely due to the nature of the function. Also, when fitting a structural model to $g(r)$ the error bars scale as $1/r$, making it difficult to determine the accuracy of the fit in different r ranges.

Another related function is the **reduced pair distribution function**, defined as

$$G(r) = 2\tau r \rho_0 (g(r) - 1). \tag{3.16}$$

This function oscillates around zero and ideally any change in peak amplitude is due to a loss of structural coherence. Strictly speaking, real data will show decay because of the finite Q_{max}, but it is much slower than $1/r$. With modern synchrotrons data can easily be obtained to very high Q, minimizing the effects of Q_{max} being finite. This function also is a direct representation of the Fourier transform of the data. No *a-priori* parameters, such as ρ_0, must be input which helps reduce systematic errors. Ideally, as $r \to 0$, $G(r)$ is a line with a slope of $-2\tau r \rho_0$, so the number density, ρ_0, can be extracted. It also has the advantage that when fitting to a model, the uncertainties are constant in r. This makes it easier to judge the accuracy of a model over a wide data range. Although plots of this data are less physically intuitive, it is commonly used in the literature, and it is what will be used in this work. For simplicity, $G(r)$ will be referred to as the pair distribution function (PDF), rather than the reduced PDF.

3.2.2   Derivation of the PDF

Starting with the definition for the sample scattering amplitude (Eq. 3.3),

$$\Psi(\mathbf{Q}) = \frac{1}{\langle b \rangle} \sum_{\nu} b_{\nu} e^{i\mathbf{Q}\mathbf{r}_{\nu}}. \tag{3.17}$$

We will assume that all atoms have equal scattering power, meaning that $b_{\nu} = \langle b \rangle N$. The atomic density function, $\rho_a(\mathbf{r})$, can be defined as

$$N = \int_V \rho_a(\mathbf{r}) \ d\mathbf{r}. \tag{3.18}$$

Incorporating this equation into Eq. 3.17 and changing the sum to an integral, results in

$$\Psi(\mathbf{Q}) = \int \rho_a(\mathbf{r}) e^{i\mathbf{Q}\mathbf{r}} \ d\mathbf{r}. \tag{3.19}$$

Plugging this into the definition of the structure function (Eq. 3.14) yields

$$S(\mathbf{Q}) = \frac{1}{N} |\Psi(\mathbf{Q})|^2 = \frac{1}{N} \int \int \rho_a(\mathbf{r}) \rho_a(\mathbf{r}') e^{i\mathbf{Q}(\mathbf{r}-\mathbf{r}')} \ d\mathbf{r} \ d\mathbf{r}'. \tag{3.20}$$

The PDF is defined as being the Fourier transform of the scattering function, therefore

$$FT[S(\mathbf{Q})] = \rho_0 g(r) = \frac{1}{\tau^3} \int S(\mathbf{Q}) e^{i\mathbf{Q}\mathbf{r}} \ d\mathbf{Q}, \tag{3.21}$$

where the ρ_0 is the number density of the material and $g(r)$ is the pair distribution function. Using the assumption of isotropic scattering,

$$= \frac{1}{\tau^3} \int_0^{\infty} \int_{-1}^{1} \int_0^{\tau} S(Q) e^{iQr\cos\theta} \ d\phi \ d(\cos\theta) \ Q^2 \ dQ \tag{3.22}$$

$$= \frac{1}{\tau^2} \int_0^{\infty} \int_{-1}^{1} S(Q) e^{iQr\cos\theta} d(\cos\theta) \ Q^2 \ dQ \tag{3.23}$$

$$= \frac{1}{\tau^2} \int_0^{\infty} S(Q) \frac{\sin Qr}{Qr} Q^2 \ dQ \tag{3.24}$$

$$\rho_0 g(r) = \frac{1}{\tau^2 r} \int_0^{\infty} S(Q) \sin(Qr) Q \ dQ. \tag{3.25}$$

The last equality shows that the Fourier transform of the scattering function is the pair distribution function.

In a real measurement, we cannot obtain information out to arbitrarily high-Q, therefore the integral must be truncated at Q_{max}. Because $S(Q)$ oscillates around one, this would result in $g(r)$ being strongly dependent on where the integral was truncated. To help alleviate this problem, unity is subtracted from $S(Q)$ and $g(r)$. With a slight rearrangement this results in

$$2\tau r \rho_0 (g(r) - 1) = \frac{4}{\tau} \int_0^{Q_{max}} Q(S(Q) - 1) \sin(Qr) \, dQ \tag{3.26}$$

$$G(r) = \frac{4}{\tau} \int_0^{Q_{max}} F(Q) \sin(Qr) \, dQ, \tag{3.27}$$

where

$$G(r) \equiv 2\tau r \rho_0 (g(r) - 1) \tag{3.28}$$

$$F(Q) \equiv Q(S(Q) - 1). \tag{3.29}$$

$F(Q)$ is referred to as the **reduced** structure function, and $G(r)$ is the **reduced** PDF. Truncating the Fourier transform at a finite value produces transform ripples with a wavelength of τ/Q_{max}. If Q_{max} is too low, the PDF peaks will be broadened and termination ripples will be large. As Q_{max} is increased, the oscillations of $F(Q)$ become very weak, decreasing the amplitude of the ripples. This is one reason why it is important for PDF experiments to measure out to high values of Q. The other reason is that the high-Q region still contains structural information, and not including this region means not including information about the structure that is trying to be measured. A plot of $F(Q)$ and $G(r)$ are shown in top and bottom panels of Fig. 3.2, respectively. The accuracy of the PDF method is immediately apparent in the bottom panel of Fig. 3.2, where an ideally calculated PDF is already an excellent match to the data, even prior to any fitting.

3.3   Concluding Remarks

This chapter has shown that by using total X-ray scattering techniques, one is able to produce a direct real space map of interatomic distances, the PDF. This technique is equally applicable to amorphous and crystalline forms of matter. PDF experiments use a wide Q-range, which is not accessible by standard X-ray diffraction equipment.
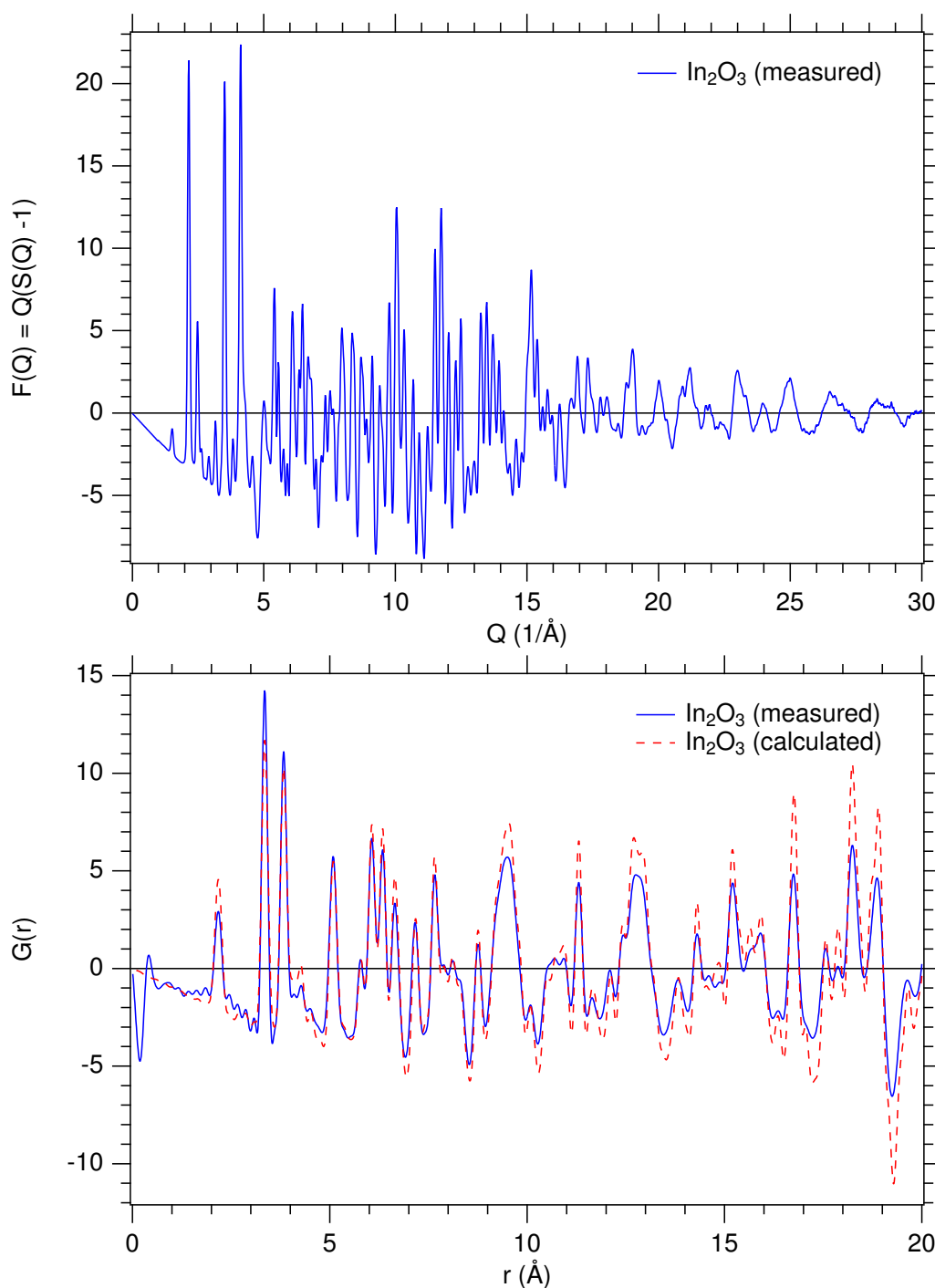
Figure 3.2: (top) The reduced structure function, $F(Q)$, of powder In_2O_3. A significant amount of information is present beyond 8 Å^{-1}, the limit of most laboratory X-ray sources. (bottom) The PDF of the powder In_2O_3 sample (blue) and a theoretically calculated In_2O_3 PDF (dashed red). The spike near zero in the measured PDF is due to an imperfect background subtraction. As an example of the accuracy of the PDF technique, the theoretically calculated PDF **was not** fit to the data. The calculated PDF was generated using PDFGUI [31] and a theoretical In_2O_3 crystal structure [32]. Even with all of the real world effects present during an experiment, the measured PDF is very close to the ideal PDF.

Chapter 4

PDF Experiments

4.1   Data Collection and Reduction

Pair distribution function measurements were carried out at the Advanced Photon Source (APS) using beamline 11-ID-B. This is a dedicated PDF beamline operating at 90 keV (0.137 Å). The detector was a 16 x 16 inch^2 Perkins-Elmer a-Si area detector, with a sample-to-detector distance of $\sim$ 215 mm. Flat-plate transmission geometry was used, which is where the sample is stationary and normal to the X-ray beam. This configuration limited our measurement to $Q_{max} = 32$ Å^{-1} ($2\theta \approx 41°$). Because of signal-to-noise issues, the functional limit was $Q_{max} = 18$ Å^{-1}.

The data is collected as a tiff image file that has been corrected for dark current and geometrical effects arising from the use of an area detector. Multiple images were then averaged and integrated using the program FIT2D, where artifacts such as the beam block and dead pixels were masked from the integration region [33,34]. This program has built-in routines to calibrate parameters such as the detector distance, detector tilt, etc [35]. For this calibration, a LaB$_6$ standard was used in a similar form factor to the pellicle samples. The step size used for integration was $\sim$ 0.06 Å^{-1}. A pristine pellicle sample was measured for 5 hours to act as a background sample for the deposited films. The films were each measured for 2 hours. A typical plot of the integrated scattering data can be seen in Fig. 4.1.

The integrated intensities were processed into PDF's using PDFGETX2 [36]. It was mentioned in section 3.1.1.2 that the quantity of interest is the scattering cross section. A simple form for this
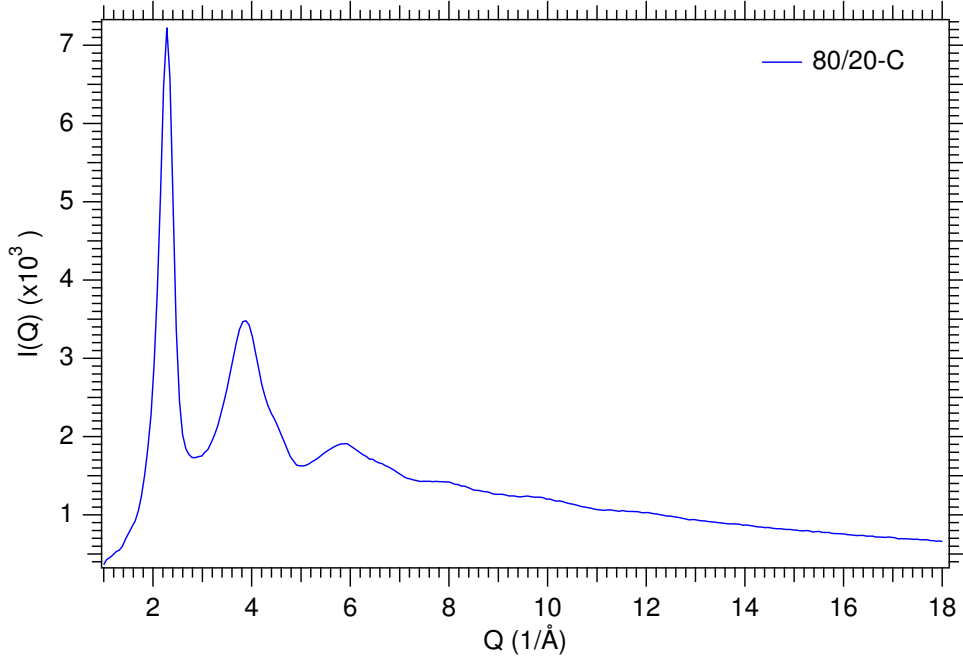
Figure 4.1: Integrated scattering data as a function of Q after background subtraction. Data is representative of typical a-IZO films.

expression was presented in Eq. 3.12. A more general expression for this parameter is

$$\frac{d\sigma_c(Q)}{d\Omega} = \left(N_s - V'_{bkg}N_{bkd}\right)\left(\frac{1}{P_iV'_s}\right)\frac{1}{\rho_s d\Omega K\epsilon_d} - N_{MS} - N_{IC}, \tag{4.1}$$

where N_s and N_{bkd} represent the normalized and deadtime corrected counts of the sample and background, respectively. The terms V'_s and V'_{bgd} are the effective scattering volumes of the sample and background, and the number density of the sample is given by ρ_s. The efficiency of the detector and I_0 ion chamber are given by ϵ_d and K, respectively. The polarization of the X-rays is given by P_i, for synchrotron radiation the beam is roughly 95% polarized. Multiple scattering contributions are expressed as N_{MS}, and the Compton (incoherent) scattering is N_{IC}. The multiple scattering is a strong function of the total absorption (μ_T) of the sample; the larger the absorption, the larger effect N_{MS} has on the data. If $\mu_T \approx 1$, the total multiple scattering intensity will be about 4% of the total signal. For our films $\mu_T \sim 10^{-5}$, so multiple scattering can safely be ignored. This same argument is true for the scattering volumes.

All of the terms can be calculated or measured, except for $\rho_s d\Omega K\epsilon_d$. We know from section

3.1.1.2 that as $Q \to \infty$, $d\sigma_c(Q)/d\Omega \to \langle b^2 \rangle$. Defining the unknown terms as β, and assuming they don't vary with Q, Eq. 4.1 can be written as

$$\beta = \lim_{Q \to Q_{max}} \frac{(N_s - N_{bgd})}{P_i \left(\langle b^2 \rangle + N_{IC} \right)}. \tag{4.2}$$

This expression for β can be evaluated. The expression for the cross section can now be written as

$$\frac{d\sigma_c(Q)}{d\Omega} = (N_s - N_{bkg}) \left(\frac{1}{P_i \beta} \right) - n_{inc}. \tag{4.3}$$

From this the structure function and the PDF can be now be calculated as in sections 3.1 and 3.2.

4.1.1   Lorch Damping Function

By their nature, amorphous systems are weakly scattering, even in the low-Q region where peaks are easily observable. In high-Q regions, the signal-to-noise ratio presents a major obstacle in creating high quality PDF's. The signal-to-noise ratio also makes the proper normalization of F(Q) difficult, resulting in Fourier transform ripples that can significantly corrupt the data. A solution to both of these problems is to multiply $F(Q)$ by the Lorch function [37], defined as

$$M(Q) = \frac{\sin(\pi Q/Q_{max})}{\pi Q/Q_{max}}. \tag{4.4}$$

This function is equal to unity at $Q = 0$, and slowly decreases until it is equal to zero at $Q = Q_{max}$. This serves to both decrease the amplitude of the noise at high-Q, and to force $F(Q_{max}) = 0$.

This function is commonly used in amorphous systems and glasses [38–40]. The top panel of Fig. 4.2 shows two $F(Q)$ traces for the 80/20-C sample with and without the Lorch function. It is immediately clear that amount of noise in the high-Q regions is significantly damped, but the changes to the low-Q region are minimal. The bottom panel of Fig. 4.2 (bottom) shows $G(r)$ with and without the Lorch function. It is immediately evident that the decrease in noise significantly improved the termination ripples. The degree of signal present at extended r is striking. For a typical glass, such as our E2k substrates, the PDF signal is within the noise after about 5 Å. This indicates that some ordering is still present on the length scale of 1-2 nm.
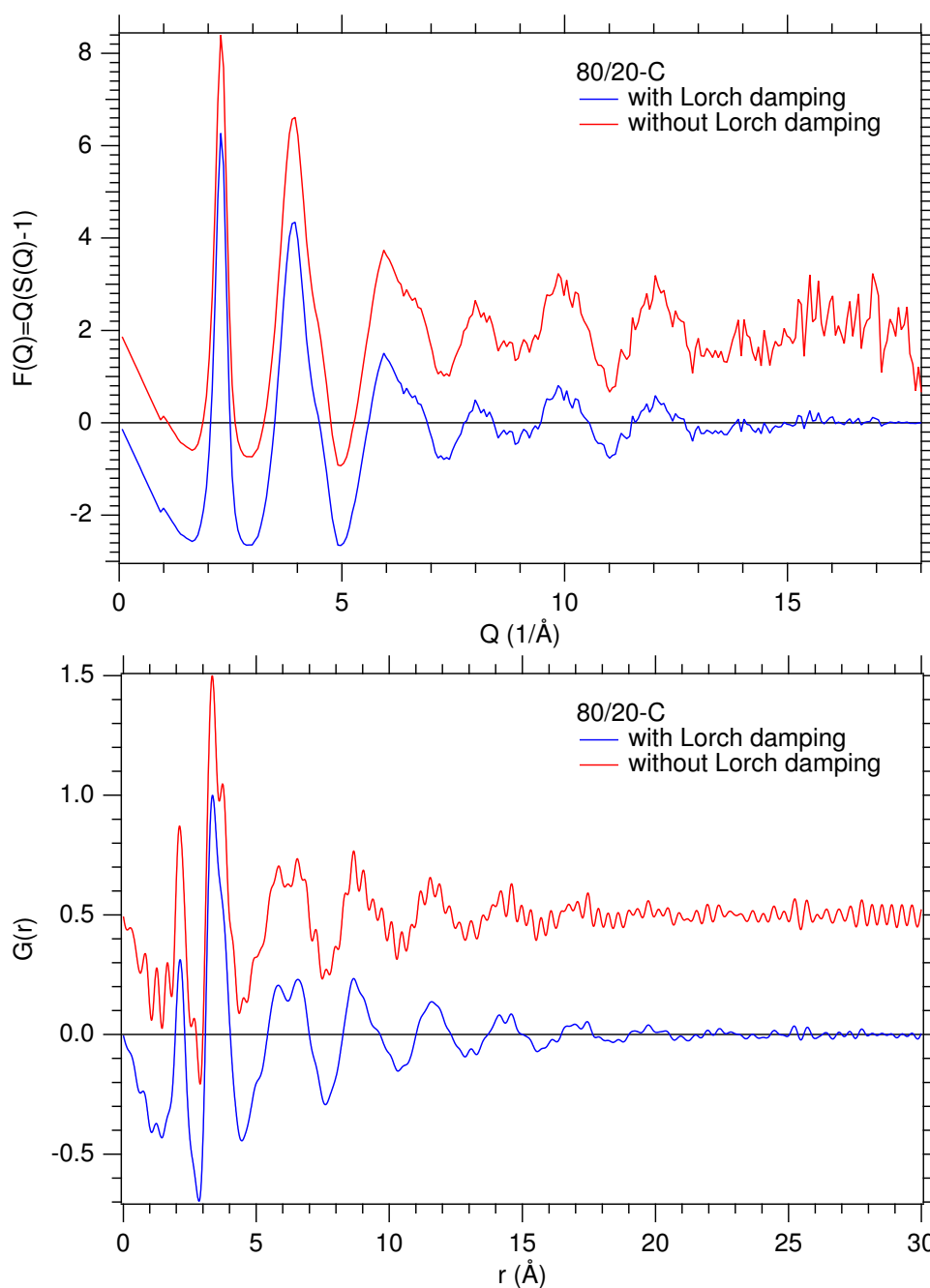
Figure 4.2: (top) $F(Q)$ plots for the 80/20-C sample with (blue) and without (red) the Lorch function. The function without the Lorch has been offset for clarity. It is immediately evident the Lorch function is significantly attenuating the signal in the high-Q region. (bottom) The PDFs of the same sample. Fourier ripples are present in both plots. However, the PDF where the Lorch was not applied has significant contributions from Fourier ripples throughout the spectrum, although it does maintain the same general trends as the PDF with the Lorch function. The PDFs have been normalized to unity for easier comparison.

4.2   PDF results

4.2.1   PDF of Amorphous IZO Films

The gathering of reliable PDF data was a very laborious and experimentally intensive task. Many trips were taken to the Stanford Synchrotron Radiation Laboratory (SSRL) where only valuable experience was obtained. Being awarded beamtime at APS proved to be a turning point for the PDF portion of this project. However, because of time constraints none of the PDF data could be analyzed. Since PDF's are direct representations of atomic radial distributions, the data from the IZO films is presented to add a qualitative sense to the structural nature of these materials.

Figure 4.3 shows the same PDF as pictured in the bottom panel of Fig. 4.2, but overlaid with theoretical PDF's of both In_2O_3 and ZnO. The similarity of the peaks at 2.1 and 3.4 Å is striking. The match in position, particularly between the peak at 3.4 Å and In_2O_3 spectra, indicates that modeling these structures as something similar to In_2O_3 would be justified. The width of the peaks indicates that there is a significant spread in the interatomic distances.

In the top panel of Fig. 4.4, the three conductive samples are compared. There are no strong trends, but the features at 3.6, 5.2, and 8.0 Å do trend with the composition of the films. The 80/20-C sample had the best background removal, as can be seen by the gently oscillating line below $r \sim 1.75$. The larger oscillations present in this same region of the other samples indicates that a low-frequency spine shape is present in $F(Q)$, rather than it truly oscillating around zero. The bottom panel of Fig. 4.4 compares the three insulating samples. The trend with composition is similar to that of the conductive films at 3.6 and 8.0 Å. There is also a trend with conductivity in the features at 2.2 and 6.0 Å. When overlaying the intrinsic samples with the conductive films (not pictured), the only consistent trend is that the conductive films have a slight increase in the peak height of the In-O shell at 2.1 Å when compared to the intrinsic films. Both of these sets of data show a consistent change with In content at 2.8 Å, a region corresponding to corner-sharing octahedral units.
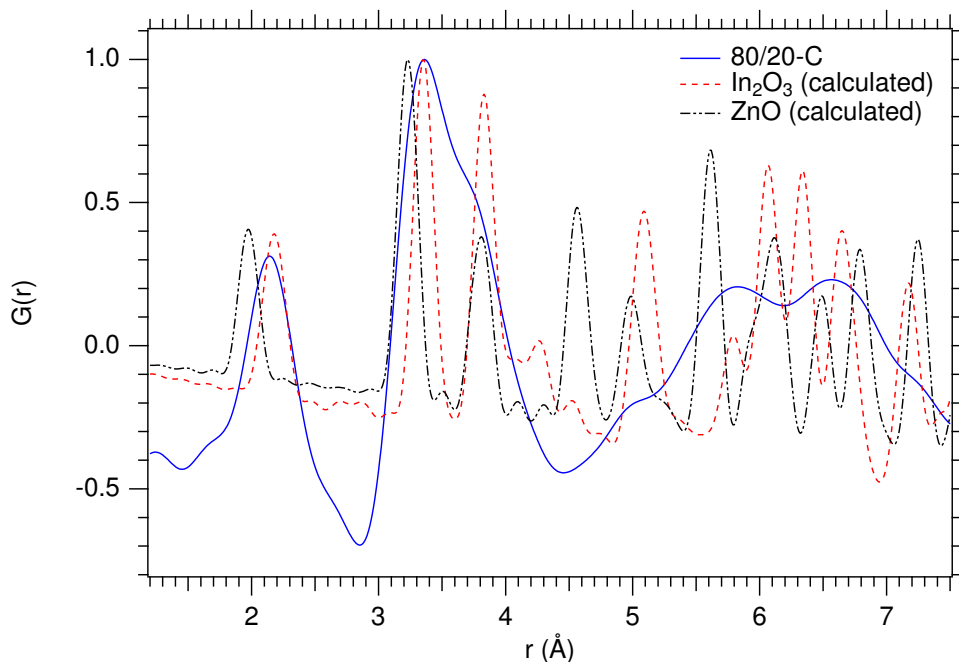
Figure 4.3: Comparison of the PDFs from a typical IZO sample and theoretically calculated oxide references of In_2O_3 and ZnO [32]. The similarity in the peaks at 2.1 and 3.4 Å indicates this structure is similar to that of crystalline In_2O_3. The theoretical In_2O_3 peaks at 3.4 and 3.8 Å correspond the edge and vertex sharing In-centered octahedrons, respectively.

4.2.2 PDF of Amorphous IZO Powder

One additional sample that was made for PDF measurements is worthy of discussion. It was an 80/20 IZO film deposited on E2k glass with a thickness of ~ 1 μm. For unknown reasons this film delaminated from the substrate. The fragments were collected, and ground into a fine powder using a mortar and pestle. This powder was scooped into a capillary tube made of Kapton with an ID=1.02 mm.[1] Kapton capillaries are the standard way that data is collected at 11-ID-B. Loading the sample into a capillary increases the effective thickness, and thus the signal strength, by a factor of ~ 2000. The top panel of Fig. 4.5 shows the $F(Q)$ data from a 80/20 sample measured on a pellicle and in a capillary tube. The pellicle sample is the same one shown in Fig. 4.2. The difference in the noise level is substantial; especially considering the pellicle sample represents seven hours of data collection (sample and background), whereas the capillary sample represents only 20

---

[1] Cole-Palmer part #: EW-95820-09

Figure 4.4: (top) Comparison of the PDFs from the conducting group of samples. Although weak, there is a trend with composition at 3.6, 5.2, and 8.0 Å. (bottom) Comparison of the PDFs from the intrinsic group of samples. The compositional trends relative to the conductive films are similar. There is also a trend with conductivity at 2.1 and 6.0 Å. The large oscillations at low-r are indicative of a poor normalization process. The 80/20-C sample is an excellent example of a proper normalization. Both panels use identical vertical and horizontal scales. The main peak (3.4 Å) for all the plots has been scaled to unity for comparison purposes.

minutes! The bottom panel of Fig. 4.5 shows the PDF data of the two samples. The PDF of the capillary sample follows a similar trend to the pellicle sample, but there are differences. There is the appearance of the shoulder at 3.7 Å and a narrowing of the peak at 2.1 Å. Although not readily visible on this scale, the transform ripples become apparent on the capillary sample around 20 Å.

4.3   Concluding Remarks

Although time constraints have the prevented the proper modeling of the PDFs presented, several qualitative conclusions can be drawn. The first is that the PDF results for a-IZO displays a general structural behavior that resembles the ideal crystal structure of In_2O_3. Secondly, both the conductive and intrinsic PDFs show a small, yet consistent, trend as a function of composition. The region near 3.8 Å, corresponding to vertex-sharing polyhedra in In_2O_3, tends to decrease with decreasing In content. This is consistent with what is found in the literature [19, 20]. Lastly, it has also been demonstrated that performing the experiment on powdered samples, rather than film, yields small yet significant differences in the results. If a full composition spread of powders could be measured, the increased resolution of the measurements would provide more definite trends in the behavior of these films.
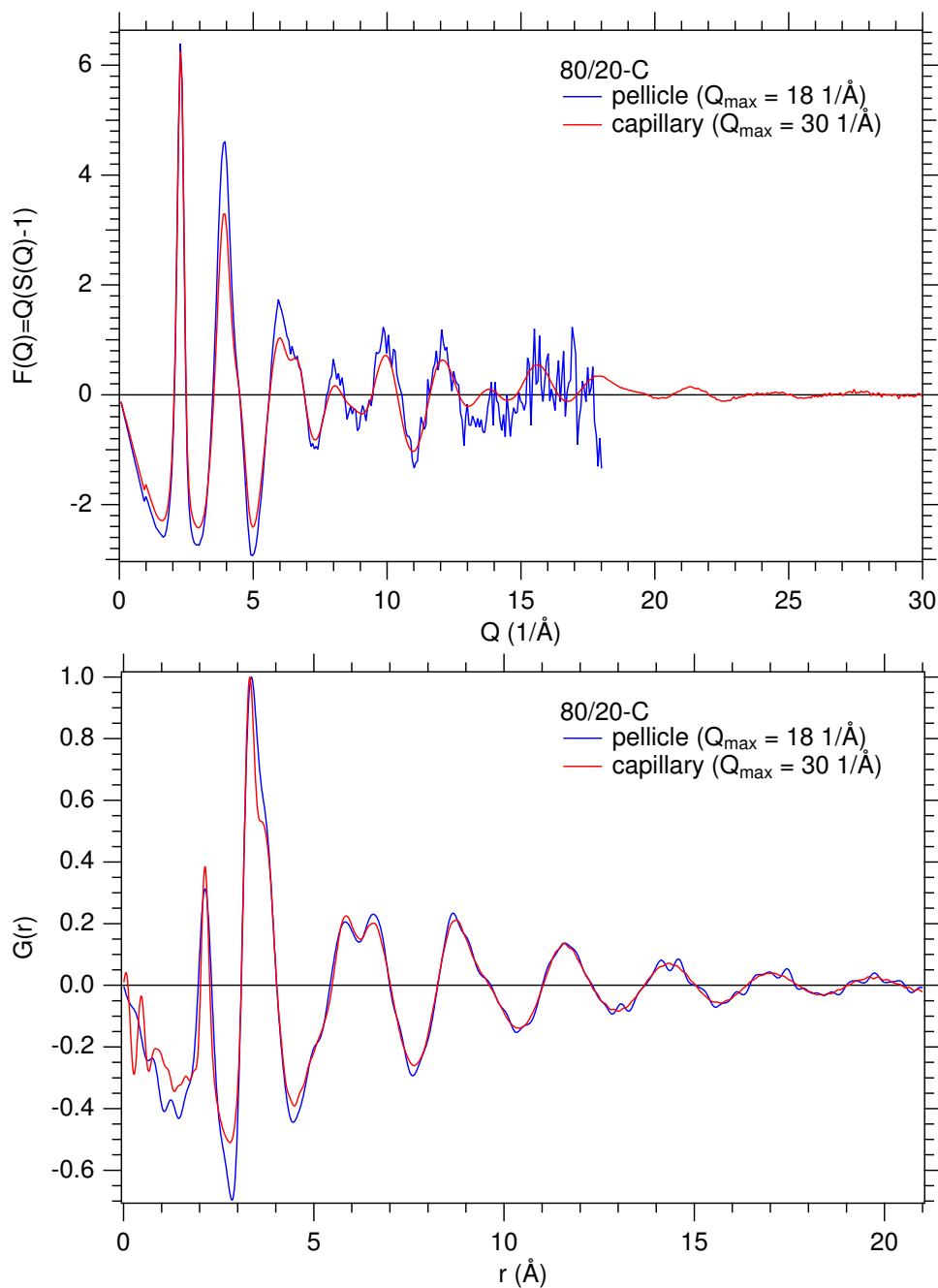
Figure 4.5: (top) Comparison of $F(Q)$ spectra for a capillary sample compared to the standard pellicle substrate. Both samples have a composition of 80/20 In/Zn (atomic %). The $F(Q)$ for the pellicle is not damped to illustrate the scale of the noise difference. (bottom) The PDFs of the same two samples. The PDF of the pellicle used Lorch damping to minimize the noise.

Chapter 5

Theory of X-ray Absorption Fine Structure (XAFS)

5.1   Background

One of the many processes that can occur when an X-ray interacts with an atom is the complete absorption of the X-ray, transferring all of its energy into the atom. The atom uses this energy to excite an electron to a higher unoccupied orbital or, if the energy is high enough, the electron will be ejected into the continuum, dissociating the electron from the atom and creating a hole state in the atom. After ejection into the continuum, the electron is referred to as a photoelectron.

The electronic orbitals, or "shells," are named based on their principle quantum number, n. If an electron is in the $n = 1$ state, it is referred to as being in the K-shell. If $n = 2$, the electron is in the L-shell. The azimuthal (ℓ) and angular momentum (j) quantum numbers determine how many sub-shells exist with the same quantum number. The number of sub-shells, and the ability for electrons to transfer between them, is governed by quantum transition rules [41]. The binding energies of each shell for every element is unique and well documented [42]. It is the uniqueness of these energies that gives XAFS the ability to probe materials in an element-specific way.

The probability for an absorption event to occur is given by μ, the linear absorption coefficient. The absorption coefficient is generally a slowly decaying function of X-ray energy. When the incident X-ray energy reaches the binding energy of any of the electronic orbitals a sudden increase in μ is observed. This is referred to as an absorption edge and was first observed in 1913 by Louis de Broglie's older brother, Maurice [43]. In 1920, it was observed that the region immediately after an absorption edge showed complex features [44, 45]. It was not realized until 1971, when

these complex features were Fourier transformed, that they could be used to describe the atomic structure of materials [46]. It was several more years until development began on what has come to be known as the modern theory of XAFS [47,48].

Experiments where the X-ray absorption coefficient as a function of energy, $\mu(E)$, is measured are referred to as XAFS measurements. XAFS measurements are typically performed at energies such that the K- or L-shells are excited, and are referred to as K- or L-edge measurements. The energy of the edge-step is referred to as E_0. The ultimate goal of XAFS is to extract the details of the local structural environment surrounding an atom.

5.1.1 Basic Measurement Principles

There are two basic modes of XAFS measurements: transmission and fluorescence. Each mode has advantages and disadvantages. All else being equal, transmission mode is generally preferred due to simpler experimental interpretation and higher signal-to-noise ratios. However, one drawback is that the thickness of the samples needs to be optimized to avoid experimental artifacts. Fluorescence mode measurements are preferable if the sample cannot be sufficiently thinned for use in transmission. The use of energy-discriminating detectors means that concentrations in the low-ppm range can be measured in fluorescence [49], where this would be extremely difficult in transmission mode.

5.1.1.1 Transmission

When performing XAFS measurements, results are interpreted by making use of Beer's Law:

$$I_t = I_0 e^{-\mu_t(E)x}, \tag{5.1}$$

where I_t and I_0 are the transmitted and incident X-ray intensities, respectively, x is the thickness of the sample, and μ_t is the linear absorption coefficient in transmission mode, with the subscripted t representing the transmission measurement mode. I_0 and I_t are also dependent on energy, but

that dependance is left as implicit, for simplicity. A little rearrangement yields the simple relation

$$\mu_t(E)x = \ln\left(\frac{I_0}{I_t}\right). \tag{5.2}$$

This quantity is directly measured in a transmission mode XAFS experiment, making these measurements relatively simple to perform and to understand.

5.1.1.2   Fluorescence

In fluorescence mode measurements $\mu_t(E)$ can only be measured indirectly. A very short time, $\sim 10^{-15}$ s after the creation of a photoelectron, the hole state that was created gets filled by another electron from a higher orbital. It is filled according to the quantum selection rules regarding electron transitions. Energy is released during this transition, referred to as fluorescence, equal to the difference in energy between the two states. Because electron orbital energies are unique to each element, the energy of the fluoresced photon is also unique to each element. These energies are tabulated in [50]. The fluoresced photons are what is of interest in the measurement. Since an atom cannot fluoresce if it has not lost a core electron, the intensity of fluoresced photons should be proportional to the intensity of the absorbed photons. Thus we can write

$$\mu_f(E)x \propto \left(\frac{I_f}{I_0}\right), \tag{5.3}$$

where the subscripted f refers to a fluorescence measurement. The proportionality is due to the different ways in which the core hole can be filled, such as relaxations where secondary electrons are produced or where cascading of multiple electrons can occur. In addition to these relaxations, the incident X-rays could elastically scatter off of the sample, or be transmitted through. With the exception of transmitted photons, all of the other processes just described will contribute noise to the signal. Only the primary fluorescence is of interest, referred to as the $K\alpha_1$ emission line.

To reduce measurement noise, the elastically scattered X-rays are blocked from the detector by using a "$Z-1$" filter [51]. These filters work because they have an absorption edge below that of the scattered X-rays, but above the energy of the $K\alpha_1$ fluoresced X-rays of interest. Since the filter

is absorbing X-rays, it is also re-fluorescing more unwanted X-rays. Soller slits installed between the filter and the detector eliminate most of the unwanted X-rays by allowing only X-rays that originate from the sample to pass into the detector. The X-rays produced by low energy events, such as cascading electrons, can be mitigated by attenuating the signal using low-Z materials, such as aluminum foil, if necessary.

5.1.2   Typical Data

XAFS data typically consists of two regions, as shown in Fig 5.1. The region ~ 10 eV below the absorption edge to ~ 30 eV above the edge is referred to as the X-ray Absorption Near Edge Structure (XANES). The energy region from the top end of the XANES and higher is referred to as the Extended X-ray Absorption Fine Structure (EXAFS). The "white line" is the sharp feature seen at the onset of absorption. This feature can significantly vary in intensity and shape depending on the nature of the material being probed. There is no precise delineation as to where the boundary is between EXAFS and XANES. Different theoretical methods are employed to describe the fine details of the structure in each region. Each will be discussed in the remainder of this chapter, with a particular emphasis on the EXAFS region.

5.2   XANES Spectra

The XANES region yields information regarding the local environment of an atom. XANES is also sensitive to the electronic state of the absorbing atom. Quantitative analysis of XANES has progressed slower than EXAFS. One reason for this is that the path expansion method, discussed in section 5.6, breaks down close to the absorption edge and calculations must be done by direct matrix inversion, which can quickly become computationally intensive. The great strength of XANES is the relative ease with which it yields qualitative information about the atom of interest. Changes in the formal charge state of an absorbing atom will cause the absorption edge to shift by a few eV, an easily observable shift. High degrees of symmetry surrounding the absorbing atom can contribute to additional features immediately after the white line. Additional features in the edge region can
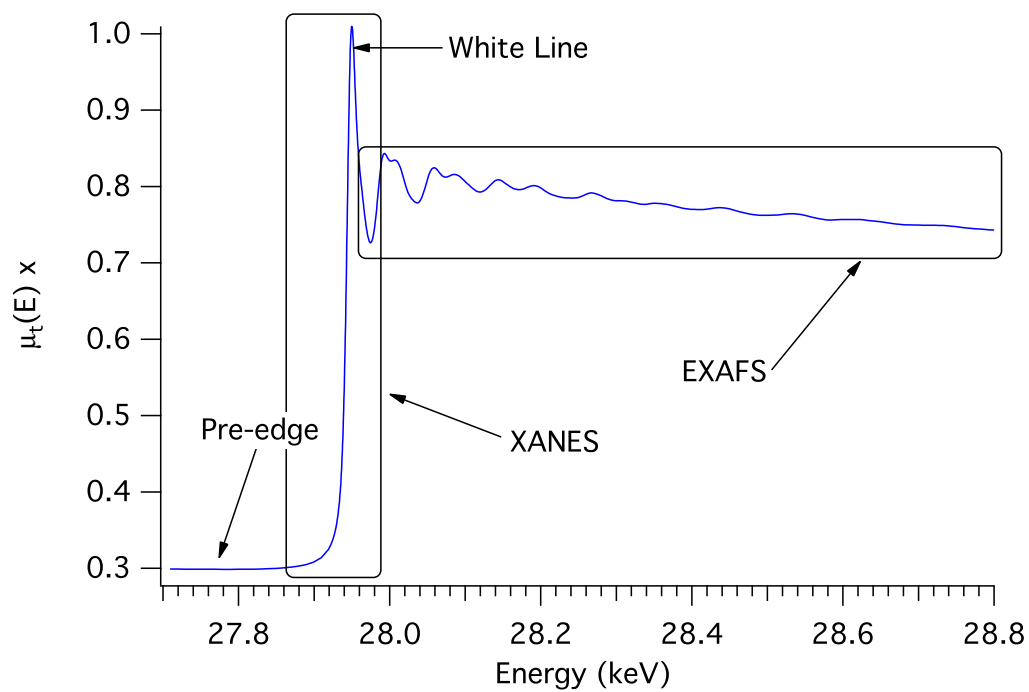
Figure 5.1: A typical graph of the raw XAFS data as gathered in transmission mode. The sample is In_2O_3 powder and represents three scans averaged together. There is not a set boundary between the XANES and EXAFS regions.

give clues to the electronic state of the absorbing atom as certain electronic transitions are allowed or forbidden.

If a sample is in an unknown local bonding environment, XANES measurements of a set of related of known structure can be measured. If the spectrum matches one of the standards, that standard best represents the local bonding environment of the sample. If the sample appears to be a mixture, linear combination fitting can be used to determine what phases are present and at what concentrations. Theoretical XANES can be calculated and used to model a certain feature in the spectra as being related to a particular arrangement of neighboring atoms. For a more in depth discussion of these topics, as well as the capabilities and methods of XANES analysis see [49, 52, 53].

5.3   EXAFS Spectra

In the absorption event described earlier, the photoelectron was ejected from the **central** or **absorbing atom**. After the photoelectron leaves the central atom, it propagates outward as a spherical wave of the form e^{ikr}/r, where k is the wavenumber of the photoelectron. The wavenumber is calculated with respect to the edge-energy (E_0) using

$$k = \sqrt{\frac{2m(E - E_0)}{\hbar^2}}, \tag{5.4}$$

where E is the energy of the incident X-ray, m is the mass of the electron and $\hbar$ is the reduced Planck constant.[1]   Strictly speaking E_0, as used in the data processing, is properly expressed as $E_0 + \Delta E_0$, where E_0 is a fixed energy chosen somewhere on the absorption edge and ΔE_0 is a small correction that is a variable in the fitting. The edge-energy, E_0, can be chosen somewhat arbitrarily during the background subtraction, as discussed in section 5.6.2. The correction term, ΔE_0, is a variable that is used to align the theoretical spectrum to the measured spectrum. For brevity, both terms are often collectively referred to as E_0.

After leaving the central atom, the photoelectron wave will scatter off of nearby atoms, referred to as **scattering atoms**. The outgoing and scattered photoelectron waves create interference

---

[1] The relation $E - E_0 \approx 3.81k^2$ is handy to remember.

effects. The interference depends strongly on the distance between the absorbing and scattering atoms and their atomic number (Z), as well as the kinetic energy of the outgoing photoelectron ($KE = E - E_0$). It is these interference effects that cause the oscillations in the EXAFS region of Fig. 5.1. These oscillations are what is studied in EXAFS analysis.

If several atoms are at the same distance from the absorbing atom, they will contribute the same component to the EXAFS signal. This group is referred to as a **shell** of atoms. The degeneracy of a shell refers to the number of atoms in it. Often, the degeneracy is simply referred to as the coordination number. Each shell of atoms will contribute a sinusoidal wave to the EXAFS spectrum. The combination of all the sinusoidal waves from all the scattering atoms makes the final EXAFS spectrum.

If the photoelectron only scatters off of one neighbor before returning, it follows a single-scattering (SS) path. If the photoelectron scatters off of multiple neighbors it is a multiple-scattering (MS) path. The degeneracy of a SS path is equivalent to the coordination number of that shell, and the degeneracy of a MS path is the number of unique ways that particular path can occur. A graphical representation of these ideas is shown in Fig. 5.2. When EXAFS spectra are calculated this way it is referred to as the **path expansion method**.

When discussing different scattering shells, one of two descriptions is used. Sometimes a shell is simply referred to a nearest neighbor or next-nearest neighbor shell, as in Fig. 5.2. If the type of the atom is important, the shells are referred to by the absorbing and scattering atoms, for example, the In-Zn shell refers a shell where In is the absorbing atom and Zn is the scattering atom. The Zn-In shell would refer to a shell where Zn is the absorbing atom and In is the scattering atom.

5.4   Background Subtraction

The EXAFS region, shown in Fig. 5.1, can be separated into two components. The first is the slowly varying atomic background, $\mu_0(E)$. The second is the rapidly varying EXAFS portion: this is the region of interest. At the beginning of the chapter, the discussion of absorption proba-
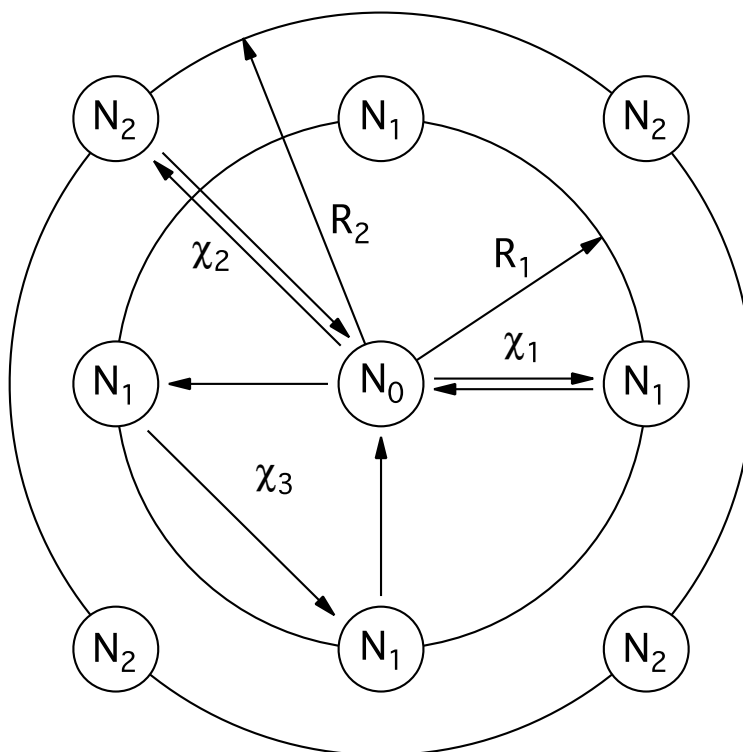
Figure 5.2: A diagram representing several scattering paths and coordination shells. N_0 is the absorbing atom. The scattering path to a nearest neighbor, N_1, is represented by the path χ_1. It is a SS path with a degeneracy of 4, which is equivalent to the number of nearest neighbors. These 4 atoms make up a **coordination shell** at a distance R_1 from the absorber. A similar argument applies to the coordination shell at a distance R_2 from the absorbing atom. The degeneracy of path χ_2 is equivalent to the coordination number of next-nearest neighbors, again 4. The MS path χ_3 is also shown. It is a triangular path with a degeneracy of 8 and path distance, R_3, equal to half of the sum of the three segments that make up its path. MS paths are weaker than SS paths, but there can often be a lot of them contributing to the signal, especially in very ordered systems. Figure adapted from [49].

bility assumed the atom was isolated. The atomic background takes into account changes in the absorption probability of the atom in the presence of its atomic neighbors. Thus the absorption can be written as

$$\mu(E) = \mu_0(E)\left(1 + \chi(E)\right),\qquad(5.5)$$

where $\chi(E)$ is the scattering contribution from the photoelectron of interest. Many other experimental effects that do not contribute to the EXAFS are also included in the $\mu_0(E)$ term. These include such effects as detector energy dependence, harmonic content of the X-ray beam, etc. These terms often show a low frequency oscillatory structure that, if not accounted for, will corrupt the EXAFS signal. These artifacts are minimized with good experimental procedures. *Ab-initio* calculations of $\mu_0(E)$ are difficult because of the contribution of experimental effects, therefore, it is often determined empirically. Removing this term from the data is the process of **background subtraction**.

In addition to background subtraction, XAFS data is often presented after **pre-edge removal** and **normalization**. Pre-edge removal fits a line to this region of the data, and subtracts it from the entire data range. This serves to make the entire pre-edge region zero, fitting in line with the simple model of no absorption below the edge. A line, called the post-edge line, is then regressed through the high-energy EXAFS portion of the data, where any oscillations are negligible. The difference between the pre- and post-edge lines at E_0 is referred to as the edge-step, δ_μ. The post-edge line is subtracted from the data, and the EXAFS region is normalized to the edge-step. Normalizing to the edge-step means that the EXAFS data will oscillate around one, simulating the absorption probability of one photon. This is the typical way that $\mu(E)$ results are presented.

A rearrangement of Eq. 5.5 and normalization to the edge-step, yields the scattering due to the photoelectron

$$\chi(E) = \frac{\mu(E) - \mu_0(E)}{\delta_\mu}.\qquad(5.6)$$

Finally, $\chi(E)$ is converted to $\chi(k)$ using Eq. 5.4. The $\chi(k)$ data, seen in Fig. 5.3(a), is referred to as "The EXAFS." Because the EXAFS signal is so strongly attenuated as a function of k, it

is common to weight the spectrum with a factor of k^n, typically $n = 2$ or 3. This has the effect of amplifying the oscillations as seen in Fig. 5.3(b). This weighting counteracts the attenuation due to the fundamental nature of the measurement (discussed in section 5.6), amplifying the data for the atoms beyond the first coordination shell. Different weightings can also yield information about the atomic species of near-neighors [49].

Technical Details of $\mu_0(E)$ To obtain a functional form of $\mu_0(E)$, a cubic b-spline is regressed through the EXAFS portion of the data using the AUTOBK algorithm [54]. The number of nodes in the spline is $2R_{bkg}\Delta k/\pi$, which are evenly spaced in k-space over a range of Δk. R_{bkg} is a parameter that determines the lowest frequency component allowed in k-space, or equivalently, the highest frequency component in R-space. This isolates the low-frequency spectrum in $\chi(k)$ which is due to $\mu_0(E)$, allowing this contribution to be removed from the data. A typical value for R_{bkg} is about half of the nearest-neighbor bond distance [49, 55]. This number can be varied, but if too many nodes are used the spline could fit itself to the EXAFS portion of the data and remove important oscillations. If too few nodes are used peaks could appear at very low-R values, leading to incorrect interpretation of the data.

5.5   Fourier Transform - $\chi(R^*)$

The $\chi(k)$ spectrum measured by an EXAFS experiment is a sum of sine waves resulting from the scattering of a photoelectron off of atoms at various distances from the central atom. If we Fourier transform such a spectrum, the different frequency components in k-space will be separated as peaks in R^*-space. The Fourier transformed data is written as either $\text{FT}[\chi(k)k^n]$, or as $\chi(R^*)$, with units of Å^{-1-n}. In the presentation of EXAFS results, it is common to plot the data as the magnitude of the Fourier transform, $|\chi(R^*)|$. This data makes it easier to ascertain a qualitative feel for what the structure is around the central atom. However, since the Fourier transform is a complex function, it is important to look at the real and imaginary portions of the spectrum as well. This is because the phase relationship between different scattering paths is lost when looking the at magnitude of the transform.
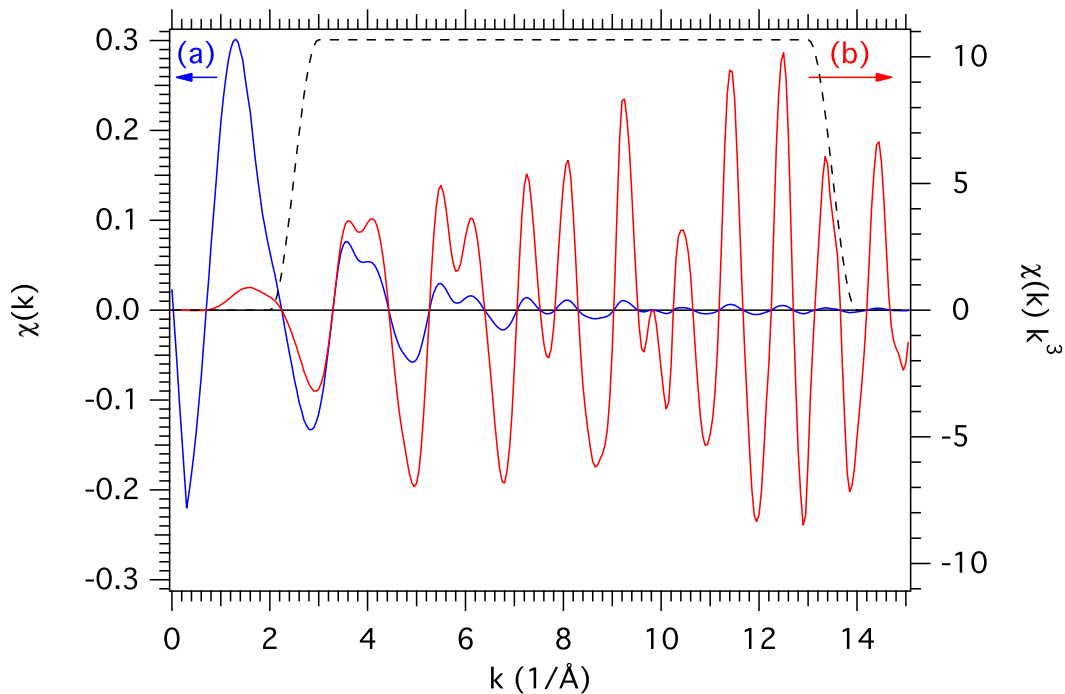
Figure 5.3: (a, blue) The EXAFS extracted from absorption spectrum of the In_2O_3 sample shown in Fig. 5.1. Even for a crystalline material, the EXAFS is strongly attenuated as a function of k. In general, EXAFS analysis does not use the data below ~ 2 Å^{-1} because the path expansion model of EXAFS breaks down near the absorption edge. (b, red) The k^3 weighted $\chi(k)$ of the same spectrum. The dashed black line is the Fourier transform window with a range of $2.5 - 13.5$ Å^{-1}. The window is a Hanning window with 0.5 Å^{-1} sills that help mitigate Fourier transform ringing.

Since the spectrum being Fourier transformed has a finite range, the resultant peaks in R^*-space are broadened. Ripples from the termination of the transform also appear. Using windows that slowly decrease the intensity of the signal to zero, rather than having a sharp end point, minimizes these ripples. A Hanning Fourier transform window is shown as a black dashed line in Fig. 5.3.

The magnitude and the real part of the Fourier transform can be seen in Fig. 5.4. It is tempting to attempt to interpret the magnitude of $\chi(R^*)$ as a radial distribution function (RDF). However, the magnitude of $\chi(R^*)$ *is not* a RDF. First, the radial position of the peak in $|\chi(R^*)|$ does not correspond to the actual distance between the atoms. It is modulated because of the phase shifts associated with both the absorbing and scattering atom, as will be discussed in section 5.6.1. Typically a peak in $|\chi(R^*)|$ appears a few tenths of an angstrom below its actual distance. Second, the complex nature of the Fourier transform means that two paths may be partially out of phase with each other. This could result in a minimum in $|\chi(R^*)|$ instead of a peak, or a peak where there should a minimum. Third, multiple scattering paths can produce sizable signals in $|\chi(R^*)|$, particularly for highly ordered systems. Lastly and in contrast, the peak height in a RDF depends only on the coordination number, N. In $|\chi(R^*)|$ signals, the peak height depends strongly on several variables, including the coordination number.

5.5.1   An Important Note on EXAFS Nomenclature

As was just discussed, when looking at a plot of $\chi(R^*)$ the distance between neighboring shells *can not* be read directly from the graph. The source of this discrepancy will be discussed in the following section. Despite this discrepancy in the displayed data, when reporting the results of a fit, the numbers presented are the actual interatomic distances. The context of a statement should be make clear if a feature in the spectrum is being referred to using the shifted values or the actual values.

In an effort to minimize confusion, when a feature on a $\chi(R^*)$ plot is discussed an asterisk will be used. When discussing the actual interatomic distances the asterisk will be omitted. For
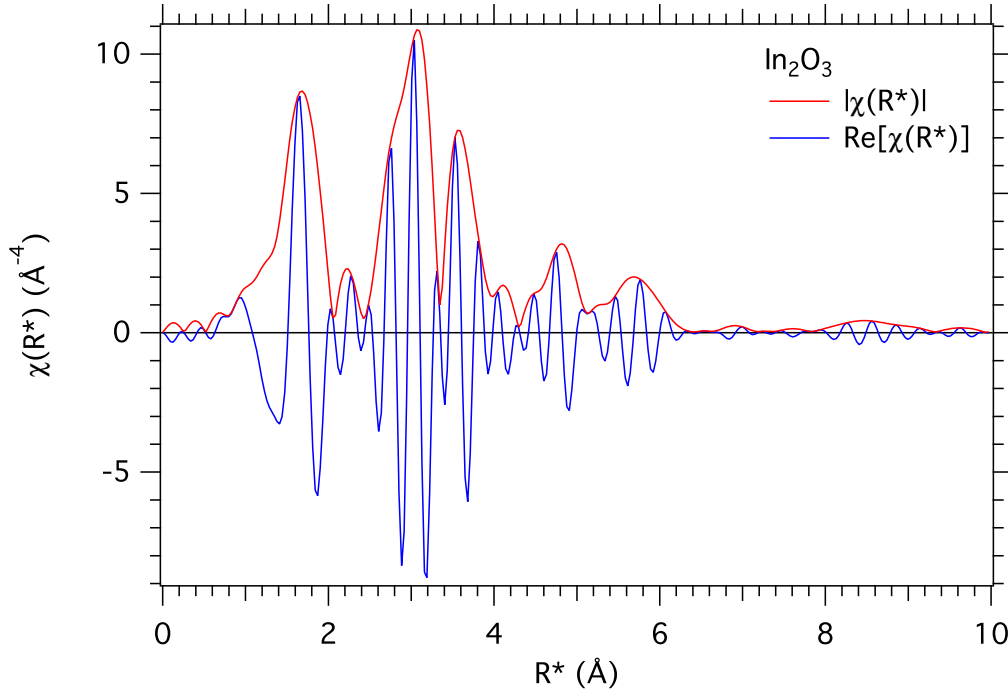
Figure 5.4: The Fourier transformed spectrum of Fig. 5.3. The red line represents the magnitude of the Fourier transform and the blue line is the real portion. Even for a crystalline structure such as In_2O_3, the structural information in EXAFS is strongly attenuated by 6 Å.

example, Fig. 5.4 has a peak at $R^* = 1.7$ Å, corresponding to In-O bond distance of $R_O = 2.18$ Å, where the subscript represents the scattering atom for the particular path.

5.6   The EXAFS Equation - $\chi(k)$

Rather than going through a rigorous derivation of the current XAFS theory, the interested reader should refer to the wealth of resources with rigorous derivations of the EXAFS equation [47, 48, 53, 56–59]. A heuristic derivation of the EXAFS equation is presented in Appendix B.1. The EXAFS equation is interpreted as a sum of all possible scattering paths, i, from a particular absorbing atom:

$$\chi(k) = \sum_i \chi_i(k), \tag{5.7}$$

where each path is written as

$$\chi_i(k) \approx \frac{N_i S_0^2}{k R_i^2} F_i^{eff}(k) \sin\left[2kR_i + \phi_i^{eff}(k) - \frac{4}{3}k^3 C_3\right] e^{-2\sigma_i^2 k^2} e^{-2R_i/\lambda(k)}. \tag{5.8}$$

This expression is the path expansion method and its form can be used for SS paths as well as MS paths. As written it applies to SS paths, but by replacing $F_i^{eff}(k)$ with a matrix an equivalent expression can be used for MS path [56, 60].

Different references write Eq. 5.8 in different ways, depending on what is being emphasized. However, the information they contain remains the same. All of the parameters can be categorized into two main groups based on their influence, those that primarily effect the **phase** of the spectra and those that primarily effect the **amplitude**. However, it is important to remember that because $\chi(R^*)$ spectra are complex, changes in a phase term of one path may affect the amplitude of another. Each of these parameters will be detailed term by term, and a brief explanation will be given of each and how it affects the spectrum. The theoretically calculated parameters will be explained first, followed by a discussion of the refined parameters.

5.6.1   Theoretical EXAFS Parameters

These parameters in the EXAFS equation are not typically fit or measured, but rather calculated using *ab-initio* multiple scattering theory. The parameters were calculated using the program FEFF [61].

$F_i^{eff}(k)$ **- Effective Scattering Amplitude.**   When considering only scattering from a single near neighbor, this term is identical to the atomic scattering factors used in traditional XRD. This term helps account for the elemental selectivity of EXAFS, because elements with more electrons tend to be stronger scatterers at higher k. It also explains why elements of similar atomic number (Z) such as O and N, are difficult to distinguish with EXAFS. Multiple scattering paths are treated equally well within FEFF because rather than only considering the distance to a scattering atom, the geometry to the atom is considered as well. The **effective** portion of the term refers to the fact that the backscattering amplitude as presented in [46] used a plane wave approximation, where the authors of FEFF developed an exact, curved wave expression for the backscattering amplitude [62, 63].

$\phi_i^{eff}(k)$ **- Effective Phase Shift.** This accounts for the phase shift of the photoelectron due to interactions with the absorbing and scattering atom. This is primarily due to the potential valleys created by the atoms causing the photoelectron to travel at different speeds depending on the proximity to an atom. As k is increased the effect of this phase shift falls off, causing the oscillations in $\chi(k)$ to come later than would be expected. This has the same effect as decreasing R_i, thus the peaks in $\chi(R^*)$ are shifted slightly in the negative direction.

$\lambda(k)$ **- Mean Free Path.** The finite lifetime of the core hole and photoelectron, which are extrinsic losses, are accounted for with the mean free path. It is an intrinsic loss because it occurs after the creation of the photoelectron. This parameter is a generally increasing function of k. This trend, coupled with the exponential dependence in $e^{-2R_i/\lambda(k)}$, is one of the reasons that only atoms closer than ~ 10 Å will ever contribute to the EXAFS [49], the other reason being the $1/R_i^2$ term in the EXAFS equation. The mean free path affects the amplitude in $\chi(k)$, with the largest changes occurring in the low-k portion of the spectrum.

5.6.2 Refined EXAFS Parameters

This section covers the parameters of the EXAFS equation that are refined during a fit. These parameters are fit using the HORAE software package [64]. This package consists of two main parts, ATHENA, used for background subtraction, and ARTEMIS, used for fitting the data. This software is a graphical front-end to IFEFFIT [65] which is a command line based program containing algorithms for the background subtraction and fitting of XAFS data to theoretical FEFF calculations.

N_i **- Degeneracy.** The degeneracy is the number of equivalent ways that a particular scattering path can be formed. For SS paths this number is referred to as the coordination number. It is directly proportional to the amplitude of $\chi(k)$ and $\chi(R^*)$ spectrums and has no k dependence.

S_0^2 **- Passive Electron Reduction Factor.** After the photoelectron is ejected, the remaining *passive* electrons relax slightly in the absence of a core electron. This relaxation causes an imperfect overlap of the initial and final quantum states, resulting in a reduction in the amplitude. It also accounts for any other processes that rob the photoelectron of energy during its creation.

Measurement and data processing issues, such as detector non-linearity, harmonics or incorrect background subtraction can affect this parameter as well. In other words, intrinsic losses, or those losses associated with creation of the core hole, are folded into this term.

It is generally accepted that this term is not dependent (or weakly so) on k and R^*, as such it affects only the amplitude of the spectra [66, 67]. The accepted values for this term fall in the range of 0.7-1.05 [68]. S_0^2 is different for different absorbing elements, but generally is considered transferable between material systems with the same absorbing atom at the same edge [49].

Since S_0^2 and N_i affect the data in exactly the same way, if both of these terms are refined in a fit, they will be completely correlated with each other. To solve this, a typical XAFS experiment measures a well-understood standard, such as a pure oxide powder, when trying to understand an unknown oxide with the same absorbing element. The standard is fit using a fixed N_i while letting the S_0^2 value float. Once a value for S_0^2 is obtained from a standard, the same value can used for a similar unknown system.

R_i **- Half Path Length.** For an absorption event to contribute to the EXAFS, a photo-electron must travel from the absorbing atom, scatter off of one or more nearby atoms, and return to the absorbing atom. For SS paths this term represents the distance from the absorbing atom to the scattering atom. When physically sensible, this parameter is the same as the average bond distance; otherwise it is simply referred to as the path length. The $1/R_i^2$ term in Eq. 5.8 is one of the reasons why the EXAFS signal is significantly attenuated in k-space, as in Fig. 5.3. This attenuation limits the sensitivity of EXAFS to local structure. An increase in R_i will cause the oscillations in $\chi(k)$ to have slightly smaller spacing, modulating the phase of the spectrum. The effect is most pronounced at higher k. The shift in R^* is approximately equal to the relative change in the parameter.

σ_i^2 **- Mean Square Radial Disorder.** The Mean Square Radial Disorder (MSRD), accounts for any disorder in a given shell. The disorder could be due to thermal or static disorder in the path. This is another term that affects the amplitude of the EXAFS, but since it enters into the path as $e^{-k^2\sigma_i^2}$, its effect becomes much more pronounced at high-k. An increase in this term

will cause a pronounced decrease in the $|\chi(R^*)|$ peak amplitude, but only a slight increase in the FWHM of the peak. This is because most of the width of the peaks in EXAFS is due to the finite k-range of the Fourier transform.

Sometimes this term is referred to as the EXAFS Debye-Waller factor because the term bears some similarity to the Debye-Waller factor (DWF) encountered in typical X-ray diffraction analysis. However, this nomenclature is becoming less popular because there are some important differences between the two terms. In XRD, the DWF refers to average variation from the lattice point. In EXAFS, the MSRD refers only to the variation in the average distance between the atoms. Depending on how the atoms are moving, situations may arise where the DWF is less than the MSRD or vice-versa.

E_0 **- Edge Energy.** Although this term is not explicitly present in Eq. 5.8, it is used in the calculation of k via Eq. 5.4. Assigning a explicit physical meaning to this term is difficult. However, differences in this term can be very meaningful. For example, oxides often show increases of several eV in their absorption edge, when compared to the pure element. Shifts of a few eV can also distinguish between different oxidation states. This term affects the phase of the spectra, causing a shift most prominent at low-k. This is the opposite of R_i, where the primary effect was at high-k. The shift in $|\chi(R^*)|$ is similar to that seen by shift in R_i. A reasonable first guess for this parameter is the peak of the first derivative of $\mu(E)$.

5.6.2.1   Third Cumulant - C_3

The EXAFS equation as presented contains the assumption that the distribution of bond lengths (the MSRD) in a given shell is Gaussian. Using the **cumulant expansion** method, the variation in the bond lengths is represented as $C_2 = \sigma_i^2 \equiv \langle (R_i - \bar{R}_i)^2 \rangle$, where C_2 is called the second cumulant. For a further description of this method, please see Appendix B.2. In this expression σ^2 and R_i are identical to their definition in the previous section, and $\bar{R}_i$ is the average bond distance of the particular path in question.

If the bond variation is not Gaussian, the third cumulant, C_3, can be used. It is defined as

as $C_3 = \langle (R_i - \bar{R}_i)^3 \rangle$. This term creates a skew in the $\chi(R^*)$ peak. During a fit, it is strongly correlated with R_i which leads to an increased degree of uncertainty in the refined values for R_i. The uncertainty added to the absolute value of the refined path length is not well represented by the reported error bars, however trends in this parameter are still reliable [69]. Typical values for this parameter are $\sim 10^{-4}$ Å^3. For example, in a system where lots of disorder is expected, such as liquid gallium, $C_3 \approx 8 \times 10^{-4}$ [70]. In a system where little disorder is expected, such as amorphous silicon, $C_3 \approx 1 \times 10^{-4}$ [71]. Although this is a somewhat uncommon fitting parameter, it is often used in amorphous systems, where assuming a Gaussian distribution of bond lengths may not be valid. This study will utilize this parameter in the refinement of the nearest-neighbor bond length.

5.7   Statistical Tools

In the fitting of EXAFS data, criteria must be established whereby one can determine whether a particular fit or model is "good" in comparison to another. The IFEFFIT routine fits a given model to the data using a least-squares fitting method, using the parameters discussed in section 5.6. To quantify the accuracy of the results, two statistical figures of merit of produced, the R-factor ($\mathcal{R}$), and the reduced chi-squared (χ_ν^2).

5.7.1   Chi-Squared - χ^2

The parameter that is minimized during the least squares minimization is chi-squared, χ^2 [72]. This term should not to be confused with our EXAFS data, $\chi(k)$ and $\chi(R^*)$. χ^2 is evaluated on both the theoretical spectrum, calculated from FEFF, and the experimental data. It is defined as

$$\chi^2 = \frac{N_{idp}}{N} \sum_n^N \left| \frac{\chi_{data}(R_n^*) - \chi_{fit}(R_n^*)}{\epsilon_n} \right|^2, \tag{5.9}$$

where N_{idp} is the number of independent data points, N is the number of the points in the real and imaginary portion of the Fourier transform, ϵ_i is the measurement uncertainty at each data point and the sum is over each data point, n. Because this quantity must be evaluated for each data point, it is important to use uniform grids in k- and R^*-space, so that fast Fourier transform

methods can be used.

5.7.1.1   Independent Data Points - N_{idp}

The number of independent data points is a measure of the information content within a set of EXAFS data. Information theory dictates that this can be calculated using the Nyquist theorem,

$$N_{idp} = \frac{2\Delta k \Delta R^*}{\pi} + 1, \tag{5.10}$$

where Δk and ΔR^* represent the range over which the data is fit in k- and R^*-space, respectively [73]. For EXAFS, it has been suggested by some that the additive term should be 2, not 1 [74]. The difference is not particularly important because this value is regarded as an upper limit to the information content in a spectrum. One reason for this is that the Nyquist theorem assumes that the information is ideally packed throughout the entire spectrum. In a $|\chi(R^*)|$ spectrum, the signal in the low-R^* region is likely to be dominated by one, or perhaps two shells of atoms, while a higher-R^* region could have contributions from many next-nearest neighbors (a metal) or almost no signal at all (a liquid). The theorem also assumes that the error of the measurement is dominated by statistical, not systematic, error. At modern synchrotron sources, very high X-ray fluxes ensure that for many EXAFS experiments statistical errors are not a primary concern. However, systematic errors, such as monochromator glitches or non-ideal samples, can be problematic.

5.7.1.2   Measurement Uncertainty - ϵ_n

The measurement uncertainty at each data point, ϵ_n, is a parameter that can not be easily measured or developed *ab-initio*. In practice, this parameter can only be estimated because both Poisson noise and systematic errors are present in a given measurement. It is estimated by measuring the mean of the signal between $R^* = 15$ and 25 Å. This range should be large enough such that there is no contribution from the structure of the system in question. However, the general assumption is that this method produces an ϵ about an order of magnitude too low [55]. This results in a significant underestimation of the error bars for a particular fit.

5.7.2 Reduced Chi-Squared - χ_ν^2

To aid in answering the question of whether one model is better than another, the **reduced chi-squared** is defined as

$$\chi_\nu^2 \;\equiv\; \frac{\chi^2}{\nu} \tag{5.11}$$

$$\nu \;\equiv\; N_{idp} - N_{var}, \tag{5.12}$$

where ν is called the **degrees of freedom** in a fit and N_{var} is the number of variables fit. This parameter allows comparison between various models or constraint schemes on a particular set of data. A criterion for determining if a change in the model is statistically significant is if the χ_ν^2's between two models differ by more than a factor of $1 + 2\sqrt{2/\nu}$, the change can be considered significant. If too many variables are used, the fit can become over-determined, resulting in a perfect fit to the data. The χ_ν^2 would accurately reflect that this fit does not have statistical significance, even though by eye the fit looks excellent. A perfect fit to the data should never be achieved because the theoretical construction of EXAFS, while having greatly advanced in the past 30 years, is still an approximation.

The fitting algorithm produces a covariance matrix from which the fitted parameters and their error bars can be extracted. As discussed earlier, these error bars represent a significant underrepresentation of the actual error. Ideally, a good fit should produce a χ_ν^2 of unity. In practice however, χ_ν^2 is often much greater than 1. To account for the large χ_ν^2 and the small ϵ, the diagonal elements of the matrix are multiplied by a factor of $\sqrt{\chi_\nu^2}$, increasing the uncertainties by the same amount and rescaling χ_ν^2 to be equal to 1. The disadvantage to scaling the error bars this way is that in doing so an assumption is being made that every fit is indeed a good fit. However, this disadvantage is more than outweighed by the fact that the error bars are now a much better estimate of the actual error. It also means that it is important for the experimenter to carefully look at the fit results and decide if the values and their error bars make physical sense.

5.7.3 R factor - $\mathcal{R}$

The $\mathcal{R}$-factor is the fractional misfit of the data compared to the fit, and is defined as

$$\mathcal{R} = \frac{\sum_n \left(\chi_{data}(R_n^*) - \chi_{fit}(R_n^*)\right)^2}{\sum_n (\chi_{data}(R_n^*))^2}, \tag{5.13}$$

where n indicates the sum is over each data point. This term is proportional to χ^2, but avoids the issue of poor estimation of ϵ_i. Values less than 0.05 are generally considered to reflect a reasonable fit to the data [49].

In practice physical intuition, the $\mathcal{R}$-factor, and χ_ν^2 are all used in the process of making a determination of the fit quality. In some situations one term may provide more insight than another. For example on a single data set comparing two different models, the χ_ν^2 can play a significant role, but a fit may be obtained where the χ_ν^2 shows a statistical improvement but no longer makes physical sense, such as a negative MSRD (σ^2). In this case the model with a higher χ_ν^2 is the better model. It is necessary to take care when comparing χ_ν^2 for fits using a different k-range or k-weighting because changing these parameters can lead to large changes in χ_ν^2 that are not indicative of a drastic change in fit quality.

5.7.4 Multiple Data Set Fitting

Because the number of independent data points in EXAFS is often a limiting factor in creating a good model, it is desirable to fit similar data sets simultaneously. For example, when measuring the same sample at different temperatures, the coordination numbers could be constrained to be equal for all data sets. Constraining certain parameters to have the same value across the data sets reduces the number of variables. This means that the number of independent data points is doubled because two separate data sets are used, but the number of variables increases by a factor less than 2. This serves to decrease correlations between variables thereby increasing the reliability and decreasing the error bars of the resultant fit.

For this work, the conducting and intrinsic samples of a given (nominal) composition were fit simultaneously. The EXAFS spectra of the conducting and insulating samples of a given composi-

tion always came out nearly identical to each other, making the two data sets natural candidates for multiple data set fitting. To determine what parameters should be constrained across data sets, a figure-of-merit, $\mathcal{F}$, was created that would allow quantitative comparisons. For a given parameter and error bar, $x_i \pm \Delta x_i$,

$$\mathcal{F} = \frac{|x_C - x_I|}{\text{MAX}\left(\Delta x_C, \Delta x_I\right)}, \tag{5.14}$$

where the subscripts indicate the conducting and intrinsic samples. The larger of the two error bars is used to create a more conservative estimate in the error. However, the error bars were typically very close to each other. Thus, $\mathcal{F}$ represents the fractional difference of the parameters compared to the size of the error bars. A value of 1 indicates that the fit values are separated by one error bar, and a value greater than 2 indicates there is no overlap in the error bars.

5.8   Concluding Remarks

In this chapter, a basic overview of the fundamentals of XAFS has been given. This included the basic physical principles of what is being measured and how to interpret the results. XAFS relies on the unique response of individual elements to X-rays of varying energies and it provides information on the local arrangement of atoms surrounding a particular element. Information has been presented on how multiple data sets can be fit simultaneously, increasing the overall certainty of a fit.

Chapter 6

XAFS Experiments

6.1   Experimental Configuration

X-ray absorption measurements were carried out at the Stanford Synchrotron Radiation Laboratory (SSRL) at beamline (BL) 4-1, which uses a 20-pole, 2.0 tesla wiggler. No collimating mirror was installed in order to reach the In-edge. The monochromator used a double-bounce configuration with a $\langle 220 \rangle$ oriented Si crystal, with $\phi = 0°$. The monochromator was calibrated to the Zn k-edge (9659 eV) and the In k-edge (27940 eV) using the absorption edge of Zn and In metal foils. The monochromator was tuned by adjusting the bend on the crystals until the maximum intensity was reached. The monochromator was then detuned by $\sim$25% to eliminate harmonics.

Once inside the experimental station, the beam of X-rays passed through the I_0 slits. The vertical slits determine the angular acceptance from the monochromator, i.e. the energy resolution, because of the geometry of the monochromator. This is because Bragg's Law dictates that the energy spread using this geometry will be in the vertical direction. If the energy is increased while keeping angular acceptance the same, a bigger spread in energies will be present. After passing through the I_0 slits, the X-rays go through the I_0 ionization chamber and into the sample chamber with the sample at 45° relative to the incident beam. A schematic of this experimental configuration can be seen in Fig. 6.1.

A 6 cm Lytle detector was used to collect the sample fluorescence data. A Lytle detector is an ionization chamber with a large solid angle used to detect fluorescent X-rays. For Zn-edge measurements the gain of the detector was 10^9, which is the base setting. The measurements at
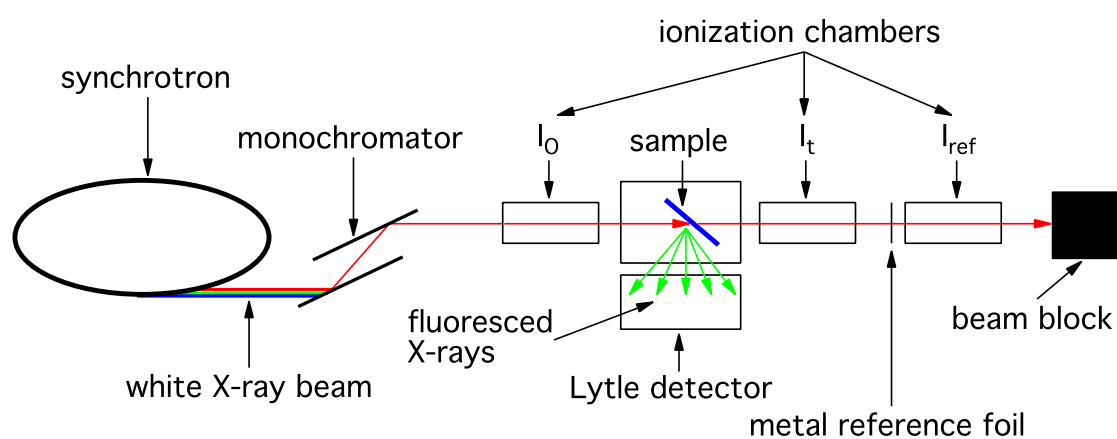
Figure 6.1: A schematic of a typical XAFS experiment. The entrance and exit slits of the ionization chambers are sealed with Kapton tape and filled with Ar gas. A $Z - 1$ filter and Soller slits (not shown) to decrease the background signal are in between the sample and Lytle detector. Additional optics (mirrors, slits, etc.) are not shown.

the In-edge used a gain of 10^{10}. Both edges used Ar as the ionization gas. The simultaneously collected transmission data was too distorted by the thick substrates for use in analysis, however a metal reference foil was left between I_t and I_{ref}. This allowed the scans to be realigned if the monochromator energy alignment drifted. At the In edge, this was observed on some scans with a drift ~ 1 eV or less. The Zn edge showed no signs of drift.

Measurements were also attempted using an energy discriminating 13-element germanium detector. The energy spectrum was very "clean," because the absorbing elements in the samples are relatively concentrated. This means that signals at energies other than the fluorescent energy were very small. Solid-state detectors are count-rate limited and must be dead-time corrected. In order to avoid over-saturating the Ge-detector, the slits, and thus the signal, had to be reduced in size by $\sim 80\%$. The slight increase in noise from the loss of energy discrimination was more than compensated by the huge increase in signal using the Lytle detector.

6.2   Sample Configuration

Due to the several regions of interest in XAFS measurements, scan routines were created that also had several regions of interest. Table 6.1 summarizes the scan parameters used for a single data sweep. The time per point is 1 second when stepping in energy. When stepping in k, the beginning of the range is 1 s/point, but the time increases cubically to 30 s/point by the end of the scan. This helps compensate for the rapidly decreasing signal in the EXAFS region.

Table 6.1: Scan parameters for the Zn-edge (9659 eV) measurements. The scan was divided into three regions, focusing on the three regions shown in Fig. 5.1.

region	units	start	end	step size
pre-edge	eV	9430	9640	10.0
XANES	eV	9640	9690	0.35
EXAFS	1/Å	1.62	12.0	0.05

Zn-edge   The vertical slits were each set at 1.0 mm, for a total opening of 2.0 mm. For each sample 5 data sweeps were averaged together, making each sample take ~ 3 hours to run. It was

determined that in order to overcome the signal-to-noise ratios beyond $k_{max} = 12$ would require an excessive number of scans to be run. To prevent elastically scattered X-rays from entering the detector, a Cu foil 3 absorption lengths thick[1] was placed in between the sample and the soller slits. This is a "Z-1" filter as discussed in section 5.1.1.2. The ionization chambers used N_2 as a fill gas. The vertical slit width was varied to maximize the number the X-rays entering the Lytle detector. However, care had to be taken because if the count rate multiplied by the count time exceeded 2^{24}, the electronics sending the data to the control computer would overflow causing a discontinuity in the data.

In-edge The vertical slits were each set at 0.5 mm, for a total opening of 1.0 mm. The slit sizes were decreased because at higher energies the geometry of the monochromator will allow a greater spread of energies to impinge on the sample. This energy spread was unacceptable when they were set to 1.0 mm. The proper slit size was determined by examining the XANES structure as the slit size was varied. Larger slits caused a dampening of the signal. In order to filter out any elastically scattered X-rays, an Ag foil that was 3 absorption lengths thick[2] was placed in between the sample and the soller slits as a "$Z - 1$" filter. The ionization chambers used Ar as a fill gas. It was necessary to increase the gain of Lytle detector to 10^{10} to account for the decreased ionization potential of the Ar at higher energies. The regions for the In-edge scans are shown in Table 6.2. Four sweeps were gathered for each sample, resulting in a measurement time of $\sim$2.5 hours/sample.

Table 6.2: Scan parameters for the In-edge (27940 eV) measurements. The scan was divided into three regions, focusing on the three regions shown in Fig. 5.1.

region	units	start	end	step size
pre-edge	eV	27710	27920	10.0
XANES	eV	27920	27970	0.35
EXAFS	1/Å	1.62	13.0	0.05

---

[1] This refers to the thickness at the Cu K-edge.
[2] This refers to the thickness at the Ag K-edge.

6.3   Experimental Considerations

6.3.1   Self-Absorption

For fluorescent measurements, an important experimental artifact to bear in mind is self-absorption. Simply put, self-absorption is when a sample is so thick and concentrated that when above the absorption edge, all the X-rays are absorbed. The only thing changing with energy is the effective thickness of the sample. In the extreme case, this will produce spectra with an edge-step, but no EXAFS content. The worst-case scenario for this effect is thick, concentrated samples. The definition of "thick" is in comparison to the absorption length of the material. One absorption length for our IZO films is $\sim 10~\mu$m at the Zn-edge and 4x that at the In-edge. The a-IZO films were about 500 nm thick, so self-absorption affects were not a major issue.

6.3.2   Calibration of S_0^2

To calibrate the values for S_0^2, powder oxide standards were used (ZnO or In_2O_3). The powder was finely ground and brushed onto a piece of Kapton (DuPont) tape. The tape was then folded over itself to contain the powder. The fluorescence data was fit using ideal crystal structures for the oxide being measured. In order to avoid significant self-absorption effects in the reference spectrum, the tape was only folded over itself once making the effective thickness small compared to the absorption length. This was confirmed by the small size of the edge step, δ_μ, as defined in section 5.4. Although theoretical corrections to self-absorption affects are available [55, 75], it is generally accepted that a better choice is to avoid these calculations if possible because they will introduce systematic errors into the data [49].

Chapter 7

In-Edge XAFS Results

7.1 In-edge XANES

The first method to determine what model may be appropriate for an unknown structure is to compare the XANES spectra with a known standard. As discussed in section 5.2, this is a qualitative method to compare local bonding environments. Figure 7.1 shows the normalized absorption spectrum for a representative IZO film (70/30-C) and crystalline In_2O_3 powder (c-In_2O_3). The similarity in these spectra means that the local bonding of the In atoms in IZO is very similar to that in c-In_2O_3, as would be expected.

7.2 In_2O_3 Ideal Structure

The theoretical model that was input into FEFF was based on the bixbyite structure (space group Ia$\bar{3}$) with a unit cell lattice constant of 10.117 Å [32]. This is the most stable phase for In_2O_3 under ambient conditions. The primitive cell has two unique In lattice positions and one O lattice position. The In positions are referred to as the b-site and d-site. The unit cell contains 32 cations and 48 anions. Of the cations, 8 reside on b-sites and the rest reside on d-sites, see the top panel of Fig. 7.2. The b-sites are surrounded by 6 O atoms with a bond length of 2.19 Å. The d-sites are surrounded by 2 O atoms each at bond lengths of 2.12, 2.19, and 2.21 Å. The combined average In-O distance is 2.18 Å. Both sites were attempted in fits of the In_2O_3 data, however regardless of which In site was used to fit the data no qualitative differences in the fit were observed. Therefore the simpler b-site was used in the model. This approach is consistent with findings in the literature
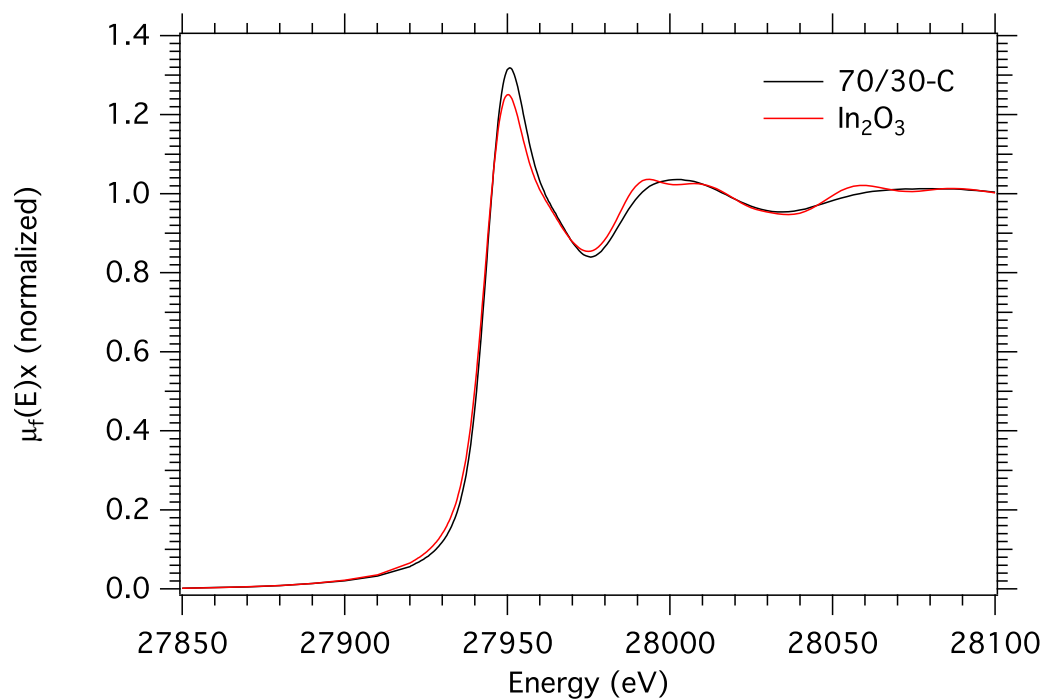
Figure 7.1: The normalized absorption spectra comparing the XANES region of a conductive 70/30 film (black) to c-In$_2$O$_3$ powder on tape (red) in fluorescence mode.

for similar systems [21, 76, 77]. Unless stated otherwise, throughout the remainder of this paper all structural references will be assuming the b-site model.

For In_2O_3, the In atoms are always octahedrally coordinated, however the In atom is too large to fit into an ideally packed O octahedron. This results in the octahedron becoming distorted. This distortion results in two different sets of O-O distances, as seen in the bottom panel of Fig. 7.2. The six shorter edges (2.83 Å) are all shared with a neighboring d-site octahedron, resulting in a 2nd shell In-In separation of 3.35 Å. The d-site exhibits a similar distortion, but has a range of O-O distances. From a charge shielding perspective, it makes sense that the edge-sharing octahedrons use the shortest edge possible. When the O atoms are farther apart the In atoms will tend to get closer together, but the In atoms naturally repel each other because of their +3 charge. Assuming hard spheres and ionic radii of 0.8 and 1.4 Å for In and O [78], respectively, the In-In distance can be calculated using simple geometry. This method predicts a 2nd shell In-In separation of 3.4 Å, which is close to the crystallographic value, justifying the accuracy of this method. Each O atom in a given central octahedron will be shared with two other edge-sharing octahedra. One corner sharing polyhedron, which creates the 3rd shell with an In-In separation of 3.82 Å, also shares each O atom in the central octahedron. This arrangement assures the charge neutrality of the polyhedron with each of the 6 O atoms having a charge of -2 shared between 4 polyhedra, for a net charge of -3 ($6 \times -2 \times 1/4$) which balances the +3 charge of the In ion. In c-In_2O_3, both of the In-In single scattering shells are easily observable with EXAFS, as seen in Fig. B.1.

7.3   In-edge EXAFS

7.3.1   IZO Model

The most prominent signal in IZO is the single scattering path of the 1st shell O atoms. The signal from atoms beyond the first shell is small, although it is well above the noise. This is a typical result from an ionic amorphous material. Figure 7.3 shows three spectra of varying compositions. It can be seen that there are only two regions showing significant differences. The first is the
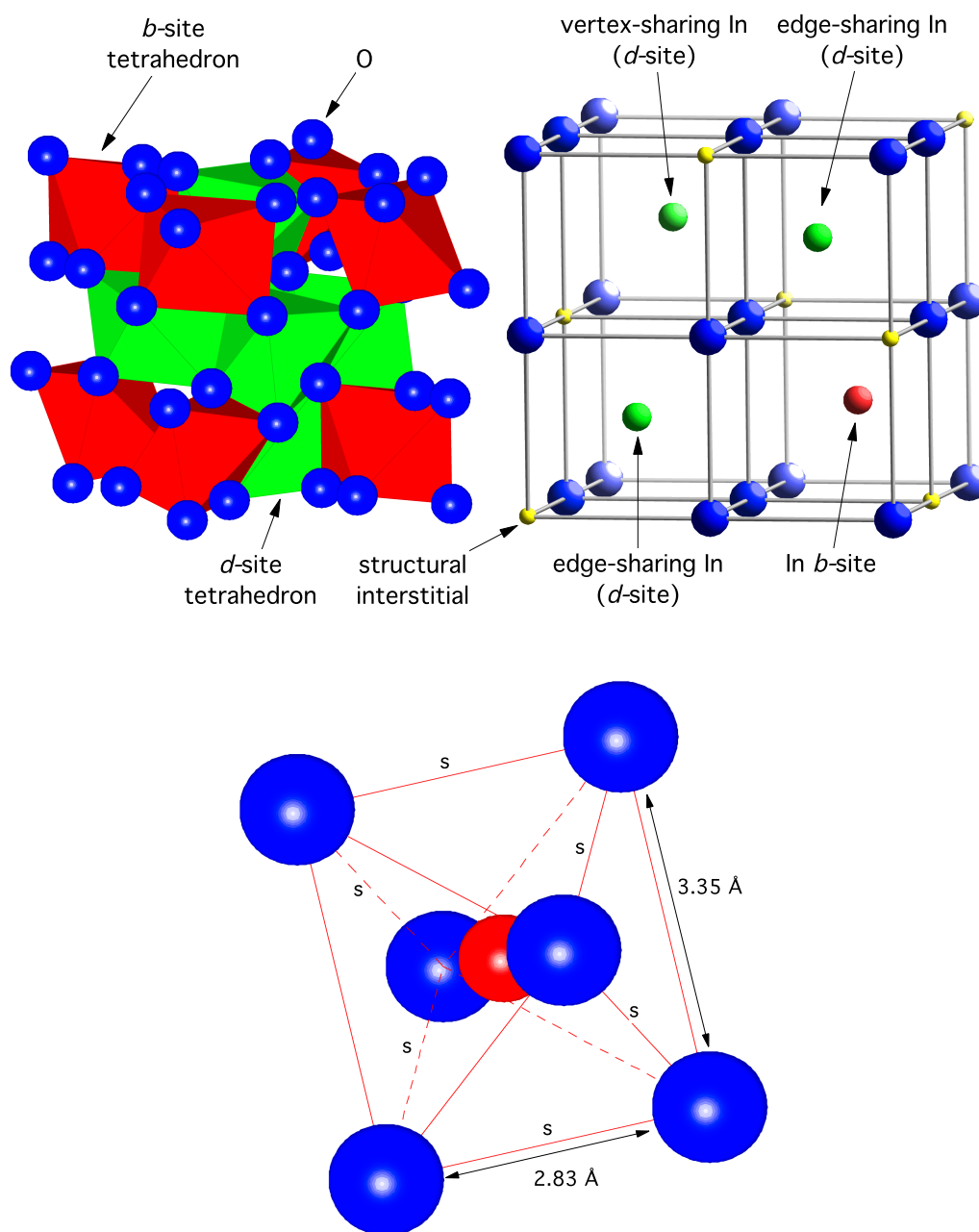
Figure 7.2: (top) The image on the left is a bixbyite unit cell. The image on the right is a simplified view of the view of the structure without the polyhedral distortions. The two edge sharing d-site atoms are in the foreground cages. The vertex sharing and b-site In atom are in the background cages. The structural interstitials are lattice positions missing an atom. (bottom) A detailed view of the b-site octahedron. The six sides marked with an "s" are the short edges with an O-O distance of 2.83 Å, the other 6 sides have an O-O separation of 3.35 Å. The shorter edges are all shared with neighboring octahedrons giving In-In separations of 3.35 Å. All 6 O atoms share a vertex with one other d-site octahedron.

amplitude of 57/43 sample at $R^* = 1.6$ Å. This difference is largely due to an experimental artifact where the spectra became slightly distorted, which will be discussed further in section 7.3.3. The other difference in the films occurs in the region near $R^* = 2.7$ Å. The increasing amplitude in this region is consistent with the trend of increasing Zn content. The signal just above 3 Å is consistent with the location of an In-In shell at 3.35 Å, as seen in the EXAFS of In_2O_3 powder (see Fig. B.1). Although a small shoulder is present in the In_2O_3 spectrum at 2.7 Å, this is primarily due to ripples from the main scattering peaks. When the σ^2 of this scattering path increases to the value necessary for the low signal seen in the IZO films, the shoulder from the ripple is dramatically reduced in amplitude. Thus, this peak appears to be from an actual scattering neighbor.

It is a reasonable assumption that because the region at 2.7 Å trends with Zn content, the peak is due to nearby Zn scattering atoms. Assuming the Zn is tetrahedrally coordinated (see section 8.1), it should have an ionic radius of 0.6 Å [78]. Replacing the In atom with a Zn in the hard sphere approximation (section 7.2), results in a theoretical In-Zn separation of $R = 3.1$ Å. To model this structure, a Zn atom was inserted into the model, replacing an existing edge sharing In atom. The vector coordinates to the new Zn atom were scaled such that it was 3.1 Å from the central atom. Since only whole atoms can be modeled, approximately the correct number of atoms were substituted, then ARTEMIS was used to scale the relative number of each atom type to match the composition of the sample.

Several methods were attempted to model the third shell of vertex sharing In atoms. None yielded physically meaningful results. If the k-range of these measurements could be extended further out to above 12 Å^{-1}, this task would probably have been more attainable. This is because heavy scattering neighbors, such as In, contribute the bulk of their signal at higher values of k. For example, if the k-range used for the IZO samples were applied to the In_2O_3 data, the third coordination shell disappears entirely. Although this is largely due to spectral broadening from a decreased k-range, it will make describing the region that much harder.
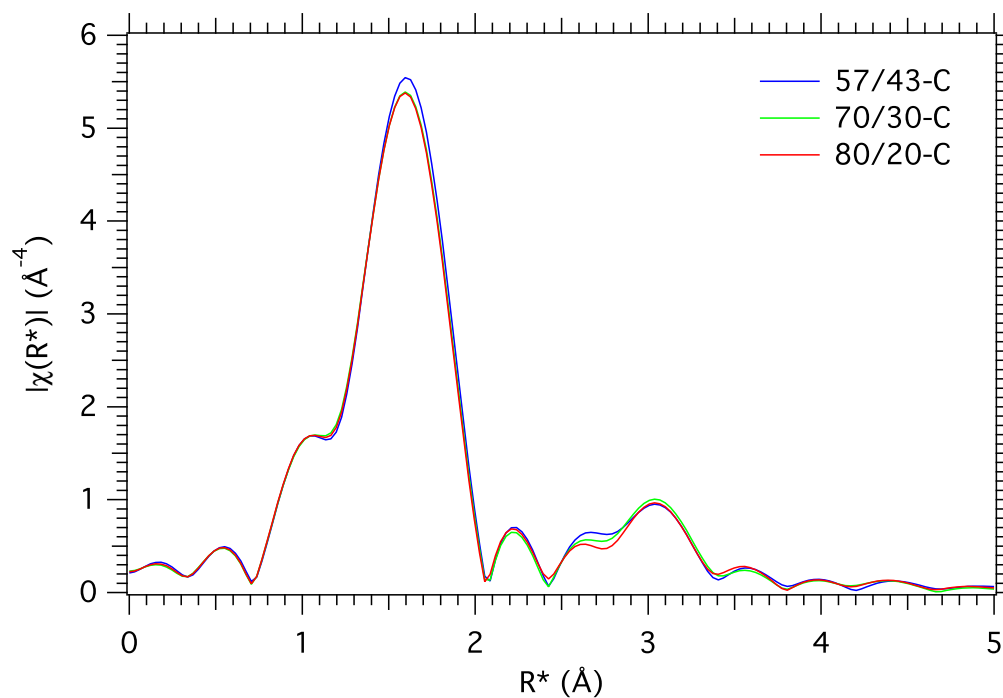
Figure 7.3: The magnitude of the Fourier transformed EXAFS data (weighted with k^3). Identical background subtractions were used for all the samples. The 57/43 sample is shown in blue, the 70/30 sample is shown in green, and the 80/20 sample is red. All the samples are from the conducting series.

7.3.1.1 Path Constraints

All paths used in a fit were constrained to have the same value for E_0 and S_0^2, with E_0 being a free parameter and $S_0^2 \equiv 0.82 \pm 0.5$. The value for S_0^2 was determined from the In_2O_3 reference sample (see Appendix B.3). For the In-O coordination shell, the coordination number (N_O), bond length (R_O), MSRD (σ_O^2), and third cumulant (C_3) were free parameters in the model.

The other two paths that were modeled were the edge-sharing Zn and In shells. The coordination numbers of each of these shells was initially set to be equal to the measured cation content in the films (see Table 2.1). The ratio of the coordination numbers was allowed as a free parameter that can be interpreted as the average cation ratio of the In next-nearest neighbors. The total number of Zn and In atoms was set at 6. The MSRD's for the In and Zn shells were constrained to be equal and one parameter was allowed to define the MSRD for both shells, σ_M^2. The relative change in the interatomic distance of the two shells was constrained to be the same value. When allowed to have independent interatomic distances the percentage change in R_i came out nearly identical for both shells. This modeling scheme results in 8 variables per sample. It was found that the most reliable data range to fit was with a k-range of $2.5 - 10$ Å^{-1} and an $R*$-range of $1.2 - 3.8$ Å. This results in 12 independent data points per sample.

7.3.2 IZO Fit Results

All six samples used identical fitting models. For all variables, the figure-of-merit, $\mathcal{F}$, was calculated for the intrinsic and conducting samples, where $\mathcal{F}$ is defined in section 5.7.4. Then, starting with the lowest $\mathcal{F}$, parameters were selected to be constrained across the data sets. This was an iterative process where variables were selected and deselected in various combinations to assure that constraining certain variables did not artificially force another parameter into a different fitting minimum. In addition to this mathematical scheme, I also looked for trends between conducting and intrinsic samples that maintained consistency across the different compositions. This method resulted in a final model where E_0 and N_O were the only parameters that remained independent

between the intrinsic and conducting samples. Thus, the three compositions each used a model
with 24 independent data points and 10 variables. A representative fit using this model is shown
in Fig. 7.4. The fits to the other sets are qualitatively the same.

Table 7.1 shows the fit parameters where no clear trends were observed, all of the parameters
shown were constrained to be identical for the intrinsic and conducting samples. The In-O bond
distance was approximately constant across the composition, but showed a noticeable decrease
compared to the In_2O_3 nearest-neighbor distance of $R_O = 2.179 \pm 0.005$ Å (Table B.1). The MSRD
for the O shell ($\sigma_O^2 \approx 0.0075$) is a value consistent with an amorphous metal oxide. Both of these
results are consistent with literature [7, 23]. The third cumulant, C_3, is a very small yet positive
number. This indicates the distribution of In-O bond distances is slightly skewed to be greater than
the average. The rather large values for χ_ν^2 are a result of fitting the data with k-weights of 1, 2
and 3 simultaneously. If only a single k-weight was used, the χ_ν^2 would drop substantially, however
the overall error bars would increase.

Table 7.1: EXAFS results from the three compositions of IZO films. All of the variables shown
were constrained to be equal for the conducting and intrinsic data sets. The statistical fit quality
for each composition is also shown.

Sample	R_O (Å)	$\sigma_O^2 \left(\text{Å}^2 \right)$	$C_3 \left(\text{Å}^3 \right)$	$\Delta R_M (\%)$	$\sigma_M^2 \left(\text{Å}^2 \right)$	χ_ν^2	$\mathcal{R}$
57/43	2.165(6)	0.0074(3)	0.0004(1)	0.1(2)	0.020(1)	188	0.0018
70/30	2.156(6)	0.0076(3)	0.0003(1)	-0.2(2)	0.019(1)	155	0.0015
80/20	2.160(6)	0.0076(3)	0.0004(1)	0.0(2)	0.020(1)	196	0.0019

The In-Zn and In-In distance were both very close to the ideal distance. This is significant
in that the In-Zn distance was calculated only assuming values for the ionic radii and that the In
and Zn centered polyhedra share a common edge. To date, no publications have been found using
EXAFS that demonstrate a potential polyhedral bonding arrangement in an amorphous thin film
of a similar system.

The importance of the Zn atom can be seen in Fig. 7.5. This is the same data as in Fig.
7.4, with one small difference in presentation. Rather than plotting only the magnitude of the
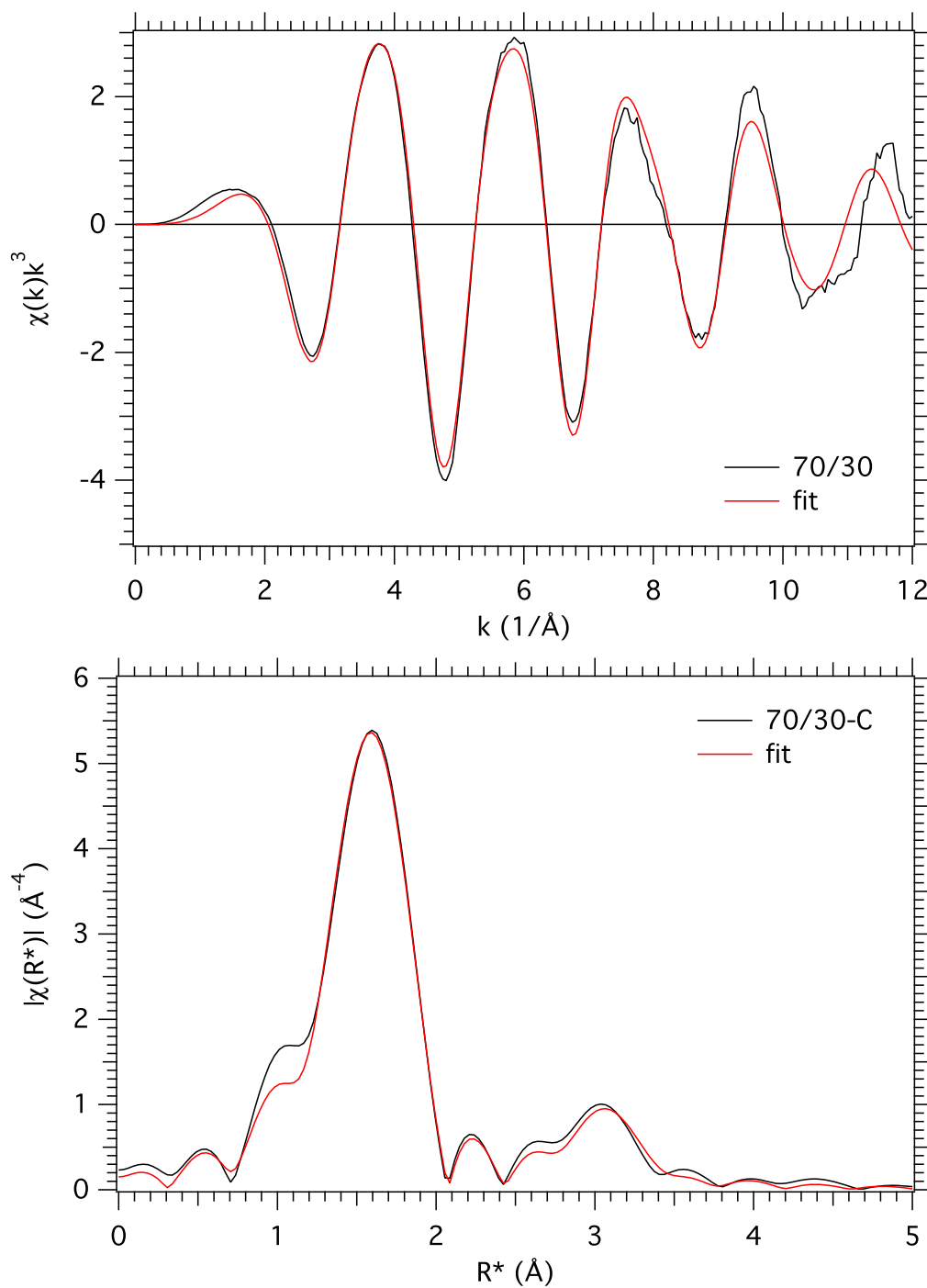
Figure 7.4: The data from an IZO 70/30 sample (black) and fit (red) shown as the k^3-weighted $\chi(k)$ (top) and $|\chi(R^*)|$ (bottom). The fit range in k was $2.5 - 10$ Å^{-1}, and the fit range in R^*-space was $1.2 - 3.8$ Å. The main features in R^*-space are fit very well.

Fourier transform, $|\chi(R^*)|$, the real portion, $\text{Re}\,[\chi(R^*)]$, is also plotted. It is important to look at the real portion of the spectrum because it can show how individual paths contribute to the final spectrum by illustrating the phase relationship between them. In addition to plotting the fit in both magnitude and real space, also included is a fit where the Zn atoms were not included. When the Zn atoms are not present, most of the amplitude at 2.6 Å is gone. Although the signal neglecting the Zn still shows oscillations in this region, they do not have the right phase to be able to create the peak at 2.6 Å. The necessity of having a Zn atom at the theoretical value provides evidence to the accuracy of the model.

7.3.2.1   In/Zn Ratio

For each sample, the ratio of In/Zn edge sharing sites was left as a free parameter. Fits were attempted where the total number of edge-sharing neighbors was a variable, but the value came out close to 6 (the crystallographic value) and had unacceptably large error bars. Therefore a fixed value of 6 was used for the total number of edge-sharing neighbors. Figure 7.6 shows a plot of the fit Zn cation content (from EXAFS) versus the bulk value (from XRF). With the exception of the 80/20 set of samples, the refined content is quite close to the nominal value. The 80/20 samples are roughly 10% off from the nominal, which is still quite close considering the simple model and limited data range. The agreement of the refined and nominal values for the composition of the film gives further evidence of the accuracy of this model.

7.3.2.2   Oxygen Coordination Number, N_O

The oxygen coordination number demonstrated a consistent trend between the conducting and intrinsic samples, as seen in Fig. 7.7. The conducting samples, grown with no additional oxygen, showed a consistent decrease in the average nearest-neighbor coordination number compared to the intrinsic samples grown with additional oxygen. The trend is weak as the values fall within the error bars. However, with EXAFS results the error bars are often overestimated when looking at relative trends and underestimated when looking at the absolute value. This is because variable
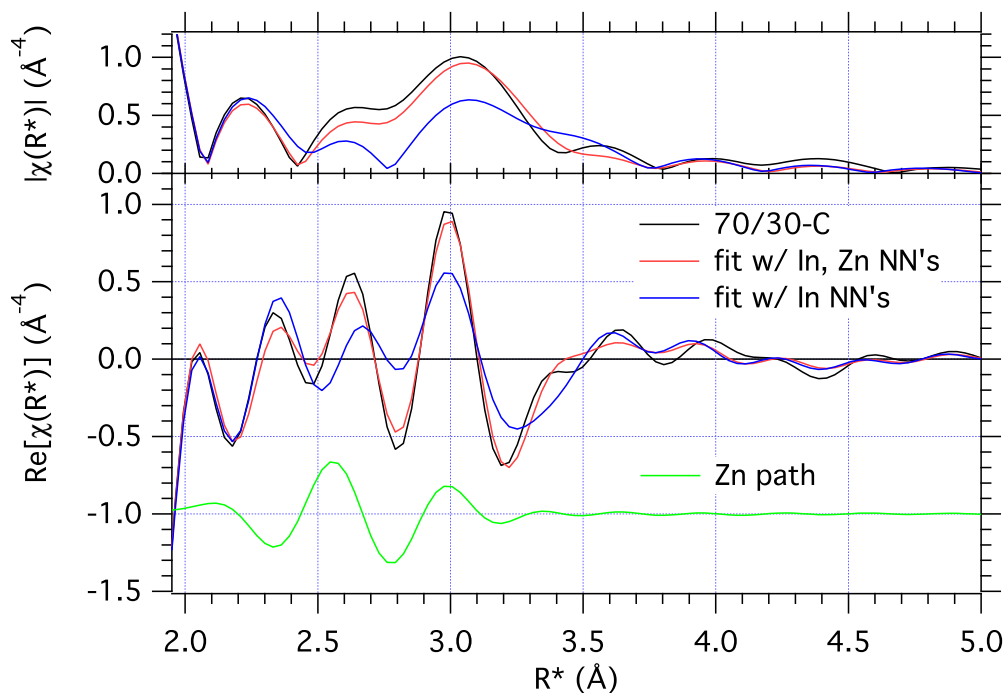
Figure 7.5: The magnitude of the Fourier transform from Fig. 7.4 is shown in the top panel. The black line is the data, the red line is the fit as shown in Fig. 7.4, and the blue line is the fit excluding the use of Zn atoms in the second shell. The real portion of the Fourier transform is shown in the bottom panel, using the same color scheme. The importance of the edge shared Zn atoms is readily apparent in the fits excluding these atoms. These atoms contributed most of the amplitude to the peak at 2.6 Å, and some amplitude to the peak at 3.1 Å. The In-Zn scattering path is shown offset in green. It is clear that this path will contribute to the amplitude at 2.6 Å.

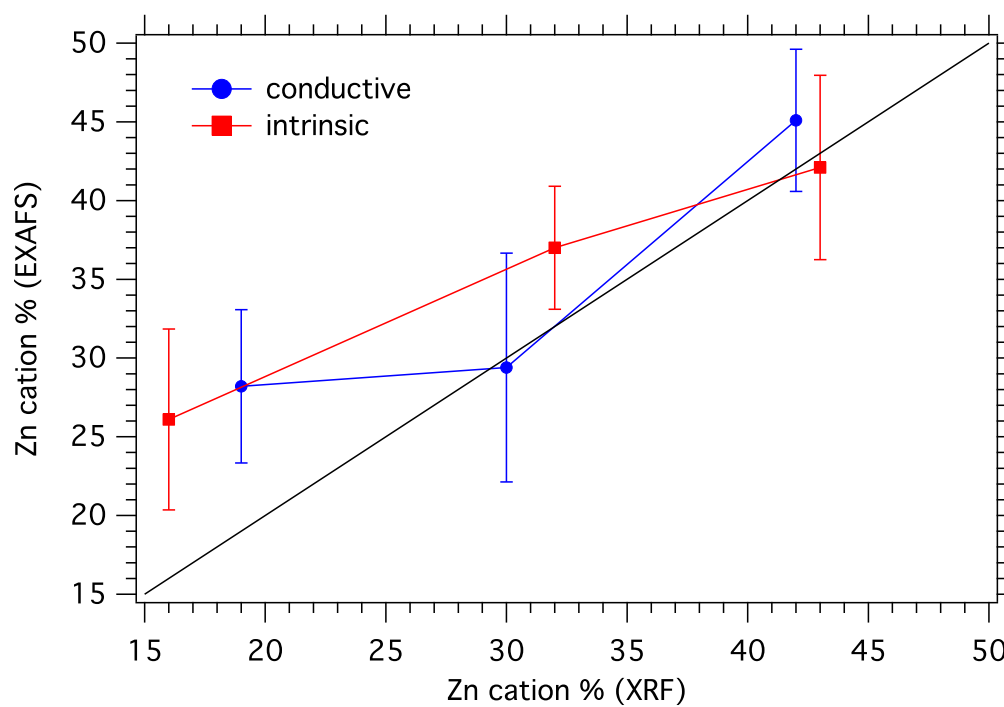Figure 7.6: The compositions refined from EXAFS compared to the compositions measured with XRF. Reported values are in Zn cation %. The conductive samples are shown as blue circles and the intrinsic as red squares. The black line is for a visual reference of 1:1 correlation between the EXAFS and XRF measurements.

correlations can change the absolute value of a parameter, but the change is consistent for all of the data sets. In this case the ideal number of oxygen atoms is 6, but these results are closer to 6.2. In Appendix B.3, it is mentioned that the S_0^2 value used is slightly underestimated. This would result in a coordination number that is slightly too large, as is seen here. The offset between samples does not follow the actual difference in conductivity, only the presence of additional oxygen. The conducting samples all had near 0.25% oxygen, while the intrinsic samples had 0.98%, 1.23%, and 1.37% content for the 57/43, 70/30, and 80/20 samples, respectively. Although it is important to note that EXAFS, in general, is less accurate in determining coordination numbers compared to bond distances. As such, this is a preliminary result that provides an interesting potential insight to a-IZO, but it must be confirmed in the follow up to this work. This is especially true considering the trend is also consistent with distortions detected in the experimental data which will be elaborated on in section 7.3.3.

7.3.2.3   Alternate Models

A significant drawback of EXAFS analysis is that there is no unique solution to a given set of data. This is why it is necessary to try many fitting models on any given data set. In spite of this drawback, if a model is attempted that does not fit the data, it can be ruled out as a potential solution. If a model is attempted that results in unphysical fit parameters or in an unstable fit, this is evidence that the model does not appropriately describe the system. In the course of analyzing this data, numerous models were used. First shell models of corundum and wurtzite structure were attempted, but only the bixbyite model produced a reasonable fit. This is not surprising given the XANES data discussed in section 7.1.

Fitting the regions beyond the first shell can be problematic due to the weak signal. Models using both In and O atoms where attempted as a solution to the peak at 2.6 Å, but neither generated acceptable results. Using O atoms, a good fit could not be found under any reasonable circumstance. When using In atoms, the fits matched the data quite well. However, the fits were not very stable, and the results they generated did not make physical sense, ruling out In as a
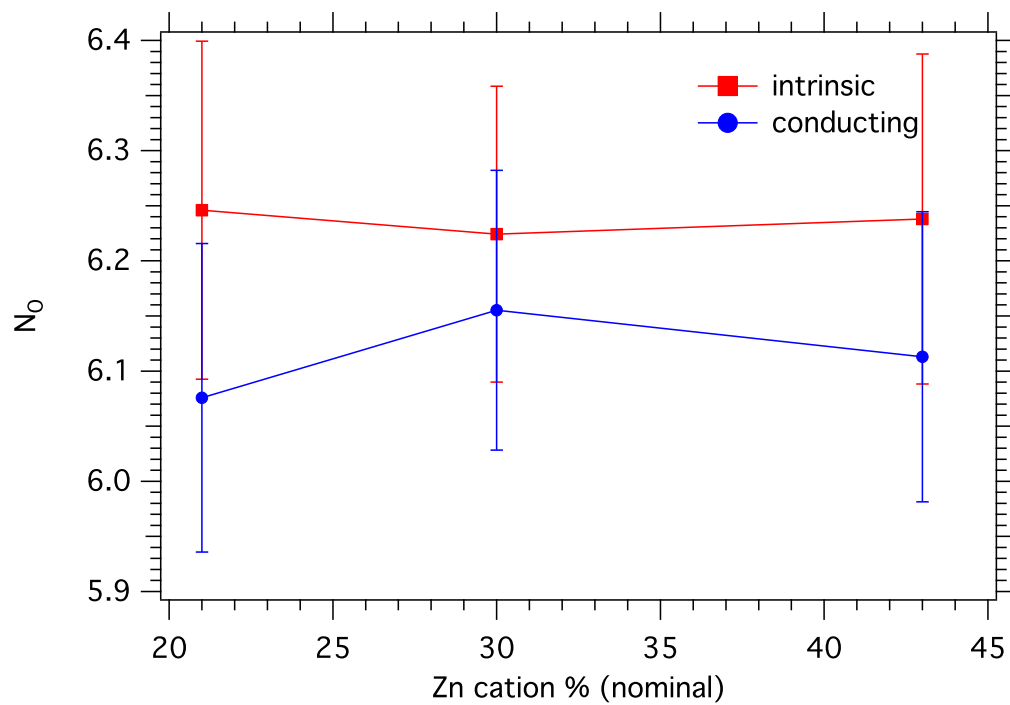
Figure 7.7: The nearest-neighbor coordination number, N_O, is plotted as a function of Zn cation content. The conducting films are shown in blue and the insulating films are red. Although the trend is not strong, it is consistent, showing a slightly decreased average coordination number ($\sim 2\%$). As a reminder, the O_2 content present during the conducting film growth was $\sim 0.25\%$ and during intrinsic film growth it was in the range of $1 - 1.4\%$ (see Table 2.1).

solution. Many different constraint schemes were also used to determine the final model, but none showed any substantial differences with the results presented.

To test the stability of the fitting model, transform ranges and background subtraction parameters were varied within reasonable bounds. When varying these parameters, the fit results would stay nearly constant, implying a stable and robust fitting model.

7.3.3   Spectral Distortions

As was mentioned in section 7.3.1, an experimental artifact caused distortions in the spectra. These artifacts were manifested by a shift in E_0 as can be seen in Fig. 7.8. As seen in the figure, the conducting samples all show a significant increase in E_0. Typically shifts on the order of one or two eV indicate a change in the oxidation state of the absorbing atom. For example, in comparing In metal, where the atom is not ionized, to In_2O_3, where it has a charge of $+3$, E_0 will shift by ~ 4 eV. This shift is easily observable in the absorption spectra of the two materials. Using this logic, the data would imply that the conducting samples are in a higher oxidation state, however this is not the case.

The typical procedure in EXAFS analysis is to align the absorption edges of a known reference material, in this case an In metal foil. The alignment uses a linear shift in the energy scale to align the peak in the first derivative of the absorption spectrum. Since the reference spectrum is collected simultaneously with the sample spectrum, any shifts in the reference spectra will also shift the data. Typically these shifts are on the order of a single eV.

The top panel of Fig. 7.9 shows the In metal absorption edge taken during the measurement of a conductive and intrinsic sample, the bottom panel shows the resulting $\chi(k)$ spectrum. Both of these spectra are measurements of the same material under identical conditions, thus the spectra should be identical in both panels. It is immediately obvious that the nodes in the low-k region of the EXAFS spectrum show a clear offset. This behavior is consistent with a shift in E_0. Figure 7.10 shows the same spectra, but the intrinsic sample has been shifted by 2 eV. The top panel again shows the absorption edge and the bottom panel shows the EXAFS spectra. With this

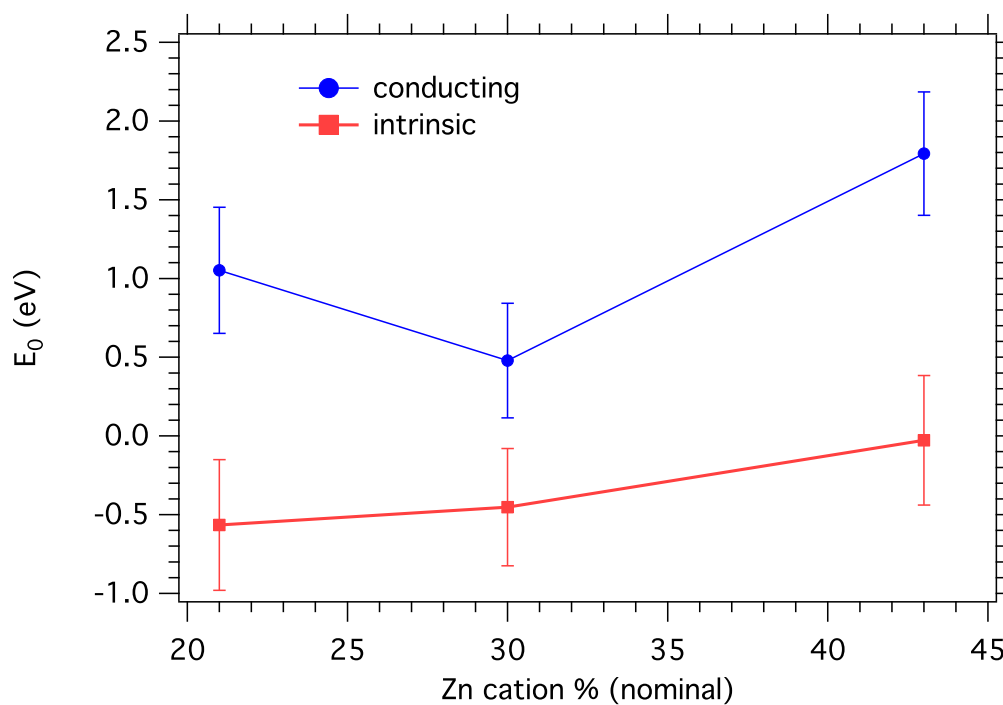Figure 7.8: The fit parameter E_0 is plotted as a function of Zn cation content. There is a very clear trend present between the conducting and insulating samples. A quick assumption would lead the experimenter to interpret this shift as meaning the conducting samples have an increased oxidation state. However, this shift has been shown to be an artifact of this particular group of experiments.

adjustment, the EXAFS data are clearly aligned and identical to each other, however a clear shift is now apparent in the absorption edge. There are still differences in the EXAFS region at less than 2.5 Å^{-1} however, this is not unexpected because this region is sensitive to the details of the background subtraction and is not often used in EXAFS analysis. These reference spectra were taken with the 57/43 samples. Notice that in Fig. 7.8 the difference in E_0 for the 57/43-C and 57/43-I samples is about 2 eV, which is exactly how much the reference spectra were shifted to align with each other. This is clearly an artifact from a change in X-ray beam illuminating the sample. There were no indications of what may have caused this change. This issue has been brought to the attention of the beamline staff, but as of the writing of this thesis no cause has been identified.

This distortion happened in such a way that it occurred between samples. Each sample was measured four times in succession, referred to as sweeps, and the four spectra averaged to increase counting statistics. During the experimental collection of these measurements, the three conducting samples were measured first, then the In_2O_3 on tape was measured followed by the three intrinsic samples. When comparing each of the four sweeps for a single sample no distortions were present. However, when looking at the final and initial sweeps of successive samples it was possible to identify that the distortion occurred between the third conducting sample and the In_2O_3 sample. All of the IZO samples, with the exception of the 57/43 conducting sample, were measured under nominally identical conditions. The 57/43 conducting sample had slightly larger horizontal slits, however this should have had a minor effect on the measured spectra. The other samples all had identical slit sizes, but the offset was around 1 eV. For the In_2O_3 sample, the horizontal slits were reduced significantly because the fluorescence signal was significantly stronger, over saturating the electronics. However, after this sample was measured they were returned to their original position. There was no obvious indication of an event occurring that may have caused this distortion.
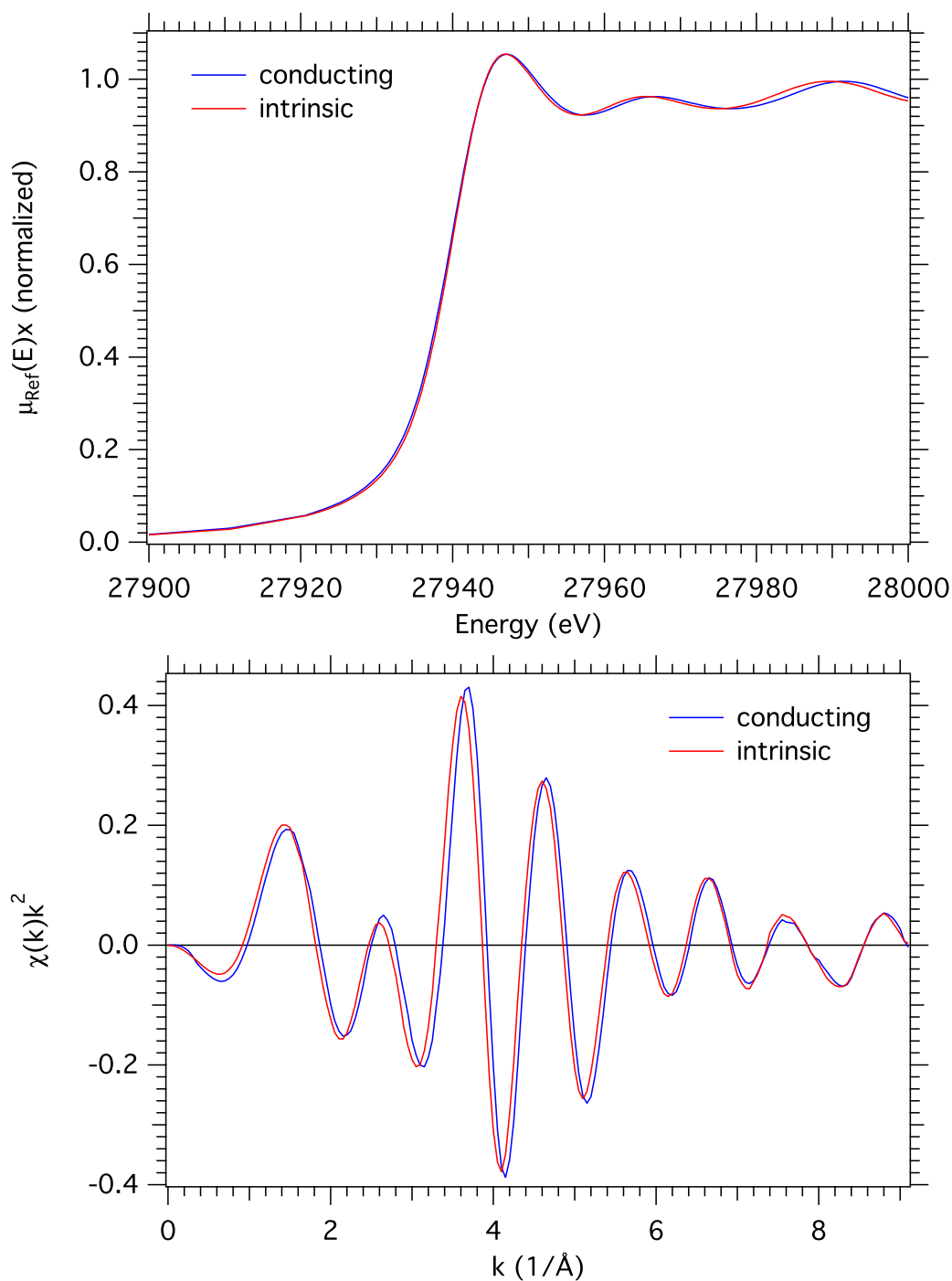
Figure 7.9: (top) The normalized absorption of an In foil as a function of X-ray energy. The conducting and intrinsic labels refer to what sample was being measured, however the data shown is of the reference foil, which was unchanged for all of measurements. The spectra were aligned by aligning the peak in the first derivative to 27940 eV. It is apparent that the intrinsic samples oscillations are rising faster after the absorption edge. (bottom) The EXAFS of the same data. It is immediately obvious that the nodes for $k \lesssim 7$ are not aligned. This behavior is consistent with a shift in E_0.
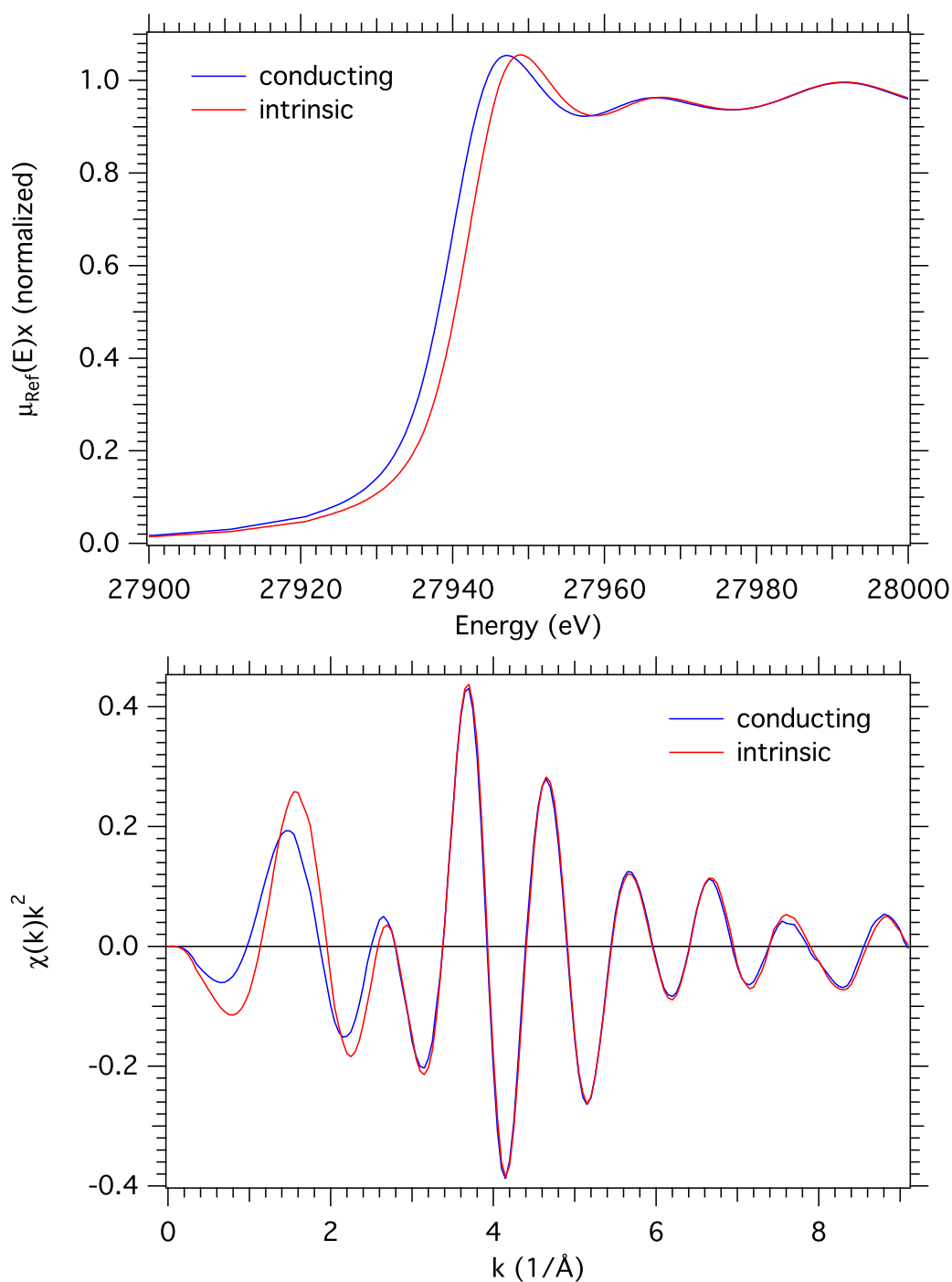
Figure 7.10: The same data as in Fig. 7.9, however for these plots an E_0 shift of 2 eV was added to the intrinsic sample. This shift made the $\chi(k)$ data well aligned. The differences in the region $k \lesssim 3$ Å^{-1} is due to the background subtraction behaving differently because of the shift. This shift created a significant shift in the apparent absorption edge of the In. These measurements are both of the same material and both plots should be identical. This indicates an equipment malfunction.

7.3.3.1   Validity of Results

It is important to remember that many of the parameters in EXAFS analysis are correlated. E_0 and R_i are strongly correlated, so a shift in one will also cause a corresponding shift in the other. In order to separate which parameters were being influenced by the distortions, the data were fit under various conditions. The results presented used the "standard" method of aligning the absorption edges, as in Fig. 7.9. The data was also fit with the EXAFS oscillations of the reference spectra aligned, as in Fig. 7.10. Fits were also performed by choosing the initial value of E_0 anywhere from the bottom of the absorption edge to the top of the edge. The results from each method came out qualitatively the same. However, fitting data with the reference EXAFS oscillations aligned is somewhat dubious as the two data sets are on a different energy and k scale, thus they are not consistent with each other. The shifts in the fit parameters were within the error bars, meaning that the signal from the edge-sharing Zn atom is still a necessary part of the fitting model. Regardless of the alignment scheme used, the fit result for the cation ratio was nearly unchanged. The most sensitive trend to these shifts, other than E_0, was the oxygen coordination number. When the data were aligned in k-space, the oxygen coordination numbers shifted closer together. The differences seen in this parameter were already very small, and these shifts made the numbers nearly identical.

7.4   Concluding Remarks

This chapter presented the results on the EXAFS measurements of IZO films at the In-edge. The two conclusions drawn from these measurements are:

(1) Indium atoms are six-fold (octahedrally) coordinated with oxygen, as in c-In_2O_3.

(2) Indium's second-nearest neighbors consist of edge-shared zinc and indium at a concentration near what is found in the bulk, with zinc atoms being slightly closer.

The six-fold nature of indium was determined qualitatively from XANES and quantitatively from the first shell of the EXAFS spectra. The MSRD of the oxygen atoms in the amorphous films

was somewhat higher than what would be found in c-In_2O_3. This indicates that although some additional disorder is present, the material still closely resembles a crystalline material, at the length scale of a nearest neighbor. EXAFS analysis of the second shell found that both In and Zn atoms can occupy edge-sharing positions on a central InO_6 octahedron. Using a hard-sphere approximation and tabulated values for ionic radii, I calculated that the In-Zn separation in this arrangement should be 3.1 Å and the In-In separation should be 3.4 Å. When modeling a Zn and In atoms at this distance, the fit results indicated the calculated value to be within 0.5% of the nominal value. The fit determined the proper ratio of In/Zn next-nearest neighbors to within 10% of the measured bulk concentration, giving further strength to the fitting model. The MSRD of the next-nearest neighbors is significantly larger than would be found in a crystalline material, indicating that beyond a few Å the structural coherence of the structure is significantly diminished.

This chapter also discussed experimental distortions that were discovered in the spectra. The distortion showed up as an apparent shift in the E_0 parameter between the intrinsic and conducting sample sets. The fitting routine was able to "see" around this distortion and place the effect into the E_0 results. To verify this, many fits were attempted where the data were intentionally shifted, creating artificial shifts in E_0. The main conclusions drawn did not change as a result of these shifts. The absolute values of the results did show correlation with these shifts, however the trends within the parameters remained mostly consistent. The one notable exception is the oxygen coordination number, N_O. The shifts in this parameter, although small, decreased the separation between the conducting and insulating samples. The data could not be remeasured for this paper, because the availability of facilities to perform these measurements is extremely limited. Any future work done to build on these results should first consider it the highest priority to remeasure these samples and confirm the results presented.

Chapter 8

Zn-Edge XAFS Results

8.1   Zn-edge XANES

As discussed in Sec. 5.2, XANES allows a qualitative method to compare local bonding environments. Figure 8.1 shows the normalized absorption spectrum for a representative IZO film and crystalline ZnO. Although significant differences are present, the general trend of the features is similar. The peak at 9680 eV has been attributed to a multiple-scattering resonance resulting from an increase in medium-range ordering around the Zn site [79, 80]. In studies of similar crystalline systems, it has been observed that the Zn atom resides on an octahedral Zn site. The XANES evidence for this is seen by a white line peak intensity that is increased $\sim 30\%$ compared to the tetrahedral Zn found in ZnO [21, 81, 82]. However, in amorphous systems it has recently been observed that the Zn atom can retain its tetrahedral local bonding environment, where a decrease in the white line intensity is observed [7]. This decrease has also been theoretically verified by XANES simulations performed with different bonding environments [83].

8.2   ZnO Ideal Structure

ZnO naturally crystalizes into the wurtzite structure. This is a hexagonal structure (space group P6$_3$mc) with unit cell parameters of $a = b = 3.25$ nm, $c = 5.21$ nm [32]. The Zn atoms are tetrahedrally coordinated, with the each O atom being shared among 4 polyhedra. Three of the O atoms in the tetrahedron are at 1.97 Å, and 1 is found 1.99 Å. The measured ZnO spectra are well described by the wurtzite structure as shown in Appendix B.4.
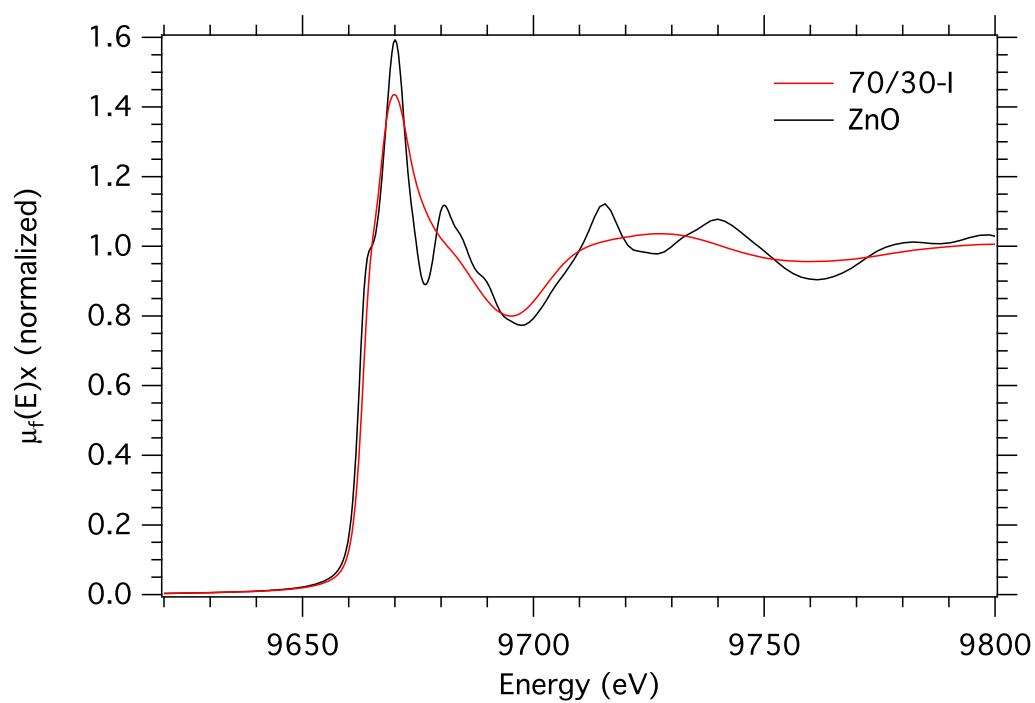
Figure 8.1: The normalized absorption spectra comparing the XANES region of a intrinsic 70/30 film (red) to crystalline ZnO powder on tape (black). The 70/30-I spectrum is typical for all a-IZO samples.

8.3   Zn-edge EXAFS

Figure 8.2 compares the intrinsic samples of all three compositions. The main peak at 1.5 Å and the small peak at 2.9 Å both show consistent trends as a function of metals composition. As with the results from the In-edge EXAFS measurements, the strongest signal is from the nearest neighbor Zn-O shell. Unlike the In-edge EXAFS, a consistent trend is the main Zn-O scattering shell with composition is apparent. The trend with composition just below 3 Å is even more apparent than in the In-edge EXAFS.

8.3.1   IZO Model

The first shell of the Zn-edge EXAFS data was fit using a wurtzite model. It was simplified slightly by using all 4 O atoms at a single distance, rather than having the fourth atom at a slightly longer distance. The fit results were indistinguishable between the ideal structure and the simplified version. The conductive and intrinsic models were fit simultaneously. The parameters were constrained following the methods in section 5.7.4. For the first shell, the E_0, MSRD (σ_O^2) and C_3 parameters were constrained to be identical across the data sets. The coordination number (N_O), and Zn-O bond length (ΔR_O) were independent for each data set. Due to time constraints, no suitable model was developed for the outer shells of the Zn-edge measurements. This scheme used a total of 7 variables for the two data sets. The data sets were Fourier transformed using a range of $k = 2.5 - 10.0$ Å^{-1}, and fit using an R^*-range of $R^* = 1 - 2.3$ Å. This produced a total of 12 independent data points for the pair of data sets. The fit results of powdered ZnO (see Appx. B.4) found that $S_0^2 = 0.91 \pm 0.07$ is an appropriate value for the Zn-edge IZO measurements.

8.3.2   IZO Fit Results

The fit to a typical data set can be in Fig. 8.3, where the top panel shows the $\chi(k)k^3$ spectrum and the bottom shows the magnitude of the Fourier transform, $|\chi(R^*)|$. The fit results of all the data sets can be seen in Table 8.1. When the In content increases the amplitude of the first shell
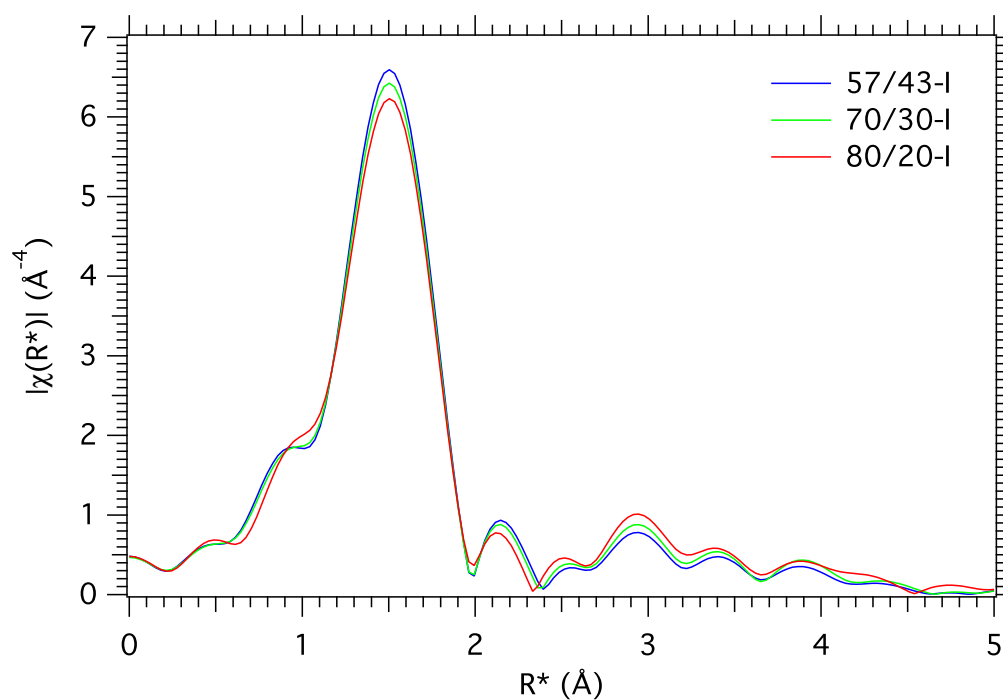
Figure 8.2: The Fourier transformed $\chi(R^*)$ spectrum comparing the compositions of the intrinsic set of samples. The 57/43-I sample is blue, the 70/30-I sample is green and the 80/20-I sample is red. Distinct trends with composition are present at 1.5 Å and the region surrounding 3 Å.

peak shows a slight decrease. This is due to the increasing MSRD as a function of In content, indicating that when the Zn ratio is relatively small, the tetrahedral cage shows more distortions in the Zn-O distance. This is because the crystal structure of In_2O_3 trying to dominate the films. The 80/20-I sample shown in Fig. 8.2 has an In cation content of 84%. Previous studies have found that when the In cation content gets above the 90% range, the films begin to lose their amorphous nature and take on the crystal structure of In_2O_3 [5]. For the a-IZO films $R_O \approx 1.95$ Å, which is slightly contracted from the average crystalline distance of 1.98 Å. This contraction is consistent with what was observed at the In-edge where the In-O distance was slightly contracted in the films compared to c-In_2O_3. The rest of the fit results are nearly identical as a function of composition, although the 80/20 samples show a slight shift in E_0 and N_O.

Table 8.1: The fit results of the IZO films. The variables spanning two rows of the same composition were constrained to be equal for the conducting and intrinsic data sets. The statistical fit quality for each composition is also shown.

Sample	E_0 (eV)	N_O	R_O (Å)	$\sigma_O^2 \left(\text{Å}^2 \right)$	$C_3 \left(\text{Å}^3 \right)$	χ_ν^2	$\mathcal{R}$
57/43-C	1.6(5)	4.14(10)	1.953(8)	0.0080(4)	-0.0003(2)	1067	0.0006
57/43-I		4.15(11)	1.953(8)				
70/30-C	1.4(7)	4.15(13)	1.953(10)	0.0083(5)	-0.0004(2)	2340	0.0011
70/30-I		4.13(15)	1.951(10)				
80/20-C	0.6(8)	4.35(16)	1.947(12)	0.0092(6)	-0.0006(3)	2972	0.0015
80/20-I		4.37(17)	1.948(12)				

Although no significant changes have been observed as a function of composition, the results are still significant because they show that Zn is tetrahedrally coordinated in a-IZO. This has been recently confirmed in a-IZTO [7], however in a-IGZO Zn has been found to take on a 5-fold coordination [23, 24]. The 4-fold coordination is further confirmed by the Zn-O separation of ~ 1.95 Å found for the IZO films. If the Zn atoms were 5- or 6-fold coordinated, the Zn-O separation would be closer to 2.07 or 2.14 Å, respectively. This is due to the increased size of the Zn ion as the coordination increases [7, 78].
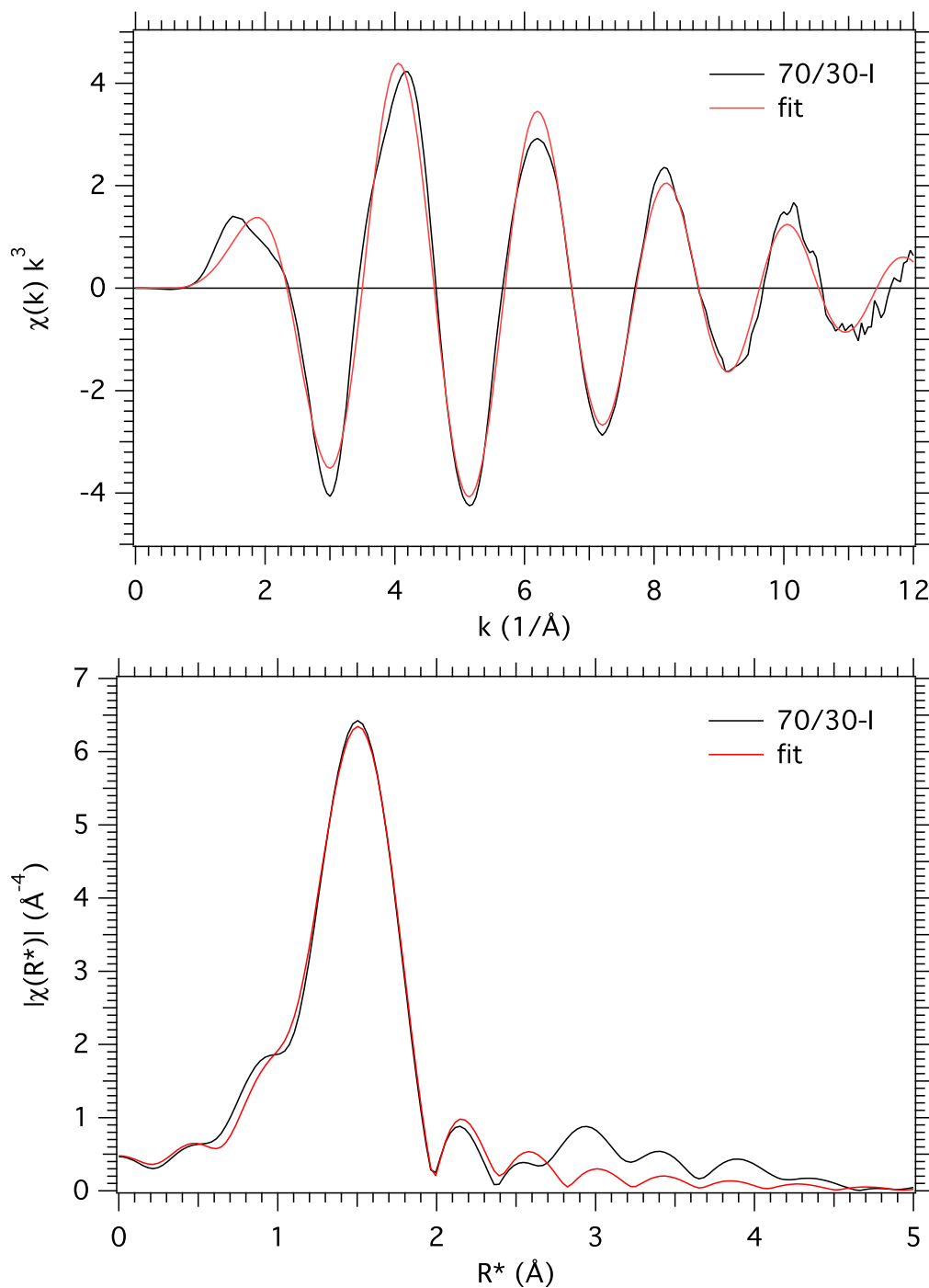
Figure 8.3: (top) The EXAFS of the 70/30-I sample and fit. (bottom) The magnitude of the Fourier transformed data and fit. The fit is representative of all the a-IZO samples.

8.3.2.1   Preliminary Results of Zn Next-Nearest Neighbors

Although a suitable model for the outer shells has not been developed, initial results of that endeavor are promising. In Fig. 8.4, a fit to the 70/30-I data set is shown with an In-Zn separation identical to that in Table 7.1. The original fit with out the In atom is also shown for reference. The peak of the In scattering occurs almost exactly at $R^*2.9$ Å, which is where the trend with composition is seen in Fig. 8.2. In this case the Zn-In distance was fixed at $R = 3.1$ Å, and the MSRD and coordination was allowed to fit the data. A model that gave results consistent with the In-edge was not developed, due to time constraints.
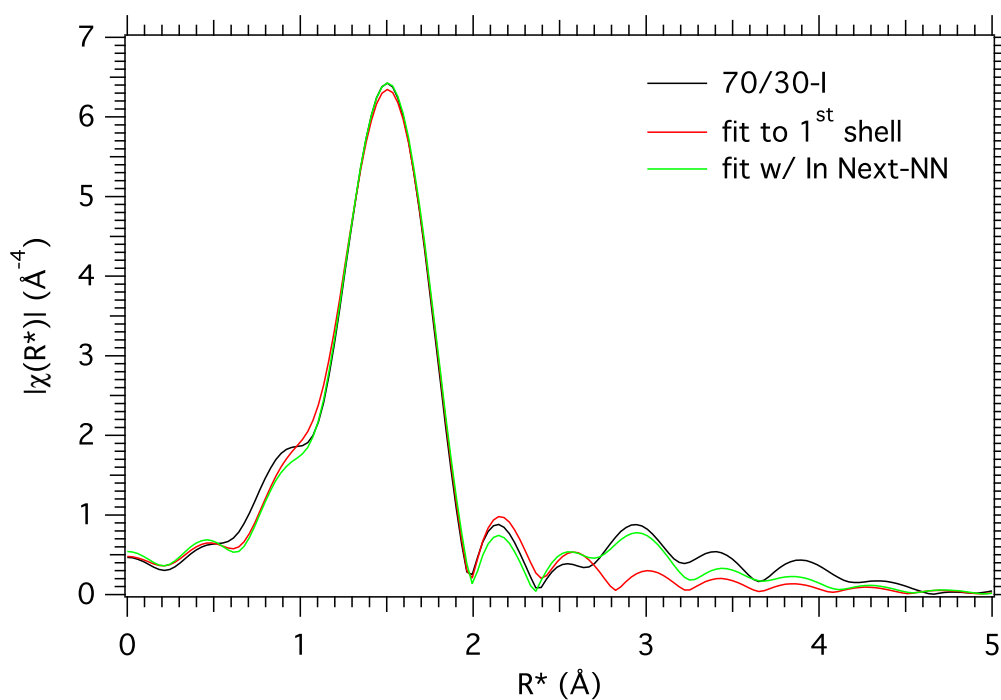

Figure 8.4: The $\chi(R^*)$ data for the 70/30-I sample (black) shown with a fit to the Zn-O shell only (red) and a preliminary fit using a Zn-In separation of 3.1 Å (green).

8.4   Concluding Remarks

This chapter has presented evidence from the Zn-edge XAFS experiments that Zn occupies a tetrahedral site in a-IZO. This arrangement has been confirmed by theoretical and experimental

evidence from both XANES and EXAFS. Although there are several literature results reporting the local arrangements of quaternary amorphous systems, such as a-IGZO [23, 24] and a-IZTO [7], the EXAFS literature on a-IZO is lacking. There is one other literature reference using EXAFS to analyze a-IZO [19]. The authors of that article found that 4.0 O atoms coordinated each Zn atom, however these results are dubious. There is no explanation of what data ranges were used, or how the nearest neighbor shells were modeled. No other parameters used in the model were given. Amorphous IZO has been studied by PDF measurements and molecular dynamics simulations [20]. This work concluded that the average O coordination number around Zn atoms was $5.0 - 5.3$, depending on the cation ratios.

In section 7.3.3, a distortion was observed in the measured EXAFS data, resulting in a shift of E_0 between samples. At the Zn-edge, the thickness of substrates caused considerable attenuation in the beam, meaning the no EXAFS features of the Zn metal reference foil were observable. The presence of this distortion at the Zn-edge can only be inferred from the results of E_0. These results indicate that a distortion of this nature did not occur for the 57/43 or 70/30 group of samples because the E_0 parameter was nearly identical for all four data sets. The 80/20 samples showed a slight shift in this parameter, although it was within the error bars of the parameter. Thus, it can be concluded that this distortion was limited to the In-edge measurements.

Initial results in describing next-nearest neighbor shells are promising. When the distance of this shell is constrained to the theoretical distance of 3.1 Å, there is good agreement with the data and a Zn-In shell at this distance. A model consistent with both the In-edge and Zn-edge measurements has not been developed, although doing so would provide strong evidence for the conclusions from the In-edge measurements.

Chapter 9

Conclusions

Amorphous TCOs are a class of materials gaining interest in the scientific community, because of their many potential uses in electronic devices. Their properties can be tuned for a wide range of applications, and their lack of crystallinity results in many desirable properties. Many different materials systems of a-TCOs have been well characterized from a device performance perspective. For example, the ability to control properties such as the optical transmission and conductivity under a variety of conditions has been well studied. One aspect of a-TCOs not as well understood is the atomic structure of these materials and the impact structure has on the bulk properties. The nature of amorphous materials makes typical X-ray measurement methods, such as XRD, of little use in determining the structural description of a sample. In recent years, the advancement and availability of synchrotron based measurements has make measuring the atomic structure of a-TCOs a reality. This thesis focused on the structural characterization of one particular a-TCO, amorphous In-Zn-O (a-IZO). This material can be created with a variety of different In/Zn ratios and the conductivity can be controlled over several order of magnitude, making it a candidate for use in applications from photovoltaics to transparent displays.

A broad overview has been given of the theoretical and experimental descriptions of both X-ray Absorption Fine Structure (XAFS) and the Pair-Distribution Function (PDF), both of which are specialized techniques used to measure the atomic structure of materials. The nature of these measurements requires synchrotron-based radiation. These techniques are especially powerful because they have the capability to measure the atomic structure of amorphous materials on very

short length scales. XAFS and PDF measurements have been used to study the structure of a-IZO, with a particular emphasis on XAFS. For this work, three different compositions of a-IZO studied. For each composition two separate samples were studied: a "conducting" sample, grown without additional oxygen, and an "intrinsic" sample, grown with additional oxygen.

The PDF results show that a-IZO has a short-range structure (< 5 Å) that is qualitatively similar to that crystalline In_2O_3. The nearest-neighbor bonding arrangements in a-IZO are almost identical to that of the crystalline oxide. The next-nearest neighbors are qualitatively similar, although the large spread in bond angles causes the structure to lose any long-range periodicity.

There are three primary conclusions from XAFS analysis. It was found that in a-IZO...

(1) Indium is octahedrally (6-fold) coordinated with oxygen. The nearest neighbor coordination of indium was determined by both XANES and EXAFS analysis to be ~ 6 oxygen atoms. EXAFS analysis found that the conducting samples showed a slight decrease in the number of nearest neighbor oxygen atoms compared to the intrinsic samples. This trend, while consistent, was weak and spectral distortions present in the measurements clouds the reliability of this result. As such, it should be viewed as a preliminary conclusion until confirmed by future work. The MSRD (σ^2) of the nearest neighbor oxygen shell was slightly higher than what is found in c-In_2O_3, as would be expected with an amorphous material. For this scattering shell, no significant trends were observed as a function of composition.

(2) Zinc is tetrahedrally (4-fold) coordinated with oxygen. An average oxygen coordination number of ~ 4 was found for zinc atoms using XANES and EXAFS analysis. The MSRD for this shell showed a slightly decreasing trend as the zinc content was increased, although no conclusions can be drawn at this trend at this time.

(3) Indium and zinc centered polyhedra form edge-sharing linkages. This was concluded by analyzing the In-edge EXAFS data, and is tentatively supported by the Zn-edge measurements. To accomplish this, a model based on the bixbyite structure of crystalline In_2O_3 was constructed. In crystalline In_2O_3, each octahedron shares 6 edges with a neighboring octahedron. The edge-sharing octahedra give rise to In-In next-nearest neighbor distance of 3.35 Å. Using a

hard sphere approximation and the tabulated ionic radii values, this distance is calculated to be 3.4 Å. Using these same assumptions, but replacing an In atom with a Zn atom, the In-Zn separation is calculated to be 3.1 Å. The In-Zn distance from the EXAFS fits was within 0.5% of this value. The ratio of In to Zn edge-sharing polyhedra was found to be within 10% of the bulk composition measurement, giving further credence to the accuracy of the model. The spectral distortions present for the In-edge EXAFS measurements have been thoroughly tested on these results and found to have no significant influence on them. To date, there have been no publications on next-nearest neighbor bonding arrangements using XAFS analysis on similar systems.

In conclusion, EXAFS analysis found that both the In and Zn atoms retain a nearest neighbor structure nearly identical to their native oxides. It was also found In- and Zn-centered polyhedra form edge-sharing units, as in c-In_2O_3, with the ratio of In/Zn next-nearest neighbors within $\sim 10\%$ of the bulk composition. The desire of each metal to form its native oxide, coupled with the incompatibility of these structures over longer scales, leads to the amorphous nature of a-IZO.

9.1   Future Work

While many results were presented in this thesis, many questions arose as a part of this work. In closing, some of the potential work that could build on the results of this thesis will be discussed.

In light of the experimental distortions discussed in section 7.3.3, the most important next step is a re-measurement of the EXAFS spectra. As was discussed, the distortions are expected to have a small effect on the results of this work, however that assumption must be verified. The results presented on the differences found between intrinsic and conducting IZO samples should also be validated.

Another round of experiments could be used to obtain data with a higher k-range, which would be beneficial in two respects. First, it would allow greater statistical certainty simply by creating more independent data points. Second, the information from heavier scattering elements have a greater contribution to the EXAFS spectrum at higher k-values. This additional information could aid in creating a model that also includes the vertex sharing polyhedra that were excluded

in this work.

Another valuable avenue of work would be to model the PDF data with the model used for the EXAFS data. Consistency between these two experimentally independent techniques would solidify the conclusions presented. Creation of powdered a-IZO samples would also prove beneficial in this task. As shown in section 4.2.2, powder samples will both greatly improve the data quality and decrease the measurement time. The increased resolution in the data would help clarify the small variations between samples.

Yet another technique which would yield great insight into this material system is the measurement of the *differential* PDF (d-PDF). This technique uses the same measurement principle as the PDF discussed in Chapter 3 with one additional important feature, the ability to tune the X-ray energy. The measurements take advantage of the fact that atoms scatter X-rays very differently just below their absorption edge compared to just above it. This difference in scattering behavior allows the experimenter to generate PDF's that are element specific, similar to XAFS. For example a PDF could be created consisting only of In-In or In-Zn scattering pairs. A measurement of this type could provide concrete evidence of how Zn and In centered polyhedra are bonded to each other. However, these measurements are significantly more difficult than the PDF experiments described in this thesis. A detailed discussion of this, and other, scattering methods can be found in [28].

Lastly, this project began with the hope of using a novel model that had been previously developed for another amorphous system, metallic glasses. It is called the "efficient cluster packing" (ECP) model and was developed by Daniel Miracle. It has demonstrated significant success in predicting the PDFs of metallic glasses from both neutron and X-ray scattering experiments [84]. It has also explained the medium-range order of these materials and why the most stable compounds form only with certain atomic ratios [85]. Although initial results on a-IZO have not been conclusive, the ECP model may still yield insights in the medium range ordering of amorphous oxide glasses. A detailed knowledge of the atomic structure could lead to the development of new materials with engineered properties to match a particular application.

Bibliography

[1] D. Ginley and C. Bright, "Transparent conducting oxides," <u>MRS Bulletin</u>, vol. 25, no. 8, pp. 15–18, Aug 2000.

[2] E. Fortunato, D. Ginley, H. Hosono, and D. Paine, "Transparent conducting oxides for photovoltaics," <u>MRS Bulletin</u>, vol. 32, no. 03, pp. 242–247, Mar 2007.

[3] B. G. Lewis and D. C. Paine, "Applications and processing of transparent conducting oxides," <u>MRS Bulletin</u>, vol. 25, no. 08, pp. 22–27, 2000.

[4] A. Leenheer, J. Perkins, M. V. Hest, J. Berry, R. O'hayre, and D. Ginley, "General mobility and carrier concentration relationship in transparent amorphous indium zinc oxide films," <u>Physical Review B</u>, vol. 77, no. 11, p. 115215, Mar 2008.

[5] M. P. Taylor, D. W. Readey, M. F. A. M. V. Hest, C. W. Teplin, J. L. Alleman, M. S. Dabney, L. M. Gedvilas, B. M. Keyes, B. To, J. D. Perkins, and D. S. Ginley, "The remarkable thermal stability of amorphous In-Zn-O transparent conductors," <u>Advanced Functional Materials</u>, vol. 18, no. 20, pp. 3169–3178, Oct 2008.

[6] T. Kamiya, K. Nomura, and H. Hosono, "Present status of amorphous In–Ga–Zn–O thin-film transistors," <u>Science and Technology of Advanced Materials</u>, vol. 11, p. 044305, 2010.

[7] C. Hoel, S. Xie, C. Benmore, C. Malliakas, J.-F. Gaillard, and K. Poeppelmeier, "Evidence for tetrahedral zinc in amorphous $In_{2-2x}Sn_xZn_xO_3$ (a-ZITO)," <u>Zeitschrift für anorganische und allgemeine Chemie</u>, vol. 637, no. 7-8, pp. 885–894, 2011.

[8] J. E. Medvedeva and C. L. Hettiarachchi, "Tuning the properties of complex transparent conducting oxides: Role of crystal symmetry, chemical composition, and carrier generation," <u>Physical Review B</u>, vol. 81, no. 12, p. 125116, Mar 2010.

[9] J. Cui, A. Wang, N. Edleman, J. Ni, P. Lee, N. Armstrong, and T. Marks, "Indium tin oxide alternatives - high work function transparent conducting oxides as anodes for organic light-emitting diodes," <u>Advanced Materials</u>, vol. 13, no. 19, pp. 1476–+, Jan 2001.

[10] K. Nomura, H. Ohta, A. Takagi, T. Kamiya, M. Hirano, and H. Hosono, "Room-temperature fabrication of transparent flexible thin-film transistors using amorphous oxide semiconductors," <u>Nature</u>, vol. 432, no. 7016, pp. 488–492, Jan 2004.

[11] J. D. Perkins, M. F. A. M. van Hest, M. P. Taylor, and D. S. Ginley, "Conductivity and transparency in amorphous In-Zn-O transparent conductors," <u>International Journal of Nanotechnology</u>, vol. 6, no. 9, pp. 850–859, 2009.

[12] A. A. Dameron, D. C. Miller, N. George, B. To, D. S. Ginley, and L. Simpson, "Tensile strain and water vapor transport testing of flexible, conductive and transparent indium–zinc-oxide/silver/indium–zinc-oxide thin films," Thin Solid Films, vol. 519, no. 10, pp. 3177–3184, Jan 2011.

[13] J. D. Jorgenson, in Unites States Geological Survey: Mineral Commodity Summary, 2004, pp. 80–21.

[14] J. F. Carlin Jr., in Unites States Geological Survey: Mineral Commodity Summary, 2007, pp. 78–79.

[15] A. C. Tolsin, in Unites States Geological Survey: Mineral Commodity Summary, 2011, pp. 74–75.

[16] J. Perkins, T. Gennett, J. Leisch, R. Sundaramoorthy, I. Repins, M. van Hest, and D. Ginley, "Amorphous transparent conductors for PV applications," in Photovoltaic Specialists Conference (PVSC), 2010 35th IEEE, june 2010, pp. 000 989 –000 991.

[17] M.-F. Chen, K. moh Lin, and Y.-S. Ho, "Effects of laser-induced recovery process on conductive property of SnO_2:F thin films," Materials Science and Engineering: B, vol. 176, no. 2, pp. 127 – 131, 2011.

[18] K. Chen, F. Hung, S. Chang, J. Liao, C. Weng, and Z. Hu, "The influences of plasma ion bombarded on crystallization, electrical and mechanical properties of Zn-In-Sn-O films," Applied Surface Science, vol. 258, no. 3, pp. 1157 – 1163, 2011.

[19] F. Utsuno, H. Inoue, Y. Shimane, T. Shibuya, K. Yano, K. Inoue, I. Hirosawa, M. Sato, and T. Honma, "A structural study of amorphous In_2O_3-ZnO films by grazing incidence X-ray scattering (GIXS) with synchrotron radiation," Thin Solid Films, vol. 516, no. 17, pp. 5818–5821, 2008.

[20] T. Eguchi, H. Inoue, A. Masuno, K. Kita, and F. Utsuno, "Oxygen close-packed structure in amorphous indium zinc oxide thin films," Inorganic Chemistry, vol. 49, no. 18, pp. 8298–8304, Sep 2010.

[21] D. E. Proffit, D. B. Buchholz, R. P. H. Chang, M. J. Bedzyk, T. O. Mason, and Q. Ma, "X-ray absorption spectroscopy study of the local structures of crystalline Zn-In-Sn oxide thin films," Journal of Applied Physics, vol. 106, no. 11, p. 113524, Jan 2009.

[22] T. Moriga, A. Fukushima, Y. Tomonari, S. Hosokawa, I. Nakabayashi, and K. Tominaga, "Crystallization process of transparent conductive oxides $Zn_kIn_2O_{k+3}$," Journal of Synchrotron Radiation, vol. 8, no. 2, pp. 785–787, 2001.

[23] D.-Y. Cho, J. Song, K. D. Na, C. S. Hwang, J. H. Jeong, J. K. Jeong, and Y.-G. Mo, "Local structure and conduction mechanism in amorphous In-Ga-Zn-O films," Applied Physics Letters, vol. 94, no. 11, p. 112112, Jan 2009.

[24] K. Nomura, T. Kamiya, H. Ohta, T. Uruga, M. Hirano, and H. Hosono, "Local coordination structure and electronic structure of the large electron mobility amorphous oxide semiconductor In-Ga-Zn-O: Experiment and ab-initio calculations," Physical Review B, vol. 75, no. 3, p. 035212, Jan 2007.

[25] B. D. Cullity and S. R. Stock, Elements of X-Ray Diffraction. Englewood Cliffs: Prentice Hall, 2001.

[26] P. Scherrer, "Estimation of the size and internal structure of colloidal particles by Röntgen rays," Royal Society of Sciences, vol. 2, p. 98, 1918, german.

[27] B. Warren, "Scattering by noncrystalline forms of matter," in X-Ray Diffraction. New York: Dover Publications, 1990, ch. 10.

[28] T. Egami and S. J. L. Billinge, Underneath the Bragg Peaks. Amsterdam: Pergamon, 2003.

[29] R. Palais, "π is wrong!" The mathematical intelligencer, Jan 2001.

[30] D. A. Keen, "A comparison of various commonly used correlation functions for describing total scattering," Journal of Applied Crystallography, vol. 34, no. 2, pp. 172–177, Apr 2001.

[31] C. L. Farrow, P. Juhas, J. W. Liu, D. Bryndin, E. S. Boin, J. Bloch, T. Proffen, and S. J. L. Billinge, "PDFfit2 and PDFgui: computer programs for studying nanostructure in crystals," Journal of Physics: Condensed Matter, vol. 19, no. 33, p. 335219, 2007.

[32] P. Villars and L. D. Calvert, Pearson's Handbook of Crystallographic Data for Intermetallic Phases. Metals Park, OH: American Society for Metals, 1985, vol. 3.

[33] A. P. Hammersley, "Fit2d v9.129 reference manual v3.1," ESRF98HA01T, ESRF Internal Report, 1998.

[34] A. P. Hammersley, S. O. Svensson, M. Hanfland, A. N. Fitch, and D. Hausermann, "Two-dimensional detector software: From real detector to idealized image or two-theta scan," High Pressure Research, vol. 14, no. 4, pp. 235–248, 1996.

[35] A. P. Hammersley, S. O. Svensson, A. Thompson, H. Graafsma, A. Kvick, and J. P. Moy, "Calibration and correction of distortions in two-dimensional detector systems," Review of Scientific Instruments, vol. 66, no. 3, pp. 2729–2733, 1995.

[36] X. Qiu, J. W. Thompson, and S. J. L. Billinge, "PDFgetX2: a GUI-driven program to obtain the pair distribution function from X-ray powder diffraction data," Journal of Applied Crystallography, vol. 37, no. 4, p. 678, Aug 2004.

[37] E. Lorch, "Conventional and elastic neutron diffraction from vitreous silica," Journal of Physics C: Solid State Physics, vol. 3, no. 6, p. 1314, 1970.

[38] P. S. Salmon, "Decay of the pair correlations and small-angle scattering for binary liquids and glasses," Journal of Physics: Condensed Matter, vol. 18, no. 50, p. 11443, 2006.

[39] W. Yao, S. W. Martin, and V. Petkov, "Structure determination of low-alkali-content $Na_2S+B_2S_3$ glasses using neutron and synchrotron X-ray diffraction," Journal of Non-Crystalline Solids, vol. 351, no. 24-26, pp. 1995 – 2002, 2005.

[40] J. Johnson, C. Benmore, S. Stankovich, and R. Ruoff, "A neutron diffraction study of nano-crystalline graphite oxide," Carbon, vol. 47, no. 9, pp. 2239 – 2243, 2009.

[41] J. Sakurai, Modern Quantum Mechanics. Boston: Addison-Wesley, 2011.

[42] G. P. Williams, "Electron binding energies," in X-ray Data Booklet, 3rd ed., A. C. Thompson, Ed. Berkeley, CA: Lawrence Berkeley National Lab, 2009.

[43] M. de Broglie, "On a new method for obtaining photographs of line spectra of röntgen rays," Comptes Rendus, vol. 157, pp. 924–926, 1913.

[44] H. Fricke., "The K-characteristic absorption frequencies for the chemical elements magnesium to chromium," Physical Review, vol. 16, no. 3, pp. 202–215, Sep 1920.

[45] G. Hertz, "About the limits on the absorption in the L-series," Journal of Physics A Hadrons and Nuclei, vol. 3, no. 1, pp. 19–25, 1920.

[46] D. E. Sayers, E. A. Stern, and F. W. Lytle, "New technique for investigating noncrystalline structures: Fourier analysis of the extended X-ray absorption fine structure," Physical Review Letters, vol. 27, no. 18, pp. 1204–1207, Nov 1971.

[47] P. A. Lee and J. B. Pendry, "Theory of the extended X-ray absorption fine structure," Physical Review B, vol. 11, no. 8, pp. 2795–2811, Apr 1975.

[48] E. A. Stern, "Structure determination by X-ray absorption," Contemporary Physics, vol. 19, no. 4, pp. 289–310, 1978.

[49] S. D. Kelly, D. Hesterberg, and B. Ravel, "Analysis of soils and minerals using X-ray absorption spectroscopy," in Methods of Soil Analysis, Part 5 - Mineralogical Methods, A. L. Ulery and L. R. Drees, Eds. Madison, WI: Soil Science Society of America, Inc., 2008, ch. 14.

[50] J. B. Kortwright and A. C. Thompson, "X-ray emission energies," in X-ray Data Booklet, 3rd ed., A. C. Thompson, Ed. Berkeley, CA: Lawrence Berkeley National Lab, 2009.

[51] S. M. Heald, "Design of an EXAFS experiment," in X-ray Absorption: Principles, Applications, Techniques of EXAFS, SEXAFS and XANES, D. C. Koningsberger and R. Prins, Eds. New York: John Wiley and Sons, 1987, pages 3, pp. 87–118.

[52] G. Bunker, Introduction to XAFS. Cambridge University Press, 2010.

[53] D. C. Koningsberger and R. Prins, Eds., X-ray absorption: Principles, Applications, Techniques of EXAFS, SEXAFS and XANES. John Wiley and Sons Inc., New York, NY, 1987.

[54] M. Newville, P. Līviņš, Y. Yacoby, J. J. Rehr, and E. A. Stern, "Near-edge X-ray absorption fine structure of Pb: A comparison of theory and experiment," Physical Review B, vol. 47, no. 21, pp. 14 126–14 131, Jun 1993.

[55] B. D. Ravel, "Ferroelectric phase transistions in oxide perovskites by XAFS," Ph.D. dissertation, University of Washington, 1997.

[56] S. I. Zabinsky, J. J. Rehr, A. Ankudinov, R. C. Albers, and M. J. Eller, "Multiple-scattering calculations of X-ray absorption spectra," Physical Review B, vol. 52, no. 4, pp. 2995–3009, Jul 1995.

[57] S. J. Gurman, N. Binsted, and I. Ross, "A rapid, exact curved-wave theory for EXAFS calculations," Journal of Physics C: Solid State Physics, vol. 17, no. 1, p. 143, 1984.

[58] ——, "A rapid, exact, curved-wave theory for EXAFS calculations. II. the multiple-scattering contributions," Journal of Physics C: Solid State Physics, vol. 19, no. 11, p. 1845, 1986.

[59] E. A. Stern and S. M. Heald, "Basic principles and applications of exafs," in Handbook on Synchrotron Radiation, E.-E. Koch, Ed.   Amsterdam: North Holland Pub. Co, 1983, ch. 10, pp. 995–1014.

[60] J. J. Rehr and R. C. Albers, "Scattering-matrix formulation of curved-wave multiple-scattering theory: Application to X-ray absorption fine structure," Physical Review B, vol. 41, pp. 8139–8149, Apr 1990.

[61] ——, "Theoretical approaches to X-ray absorption fine structure," Review of Modern Physics, vol. 72, no. 3, pp. 621–654, Jul 2000.

[62] J. J. Rehr, R. C. Albers, C. R. Natoli, and E. A. Stern, "New high-energy approximation for X-ray absorption near edge structure," Physical Review B, vol. 34, no. 6, pp. 4350–4353, Sep 1986.

[63] J. Mustre de Leon, J. J. Rehr, S. I. Zabinsky, and R. C. Albers, "Ab-initio curved-wave X-ray absorption fine structure," Physical Review B, vol. 44, no. 9, pp. 4146–4156, Sep 1991.

[64] B. Ravel and M. Newville, "*ATHENA*, *ARTEMIS*, *HEPHAESTUS*: data analysis for X-ray absorption spectroscopy using *IFEFFIT*," Journal of Synchrotron Radiation, vol. 12, no. 4, pp. 537–541, Jul 2005.

[65] M. Newville, "*IFEFFIT*: interactive XAFS analysis and *FEFF* fitting," Journal of Synchrotron Radiation, vol. 8, no. 2, pp. 322–324, Mar 2001.

[66] G. G. Li, F. Bridges, and C. H. Booth, "X-ray absorption fine structure standards: A comparison of experiment and theory," Physical Review B, vol. 52, no. 9, pp. 6332–6348, Sep 1995.

[67] J. J. Rehr and A. L. Ankudinov, "Progress in the theory and interpretation of XANES," Coordination Chemistry Reviews, vol. 249, no. 1-2, pp. 131 – 140, 2005, Synchrotron Radiation in Inorganic and Bioinorganic Chemistry.

[68] G. G. Li, F. Bridges, and C. H. Booth, "X-ray-absorption fine-structure standards: A comparison of experiment and theory," Physical Review B, vol. 52, no. 9, pp. 6332–6348, Sep 1995.

[69] S. Calvin, "Relationship between electron delocalization and asymmetry of the pair distribution function as determined by X-ray absorption spectroscopy," Ph.D. dissertation, City University of New York, 2001.

[70] S. Wei, H. Oyanagi, W. Liu, T. Hu, S. Yin, and G. Bian, "Local structure of liquid gallium studied by X-ray absorption fine structure," Journal of Non-Crystalline Solids, vol. 275, no. 3, pp. 160–168, 2000.

[71] C. Glover, G. Foran, and M. Ridgway, "Structure of amorphous silicon investigated by exafs," Nuclear Instruments and Methods in Physics Research Section B: Beam Interactions with Materials and Atoms, vol. 199, pp. 195–199, 2003.

[72] P. Bevington and D. K. Robinson, <u>Data Reduction and Error Analysis for the Physical Sciences</u>. New York: McGraw-Hill, 1992.

[73] L. Brillouin, <u>Science and Information Theory</u>. Mineola, N.Y: Dover Publications, 2004.

[74] E. A. Stern, "Number of relevant independent points in X-ray absorption fine structure spectra," <u>Physical Review B</u>, vol. 48, no. 13, pp. 9825–9827, Oct 1993.

[75] L. Tröger, D. Arvanitis, K. Baberschke, H. Michaelis, U. Grimm, and E. Zschech, "Full correction of the self-absorption in soft-fluorescence extended X-ray absorption fine structure," <u>Physical Review B</u>, vol. 46, no. 6, pp. 3283–3289, Aug 1992.

[76] T. Mason, G. Gonzalez, J. Hwang, and D. Kammler, "Point defects and related properties of highly co-doped bixbyite In_2O_3," <u>Physical Chemistry Chemical Physics</u>, vol. 5, no. 11, pp. 2183–2189, Jan 2003.

[77] P. Parent, H. Dexpert, G. Tourillon, and J. Grimal, "Structural study of tin-doped indium oxide thin-films using X-ray absorption spectroscopy and X-ray diffraction: 1. description of the indium site," <u>Journal of the Electrochemical Society</u>, vol. 139, no. 1, pp. 276–281, Jan 1992.

[78] J. E. Huheey, E. A. Keiter, and R. L. Keiter, <u>Inorganic Chemistry: Principles of Structure and Reactivity</u>, 4th ed. New York: HarperCollins College Publishers, 1993.

[79] L. Galoisy, L. Cormier, G. Calas, and V. Briois, "Environment of Ni, Co and Zn in low alkali borate glasses: information from EXAFS and XANES spectra," <u>Journal of Non-Crystalline Solids</u>, vol. 293, pp. 105–111, 2001.

[80] H. Wang, Y. Wei, Y. Yang, and J. Lee, "XAS study of Zn-doped Al_2O_3 after thermal treatment," <u>Journal of Electron Spectroscopy and Related Phenomena</u>, vol. 144, pp. 817–819, 2005.

[81] C. A. Hoel, J.-F. Gaillard, and K. R. Poeppelmeier, "Probing the local structure of crystalline ZITO $In_{2-2x}Sn_xZn_xO_3$ ($x \leq 0.4$)," <u>Journal of Solid State Chemistry</u>, vol. 183, no. 4, pp. 761–768, Mar 2010.

[82] M. Takahashi, H. Tanida, S. Kawauchi, M. Harada, and I. Watanabe, "DV-X_α MO approach to Zn k-XANES spectra of zinc aqueous solution," <u>Journal of Synchrotron Radiation</u>, vol. 6, no. 3, pp. 278–280, 1999.

[83] G. Waychunas, C. Fuller, J. Davis, and J. Rehr, "Surface complexation and precipitate geometry for aqueous Zn (II) sorption on ferrihydrite: II. XANES analysis and simulation," <u>Geochimica et Cosmochimica Acta</u>, vol. 67, no. 5, pp. 1031–1043, 2003.

[84] D. B. Miracle, "The efficient cluster packing model - an atomic structural model for metallic glasses," <u>Acta Materiala</u>, vol. 54, no. 16, pp. 4317–4336, Jan 2006.

[85] D. B. Miracle, T. Egami, K. M. Flores, and K. F. Kelton, "Structural aspects of metallic glasses," <u>MRS Bulletin</u>, vol. 32, no. 8, pp. 629–634, Jan 2007.

[86] A. Kuzmin and J. Purans, "The influence of the focusing effect on the X-ray absorption fine structure above all the tungsten L edges in non-stoichiometric tungsten oxides," <u>Journal of Physics: Condensed Matter</u>, vol. 5, p. 9423, 1993.

Appendix A

PDF - Supplemental Material

A.1   Scattering Processes

There are many different ways that an X-ray can scatter off of a material. The two general categories are coherent and incoherent. Coherently scattered X-rays have a definite phase relationship with each other, producing interference effects. The measured intensity, I, of coherently scattered X-rays is the square of the sum of the amplitude of each X-ray, ψ, $I = |\psi_1 + \psi_2 + \ldots|^2$. Incoherently scattered X-rays have no phase relationship with each other and do not show interference effects. The measured intensity from these X-rays is given by $I = |\psi_1|^2 + |\psi_2|^2 + \ldots$, the sum of the squares of the amplitude.

Scattering processes can also be categorized as elastic or inelastic. Elastic scattering events are those in which the X-ray loses no energy in the process, and inelastic processes are those which the X-ray gives up some portion of its energy to the sample. Bragg scattering is elastic and coherent, while Compton scattering is inelastic and incoherent. Thermal diffuse scattering is coherent and inelastic and Laue diffuse scattering is incoherent and elastic. Structural information is obtained from the effects of interference between the incoming and outgoing waves, thus only look coherent scattering is used to determine structural information.

A.2   The Total Scattering Amplitude - $\Psi(\mathbf{Q})$

In deriving a simple expression for Eq. 3.3, it is important to use the approximation that no multiple scattering event will contribute to the observed scattering intensity. Starting with this

assumption in mind, write the wave equation for an incident X-ray as

$$\psi_i(\mathbf{r}) = A_i \frac{e^{i\mathbf{k}_i \mathbf{r}}}{\mathbf{r}}, \tag{A.1}$$

where A_i is the incident amplitude and $\mathbf{k}_i$ is the initial wave vector of the wave. Assuming this X-ray experiences an elastic scattering event, its wavefunction can be written as

$$\psi_f(\mathbf{r}) = A_f \frac{e^{i\mathbf{k}_f \mathbf{r}}}{\mathbf{r}} e^{i\delta}, \tag{A.2}$$

where the δ represents a phase shift of the scattered wave. The location of the scattering event is at $\mathbf{r} = \mathbf{r}_\nu$, where ν describes where the νth scattering site. The magnitude of the wavevectors, but not the direction, are equal, because of the assumption that the scattering was elastic. The incident and scattered wavefunctions can therefore be equated,

$$A_i \frac{e^{i\mathbf{k}_i \mathbf{r}_\nu}}{\mathbf{r}_\nu} = A_f \frac{e^{i\mathbf{k}_f \mathbf{r}_\nu}}{\mathbf{r}_\nu} e^{i\delta}, \tag{A.3}$$

and with a little rearrangement,

$$A_f = A_i e^{i\left[(\mathbf{k}_i - \mathbf{k}_f)\mathbf{r}_\nu - \delta\right]}. \tag{A.4}$$

Substituting this equation into Eq A.2,

$$\psi_f(\mathbf{r}) = A_i e^{i\left[(\mathbf{k}_i - \mathbf{k}_f)\mathbf{r}_\nu - \delta\right]} \frac{e^{i\mathbf{k}_f \mathbf{r}}}{\mathbf{r}_\nu} \tag{A.5}$$

$$= \Psi(\mathbf{Q})\psi_0(\mathbf{r}). \tag{A.6}$$

Using the following definitions,

$$\mathbf{Q} = \mathbf{k}_i - \mathbf{k}_f, \quad \Psi(\mathbf{Q}) = e^{i\mathbf{Q}\mathbf{r}_\nu}, \quad \psi_0(\mathbf{r}) = A_i \frac{e^{i\left(\mathbf{k}_f \mathbf{r} - \delta\right)}}{\mathbf{r}_\nu}, \tag{A.7}$$

where $\mathbf{Q}$ is the scattering vector. If we now sum $\Psi(\mathbf{Q})$ over each atom, ν, we get the sample scattering amplitude,

$$\Psi(\mathbf{Q}) = \frac{1}{\langle b \rangle} \sum_\nu b_\nu e^{i\mathbf{Q}\mathbf{r}_\nu}, \tag{A.8}$$

where b_ν is the scattering amplitude of the atom, and $\langle b \rangle$ represents the average scattering power of all the atoms. The summation term is equivalent to the scattering factor as defined in traditional

crystallography, although the $\mathbf{Q}$ is often written as $\mathbf{K}_{hkl}$, where the $h, k,$ and l define the reciprocal lattice vectors, and the sum is over atoms in the unit cell. However, in this case there is no limitation of periodicity imposed, instead the choice is made to sum over all atoms in the sample.

A.3   Scattering Cross-Section - $d\sigma/d\Omega$

Starting with a scattered wave (Eq. A.2),

$$\psi_f = \frac{e^{ikr}}{r}\langle b\rangle \Psi(Q), \tag{A.9}$$

where $\langle b\rangle$ has replaced A_f the scattered amplitude, and $\Psi(Q)$ is defined in Eq. A.8 with the assumption of isotropic scattering. Assuming the incoming wave has a flux density of I_0, the intensity of the scattered wave, $I_s\ dr^2$, is given by,

$$I_s\ dr^2 = I_s r^2\ d\Omega = I_0|\psi_f|^2 r^2\ d\Omega = I_0\ d\sigma, \tag{A.10}$$

where σ is the scattering cross-section. Solving for this yields,

$$\frac{d\sigma}{d\Omega} = \frac{1}{N}|\psi_f|^2 r^2 = \frac{1}{N}\langle b\rangle^2 |\Psi(Q)|^2, \tag{A.11}$$

where the $1/N$ was added to represent the scattering cross section per atom.

Appendix B

XAFS - Supplemental Material

B.1   Heuristic Derivation

The simple picture of EXAFS involves an atom absorbing a photon and ejecting a core electron. This absorption is a transition governed by quantum mechanics and Fermi's Golden Rule. Thus the absorption can be written as,

$$\mu \propto |\langle f|\mathcal{H}|i\rangle|^2 \,, \tag{B.1}$$

where i represents the initial state, f represents the final state, and $\mathcal{H}$ is the Hamiltonian. From this point rigorous methods can be used to develop the EXAFS equation [47, 53].

As was mentioned in section 5.6, phenomenological methods can also be employed to derive the derive the EXAFS equation, $\chi(k)$ [53, 55]. After an atom absorbs an X-ray, the wave function of the outgoing photoelectron is $\psi(k, r) = e^{ikr}/(kr)$, where $k \equiv \tau/\lambda$, is the wavenumber of the photoelectron.[1]   The outgoing spherical wave will encounter nearby atoms and scatter off of them, producing interference patterns. These interference patterns are the source of the EXAFS signal. If the photoelectron encounters a scattering atom at $\boldsymbol{r_i}$, the scattered wave will have the form,

$$\frac{e^{ikr}}{kr} \frac{e^{ik|\boldsymbol{r}-\boldsymbol{r_i}|}}{k|\boldsymbol{r}-\boldsymbol{r_i}|}, \tag{B.2}$$

where the second term is the reflected wave originating at $\boldsymbol{r_i}$. If the wave travels back to the origin, both waves will have traveled a distance R and we can write

$$\frac{e^{i2kR}}{(kR)^2}. \tag{B.3}$$

---

[1] Remember $\tau \equiv 2\pi$.

This expression assumes the photoelectron is traveling in a constant potential. However, near the potential well created by the atom, the photoelectron will pick up a phase shift, $\phi(k) - \tau/4$. The $\tau/4$ is due to the outwardly propagating spherical wave from the K-shell. This term is dependent on the Z of both the scattering and absorbing atoms and is sometimes written as $\phi_a(k) + \phi_s(k)$ to express that explicitly. The probability of the outgoing wave being scattered is expressed as $F(k)$. This term is also dependent on the Z of the scattering atom. Our complex wave expression now is given by

$$F(k)\frac{e^{i(2kR-\phi(k)-\tau/4)}}{(kR)^2}.$$ (B.4)

The imaginary part of Eq. B.4 will be proportional to the EXAFS signal, we can thus write

$$\chi_i \propto \frac{F_i(k)}{(kR_i)^2} \sin\left(2kR_i + \phi(k)\right).$$ (B.5)

The subscripted i indicates that the expression will be summed over all neighboring atoms.

An important effect that must be taken into account is the lifetime of the photoelectron and the core hole that is created, this is expressed as $\lambda(k)$. Any experimental broadening will also be part of this term. Now our expression is

$$\chi_i \propto \frac{F_i(k)}{(kR_i)^2} \sin\left(2kR_i + \phi(k)\right) e^{2R_i/\lambda(k)}.$$ (B.6)

Up to now each neighboring atom has been evaluated as a separate term. If two atoms are at identical distances from the absorbing atom, Eq. B.6 will be identical for each of the atoms. If these common terms are grouped together the amount of required computation time is reduced. Now rather than the sum being over each individual atom, it is over a group of atoms all at the same distance from the absorbing atom. In other words the sum is now over each **shell** of atoms. An additional term must be added to account for the number of atoms in each shell, given by N_i, the **coordination number**. However, in any real system this assumption is unphysical. Even in a perfect crystal, the thermal motion of the atoms will mean that each atom in a particular shell will actually have a slightly different distance to the absorbing atom. Assuming this disorder is small and gaussian, it will attenuate the EXAFS by a factor of $e^{-2k^2\sigma_i^2}$, where σ_i^2 is the root mean

square of the bond lengths, referred to as the Mean Square Radial Disorder (MSRD). The MSRD can also be expressed as $\langle (R_j - \bar{R}_i)^2 \rangle$, where R_j is bond length of a particular atom and $\bar{R}_i$ is the average bond length of the shell. This term accounts for static and thermal disorders. Now our expression is written as

$$\chi_i \propto \frac{F_i(k)}{(kR_i)^2} \sin\left(2kR_i + \phi(k)\right) e^{2R_i/\lambda(k)} e^{-2k^2\sigma_i^2}. \tag{B.7}$$

In the presence of the core hole, the electrons surrounding the absorbing atom will relax slightly. This relaxation means that the wavefunctions will not perfectly overlap anymore, causing the amplitude to decrease. This requires another term, S_0^2, to be added to the formula,

$$\chi_i \approx \frac{S_0^2 F_i(k)}{(kR_i)^2} \sin\left(2kR_i + \phi_i(k)\right) e^{2R_i/\lambda(k)} e^{-2k^2\sigma_i^2}, \tag{B.8}$$

and

$$\chi(k) = \sum_i \chi_i(k). \tag{B.9}$$

This equation is what is commonly referred to as the EXAFS equation, and is equivalent to Eq. 5.8, neglecting the C_3 term. This is the same form that was developed in the initial derivation of the EXAFS equation [46], where plane-wave approximations were used. Once the derivation of the exact EXAFS equation using spherical waves was completed, it was able to recast into the original form, with $F_i^{eff}(k)$ and $\phi_i^{eff}(k)$ [63].

B.2   Cumulant Expansion

Following a more mathematically detailed approach to deriving the EXAFS equation, it can written in an integral form,

$$\chi(k) = \sum_i \chi_i(k) = \int \sin(2kr) \frac{P_i(R)}{R^2} \, dR, \tag{B.10}$$

where $P_i(R)$ is the pair distribution function (PDF) of the absorbing-scattering atom pair, and the integral accounts for the fact that a EXAFS experiment probes a macroscopic number of atoms. For clarity, I have left off the terms correcting for the phase shift ($\phi_i(k)$) and lifetime ($\lambda(k)$), as

well as a pre-factor of $F_i(k)/k$. For the rest of the discussion, I will drop the summation term for clarity.

Assuming the PDF is approximately gaussian, the EXAFS equation can be written as an expansion,

$$\chi(k) = \int \sin(2kr)\frac{P(R)}{R^2}\,dR = \exp\left[\sum_{n=0}^{2}\frac{(2ik)^2}{n!}C_n\right],\qquad(B.11)$$

where the C_n terms are referred to as cumulants. The physical validity of this idea can be seen if the PDF is assumed to be gaussian, with $\bar{R}_0$ being the mean radial distance in the model with a variance of σ^2, and R_1 is the actual radial distance of the PDF. Equation B.10 can then be written as

$$\int e^{2ik(R-\bar{R}_0)}\frac{1}{\sqrt{\tau}\sigma}\exp\left[-\frac{(R-R_1)^2}{2\sigma^2}\right]\,dR = \exp\left[2ik(R_1-\bar{R}_0)-2k^2\sigma^2\right].\qquad(B.12)$$

It can be seen using Eq. B.11, that for a pure gaussian lineshape, $C_1 = R_1 - \bar{R}_0$ and $C_2 = \sigma^2$. In the gaussian case no higher order cumulants contribute. The first cumulant represents the difference in the model centroid versus that of the PDF, $C_1 = \langle\Delta R\rangle \equiv R_1 - \bar{R}_0$. The second cumulant represents the variance in the distance between the particular absorber-scatterer pair. Thus the definition $C_2 = \sigma^2 \equiv \left\langle(R_1-\bar{R}_0)^2\right\rangle$. These definitions fit with the EXAFS equation as presented in Eq. 5.8. Assuming a **slightly** non-gaussian shape, a similar definition can be applied to the third cumulant, $C_3 = \left\langle(R-\bar{R}_0)^3\right\rangle$. This parameter will represent the skewness of the distribution from a gaussian. Higher order cumulants can be used, but their definitions become less straightforward, and they are not used in this work. Using the approximations already discussed the EXAFS equation can be written out to the third cumulant as (from [69]),

$$\chi(k) = \sum_i \text{Im}\left\{\frac{\frac{F_i(k)S_0^2}{k(r_{0,i}-C_{1,i})^2}}{\times\exp\left[-2\frac{r_{0,i}}{\lambda(k)}-2\left(k-\frac{i}{\lambda(k)}\right)^2 C_{2,i}+2ik\left(r_{0,i}+C_{1,i}\right)+i\phi_i(k)-i\left(k-\frac{i}{\lambda(k)}\right)\left(\frac{4C_{2,i}}{r_{0,i}}\right)-i\frac{4}{3}\left(k-\frac{i}{\lambda(k)}\right)^3 C_{3,i}\right]\right\}.\qquad(B.13)$$

B.3   In$_2$O$_3$ EXAFS Results

Powdered In$_2$O$_3$ was measured in fluorescence mode to calibrate S_0^2 values for use in the fitting of a-IZO samples. For unknown reasons, when the transmission data was used to calibrate for S_0^2, the value came out to be above 1.05, which is somewhat beyond the accepted range. The background was removed using the methods discussed in section 5.4. To reduce Fourier transform ripples a Hanning window with 0.5 $\mathring{A}^{-1}$ sills was used over a k-range of 2.5 - 13 $\mathring{A}^{-1}$. The fit was performed using k-weights of 1, 2, and 3 simultaneously in order to reduce correlations between variables. The fit used an R^*-range of 1 - 4 $\mathring{A}$. This combination of k- and R^*-ranges results in the data containing 20 independent data points. The edge energy was set to 27950 eV, which is approximately the peak of the white line in the absorption spectrum. This choice resulted in a refined value for E_0 close to zero.

B.3.1   In$_2$O$_3$ Model

The theoretical model used to fit the In$_2$O$_3$ data is identical to that used for the IZO samples described in section 7.2, minus the Zn of course. However, since In$_2$O$_3$ is a well-defined crystalline material additional paths were needed to properly analyze the spectrum.

B.3.1.1   Single Scattering Paths

The most prominent signals in In$_2$O$_3$ are the single scattering paths of the 1$^{\text{st}}$ shell O atoms and the 2$^{\text{nd}}$ and 3$^{\text{rd}}$ shell In atoms. It was found that the fit was improved if two other, more distant, single scattering paths were used. Each of these shells is composed of 6 O atoms at 4.00 and 4.09 $\mathring{A}$. It is typical to include paths above the fitting range because an EXAFS scattering path will actually peak somewhat below the scattering distance as discussed in Chapter 5.

If all the standard parameters for each of these three paths $(S_0^2, N_i, R_i, \sigma_i^2, E_0)$ were allowed to be fit independently in the model, 45 variables would be needed. Ideally the number of variables should be about half of the number of independent data points, but in this case there are only

20 independent data points in the data. Thus there are about a factor of 4 too many variables. However, many of these variables are related and be constrained in a reasonable way to reduce the number of variables.

B.3.1.2 Multiple Scattering Paths

Two types of multiple scattering paths were used in the fit to the In_2O_3 standard. The first was triangular paths involving one O atom and one In atom. As the name implies, for these scattering paths the photoelectron forms a triangle between the absorbing atom and two other neighboring atoms. These paths are typically weak, however they can have large degeneracies. In this context the degeneracy refers to the number of unique combinations of scattering atoms give rise to the same path expression. Three of these paths were used, each having a degeneracy of 12. Two of the paths had a scattering distance near 3.87 Å and the other had a distance of 4.07 Å. The two shorter paths scatter off the 2nd shell In atom and a 1st shell O atom. The longer path scatters off of a 3rd shell In atom and a 1st shell O atom.

The second type of multiple scattering path needed was the collinear scattering path. In this case, the photoelectron scatters off a 1st shell O atom, then scatters off the absorbing atom a second time, and finally scatters off a different 1st shell O atom before returning to the absorbing atom. All three atoms fall in a linear, or nearly so, arrangement. Paths of this nature tend to have somewhat larger amplitudes because of a "self-focusing" effect. This effect arises because the scattering phases of collinear paths adds constructively, increasing the amplitude of the path [86].

B.3.2 In_2O_3 Fit Results

B.3.2.1 Parameterization

There are many ways to parameterize the variables in an EXAFS fit, but each method generally rests on a few physically justified assumptions [52, 69, 86]. Fit constraints were obtained by starting with an initially highly constrained model and then selectively relaxing the constraints. If the relaxed value came out significantly different than the constrained value, and stayed physically

reasonable, the change was deemed a good one. This was also justified because the χ^2_ν and $\mathcal{R}$ would decrease once this additional variable was added to the model. This was an iterative process because some variables can be correlated with others in non-intuitive ways.

Single Scattering Paths   Because the oxide powder should be near the ideal structure, the coordination numbers for every path was fixed at the crystallographic value. The passive electron reduction factor, S_0^2, was a free parameter, but constrained to be identical for all scattering paths. For all paths a single, free, E_0 parameter was used. For the 1$^{\text{st}}$ In-O scattering shell the rest of the variables (R_O, σ_O^2, C_3) were allowed to vary in the fit. This was the only shell where $C_3 \neq 0$ was allowed.

Rather than fitting the actual In-In distance, I fit the percentage change in the average bond length from the crystallographic bond length. This allowed both of the In-In shells scattering distance to be fit using a single parameter, the scaled path difference, ΔR_{In}. With this definition the actual path of each In-In path i is given by

$$R_{\text{eff},i} \equiv R_{In,i}\left(1 + \Delta R_{In}\right),\tag{B.14}$$

where $R_{In,i}$ is the ideal In-In separation of each path, and $R_{\text{eff},i}$ is the In-In distance from the fit. The MSRD for each In-In path (σ_{In1}^2 and σ_{In2}^2) were independent.

For the two distant In-O shells, a single path length parameter was used. It was defined using the same method as the In-In shells. The MSRD for each of these shells was constrained to be identical to the 1$^{\text{st}}$ shell MSRD. Although intuitively it would be expected to have a larger MSRD, the large error bars obtained from this distant path made it relatively flexible.

Multiple Scattering Paths   For the triangular paths scattering length I used the average the single scattering In-O and In-In distances. The MSRD was defined as the sum of the values from the In-O and In-In paths. This assumption means that the scattering atoms are moving in an uncorrelated manner. For the collinear path, both the scattering path length and the σ^2 values were constrained to be equal to the values obtained for the first shell. While different, and more complex, constraint schemes could be constructed, the effects of multiple scattering paths

are generally weak when compared to the single scattering path amplitudes. Also, since I am only interested in the In_2O_3 sample as a reference material a finely tuned model is not necessary.

B.3.2.2   Results

The S_0^2 parameter was found to be 0.82 ± 0.05. This should be viewed as a low estimate of the number because self-absorption is not taken into account, however the effect should be relatively minor. This underestimation of S_0^2 will result in a slight overestimation of the O coordination number in the fit results for IZO. Since S_0^2 and N are perfectly correlated, this will result in the absolute value of N being slightly wrong, but any relative trends will remain unchanged. Table B.1 summarizes the fit results.

Table B.1: The single scattering path fit results. For all paths $E_0 = 0.9(3)$ and $S_0^2 = 0.82(5)$. R_i represents the crystallographic value for the path length and ΔR_i represents the percentage deviation from the ideal value. The model used 9 variables and the goodness-of-fit was $\mathcal{R}=0.0048$.

Neighbor	$R_i\left(\text{Å}\right)$	$\Delta R_i(\%)$	$\sigma_i^2\left(\text{Å}^2\right)$	$C_3\left(\text{Å}^3\right)$
O_1	2.19	-0.5(2)	$0.0057(6)^c$	0.0001(1)
In_1	3.35	$0.44(8)^a$	0.0041(3)	0
In_2	3.82	$0.44(8)^a$	0.0048(4)	0
O_2	4.00	$1.8(4)^b$	$0.0057(6)^c$	0
O_3	4.09	$1.8(4)^b$	$0.0057(6)^c$	0

^{a,b,c} Parameters were constrained to be equivalent.

The fit to the In_2O_3 standard is shown in Fig. B.1. The top panel shows the $\chi(k)k^3$ data and the bottom panel show the Fourier transformed data, $|\chi(R^*)|$. The first three main peaks in $|\chi(R^*)|$ at 1.6, 2.1, and 3.5 Å correspond the first three coordination shells. The signal from the outer two In-O shells peaked just below the 3.5 Å peak.

B.4   ZnO EXAFS Results

Powdered ZnO was measured in transmission mode to calibrate S_0^2 for use in fitting the Zn-edge of a-IZO samples. The background removal followed the methods discussed in section 5.4.
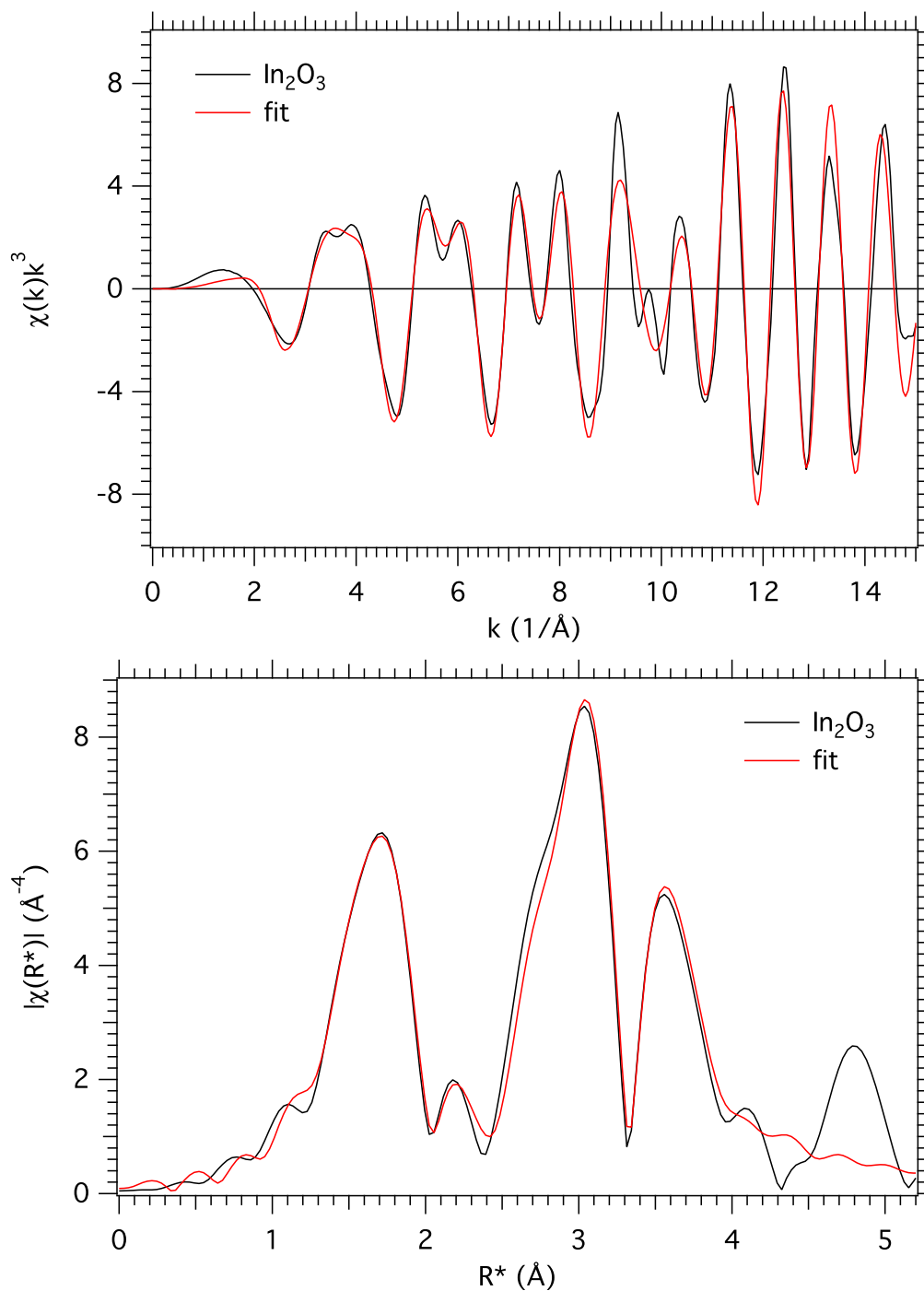
Figure B.1: (top) The k^3-weighted EXAFS of powder In_2O_3 (black) and the fit (red). (bottom) The magnitude of the Fourier transform shown with the same color scheme.

Hanning windows with 0.5 Å^{-1} sills were used over a Fourier transform range of $k = 3 - 12$ Å^{-1}, and an R^*-range of $1 - 3.4$ Å. These fit regions produced 13 independent data points. The edge energy was set to 9663 eV, which approximately the peak in the first derivative of the absorption spectrum of ZnO.

To model the ZnO EXAFS, a wurtzite structure structure (space group P6$_3$mc) was used. A suitable fit was obtained if all single scattering shells with a path length of $R < 3.9$ Å were used. This resulted in 5 single scattering Zn-O shells (2 of which being nearest-neighbors) and 2 single scattering Zn-Zn shells. The three additional Zn-O single-scattering shells ($R_i = 3.22, 3.80$ and 3.81 Å) were constrained to have the same ΔR_i and MSRD as the nearest neighbors oxygen atoms. Table B.2 provides a summary of the fit results and Fig. B.2 shows both the $\chi(k)$ data and the magnitude of the Fourier transform of the ZnO fit results. The parameterization of fit parameters followed a similar logic as in section B.3.

Table B.2: Fit parameters used in the fit of ZnO. The parameters E_0 and S_0^2 were constrained to be the same for all paths and found to be 5.2(8) eV and 0.91(7), respectively. R_i indicates the crystallographic value of the interatomic distance, ΔR_i is the percentage change from the ideal distance, and σ_i^2 is the MSRD of the path. The fit yielded a $\chi_\nu^2 = 379$ and $\mathcal{R} = 0.006$.

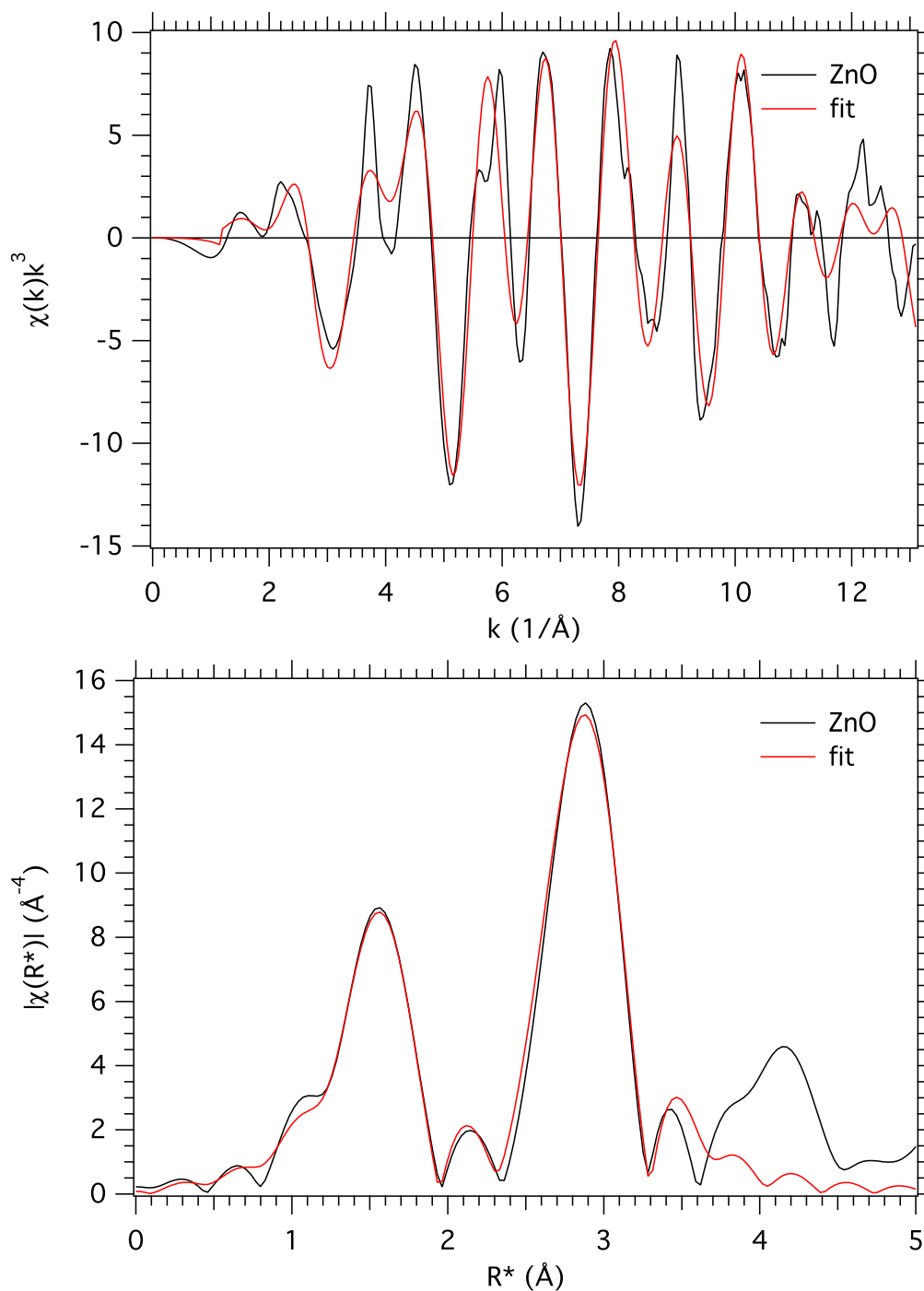| Path	R_i(Å)	ΔR_i(%)	$\sigma_i^2 \left(\text{Å}^2 \right)$
Zn-O$_{NN}$	1.97,1.99	-0.4(4)	0.005(1)
Zn-Zn$_1$	3.22	-1.0(2)	0.002(1)^a
Zn-Zn$_2$	3.25	1.9(3)	0.002(1)^a

^{a} Parameters were constrained to be equivalent.

Figure B.2: (top) the k^3 weighted $\chi(k)$ data (black) and fit (red). The fit range in k was $3-12$ Å^{-1}. (bottom) The magnitude of the Fourier transform and fit use the same color scheme. The fitting range in R^*-space was $1.0-3.4$ Å. All single scattering paths with a path length of < 3.9 Å were used in the fit.